T-3575

SEISMIC PRESTACK ANALYSIS OF A MISSION CANYON RESERVOIR, WILEY FIELD, BOTTINEAU COUNTY, NORTH DAKOTA

by

Julianne Marhoefer

ProQuest LLC.
789 East Eisenhower Parkway
P.O. Box 1346
Ann Arbor, MI 48106 – 1346

T-3575

A thesis submitted to the Faculty and the Board of Trustees of the Colorado School of Mines in partial fulfillment of the requirements for the degree of Master of Science (Geophysics).

Golden, Colorado

Date April 13, 1988

Signed: Julianne Marhoefer

Julianne Marhoefer

Approved: Thomas L. Davis

Dr. Thomas L. Davis
Thesis advisor

Golden, Colorado

Date 4/13/88

P R Romig

Dr. Phillip R. Romig
Department Head
Geophysics Department

ABSTRACT

Changes in lithology, porosity and pore fluids affect amplitude and character changes on seismic data. The purpose of this thesis was to determine whether carbonate porosity changes and/or lithologic changes could be detected in the Mission Canyon Formation in the Wiley Field of North Dakota by analysis of amplitude and character changes.

Prestack analysis using summed CDP gathers and common offset stacks enabled interpretations that could not be adequately evaluated on the stacked section alone. Tuning effects were a limiting factor on the range of offsets that could be used. Changes in seismic character were more important than changes in amplitude for distinguishing porous carbonates from nonporous carbonates. Lithologic and thickness changes have a greater influence on the seismic response than porosity variations.

TABLE OF CONTENTS

LIST OF FIGURES AND TABLES

ACKNOWLEDGEMENTS

I would like to thank the many individuals and sponsors without whom this thesis would not have been possible:

First, I would like to thank the members of my graduate committee, Tom Davis (advisor), Guy Towle, and Ray Sengbush for their help and advice. I would like to express special thanks to Tom Davis for suggesting the thesis topic and for helping to obtain funding for the thesis and my graduate studies. Guy Towle also deserves special thanks for devoting much of his time and his laboratory equipment for the rock properties measurements.

Bill Schneider and Bob Shurtleff of Golden Geophysical offered much valuable advice on special processing.

Eugene Asencio devoted much of his time toward helping me to learn the DISCO software at Golden Geophysical.

Finally, without corporate sponsors to provide much of the funding, this thesis would never have been completed. Tenneco funded 2 years of graduate study and the processing of the seismic data. Mobil provided tuition for my final semester.

INTRODUCTION

Lateral changes in lithology, porosity, and pore fluids have an effect on seismic amplitude and waveform changes. The most dramatic effects have been observed for gas saturated sands encased in shales (Gassaway, 1986, 1983; Yu, 1985; and Ostrander, 1984). The purpose of this thesis is to determine whether carbonate porosity changes and/or lithologic changes can be detected in the Glenburn Member of the Mission Canyon Formation at 4000 feet of depth in the Wiley field.

A seismic line across the Wiley Field in Bottineau County, North Dakota was reprocessed. Figure 1 shows the location of the Williston Basin and study area; Figure 2 shows the approximate location of the seismic line and the approximate locations of the facies change from carbonate to anhydrite for the Bluell, Sherwood, Mohall, and Glenburn Members in the Frobisher-Alida interval of the Mission Canyon Formation. Figure 2 also shows the structure on the base of the "State A", which is a commonly used marker at the boundary between the lower Charles Formation and the upper Frobisher-Alida.
The seismic line was previously included in a Master's

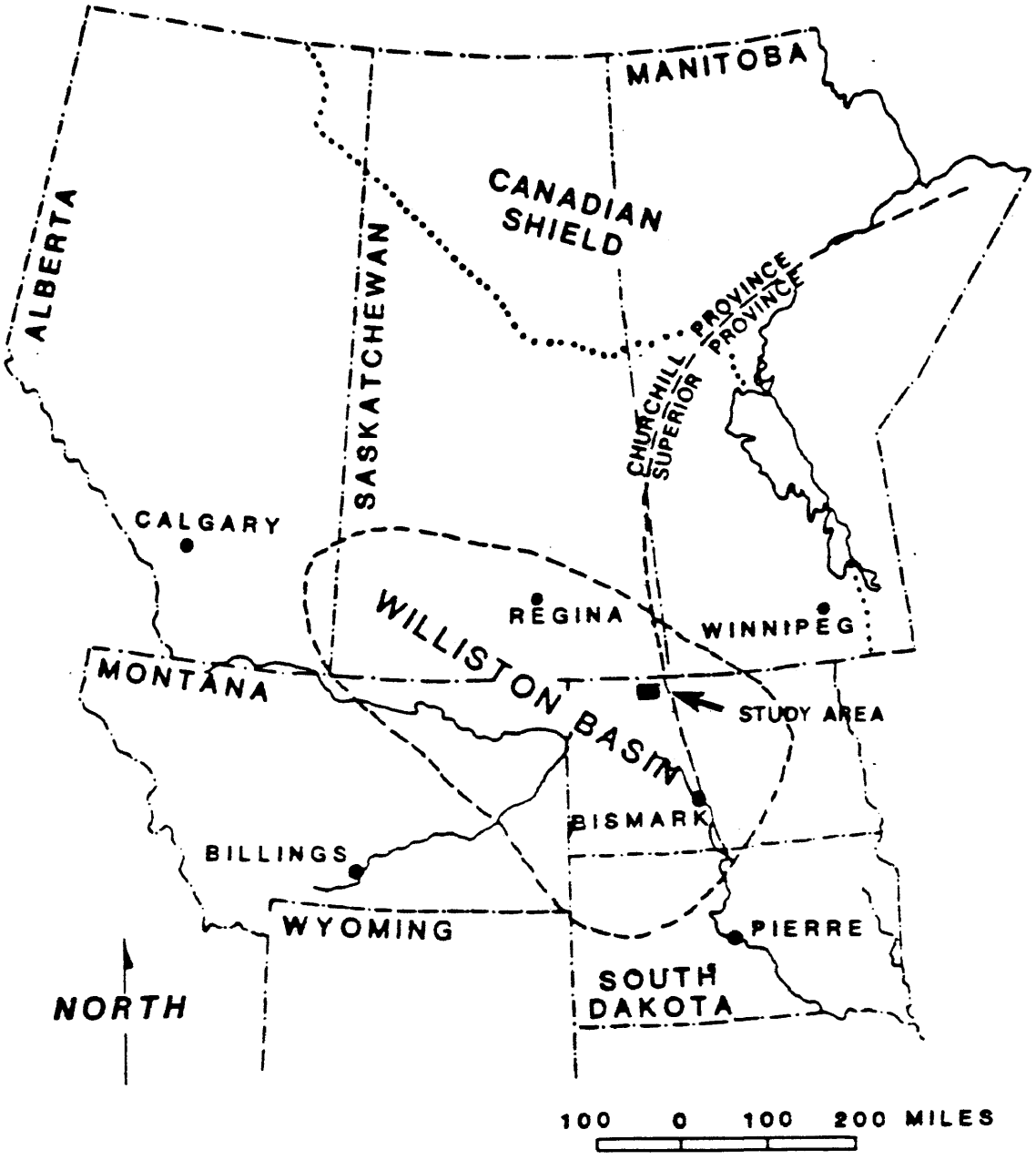

Figure 1. Location of the Williston Basin and study area (from Reeve, 1986).

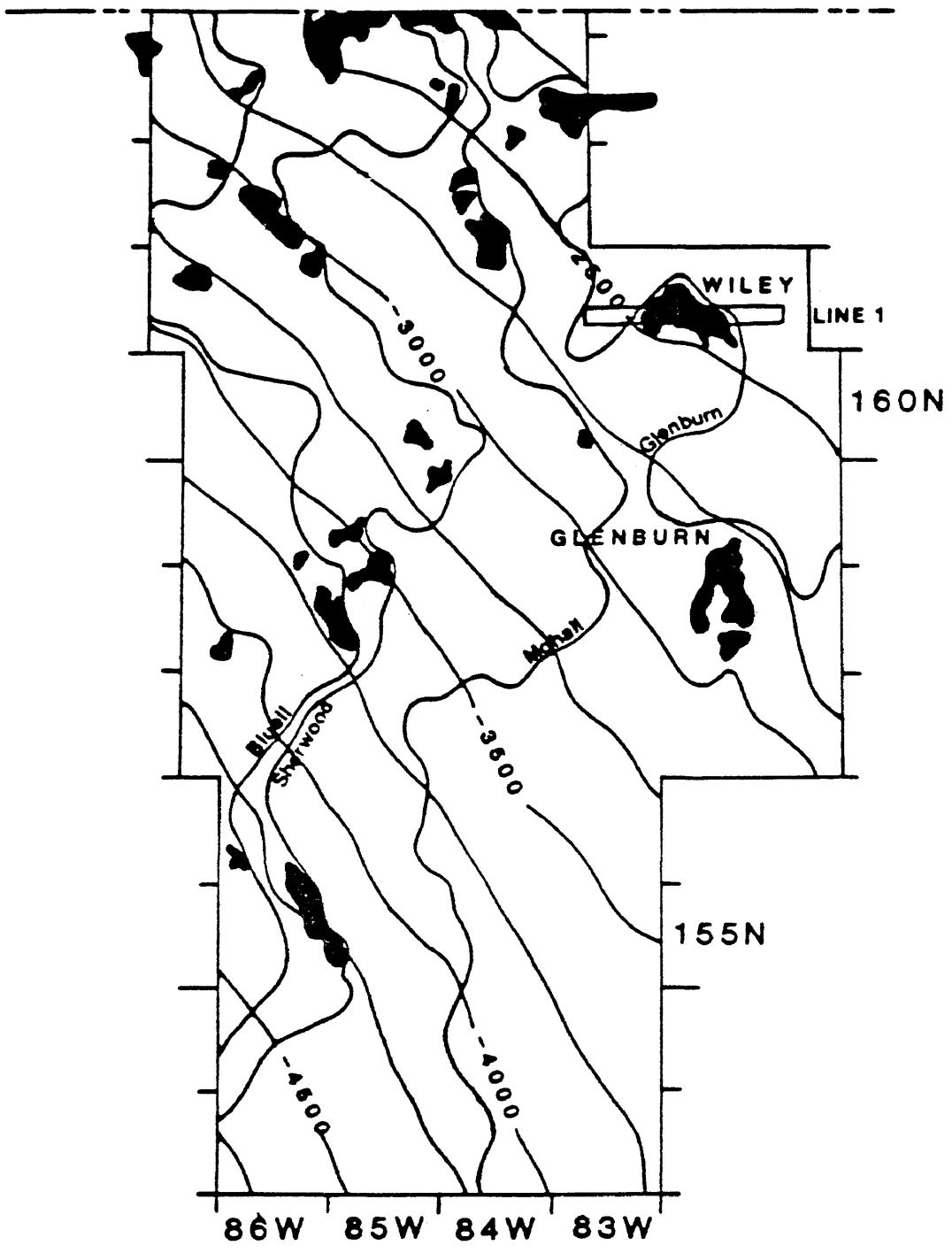

Figure 2. Base of "State A" structure with approximate easternmost edge of Bluell, Sherwood, Mohall, and Glenburn carbonates and location of seismic data (adapted from Reeve, 1986).

thesis by Donna Reeve (1986).

Seismic data were processed for amplitude analyses, by correcting for as many non-geological amplitude factors as possible. Models were prepared to compare with the seismic data by using compressional and shear velocities obtained from core laboratory measurements. Well data were integrated into the analysis.

Analyses of the seismic data included comparison of a zero-offset seismic model to the true-amplitude stacked section. Prestack analysis focused on summed CDP gathers and common offset stacks. The analysis led to observations that tuning effects were a limiting factor on the range of offsets that could be used. Changes in seismic character are more important for delineating the reservoir than changes in amplitude.

PREVIOUS WORK

Zoeppritz's equations govern the reflection and transmission of seismic wave energy in layered elastic media. Compressional and shear wave velocities and densities, along with angle of incidence at each interface, are parameters needed to solve the Zoeppritz equations.

(1) (a) Compressional (P) wave velocity (V_p) is the velocity in the medium when particle motion is parallel to the direction in which the wave is propagating, and is expressed as follows:

$$V_p = [(k + 4/3u)/d]^{1/2}$$

where k = bulk modulus
u = shear modulus
d = bulk density

(b) Shear (S) wave velocity (V_s) is the velocity in the medium when particle motion is perpendicular to the direction of wave propagation, and is expressed by:

$$V_s = [u/d]^{1/2}$$

(2) Poisson's ratio (POI) is a measure of deformation of a unit cube of material:

$$POI = - \frac{dw/w}{dl/l}$$

where w = width, dw = change in width

l = length, dl = change in length

Poisson's ratio can also be expressed as a function of V_p and V_s:

$$POI = \frac{(V_p/V_s)^2 - 2}{2(V_p/V_s)^2 - 2}$$

The range of Poisson's ratios for most materials is 0 to .5.

(3) At normal incidence, a P wave does not undergo mode conversion, but as the angle of incidence increases, the P wave incident will undergo mode conversion whereby part of the reflected and transmitted energy converts to shear wave energy.

(4) The bulk modulus, k, is a function of rock framework and interstitial pore fluids, but the shear modulus, u, depends on rock framework and grains since the

shear modulus of a fluid is zero.

Muskat and Meres (1940) used Zoeppritz equations to show that the reflection coefficients for plane P waves at a boundary showed a general slight decrease with increasing angle of incidence, however, their work did not include variations in Poisson's ratios on either side of the boundary.

Koefoed (1955) made calculations using formulas in the form given by Muskat and Meres (1940) and varied Poisson's ratios across an impedance boundary. He found a much larger change in reflection coefficients with angle of incidence. Figures 3 and 4 show the results of his calculations, and the general results of varying only V_p and POI across a boundary can be summarized as follows:

(a) For $V_{p2} > V_{p1}$ and $POI_2 > POI_1$, the reflection coefficient increases with increasing offset.

(b) For $V_{p2} > V_{p1}$ and $POI_2 < POI_1$, the reflection coefficient decreases with increasing offset.

(c) For $V_{p2} > V_{p1}$ and $POI_2 = POI_1$, the reflection coefficient decreases with increasing offset, with the effect becoming more noticeable as POI decreases.

(d) The effect in (a) is more pronounced as the velocity contrast becomes smaller.

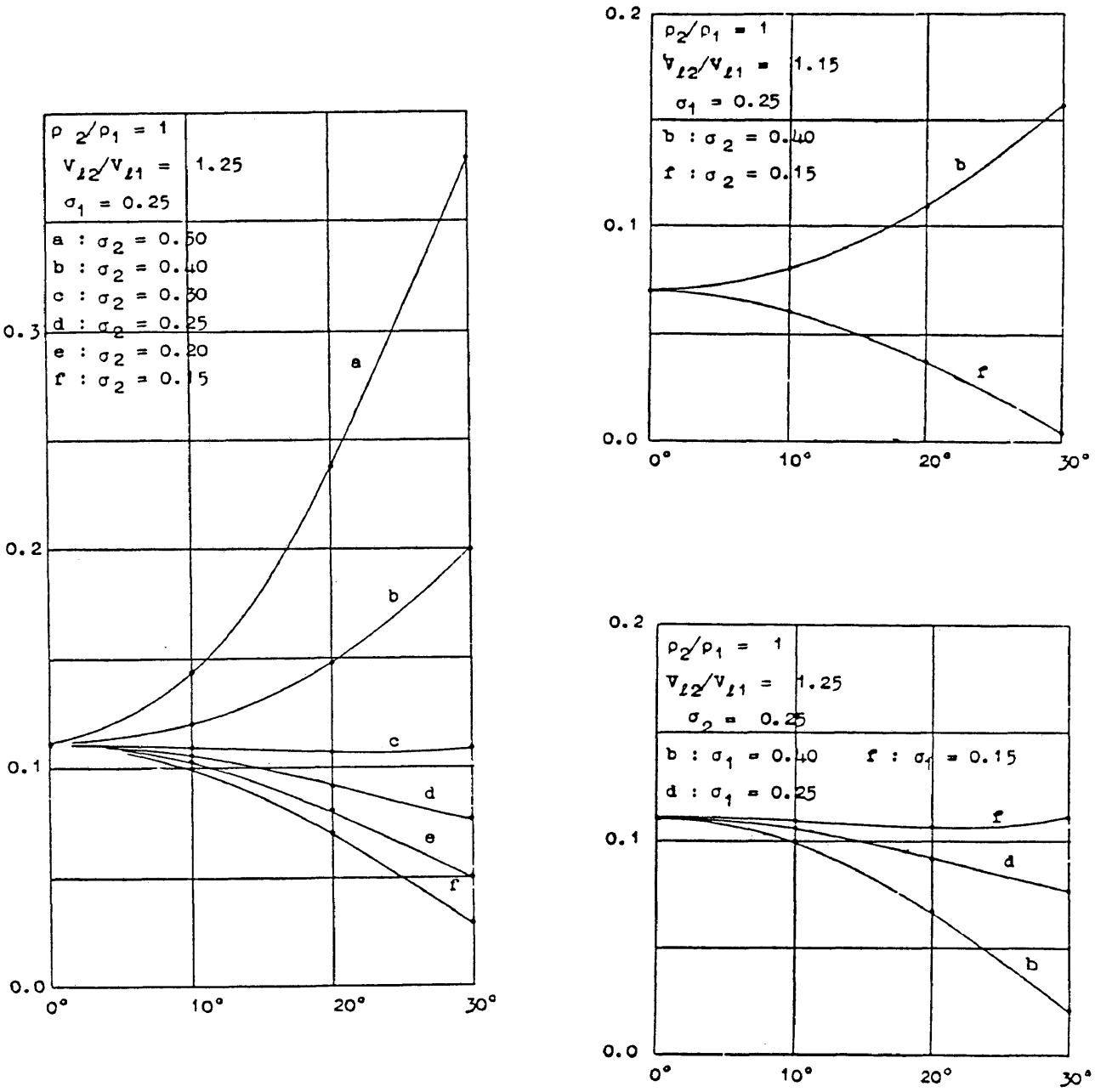

Figure 3. Reflection coefficient versus angle of incidence from Koefoed (1955). $Vp_2 > Vp_1$ and $d_1 = d_2$ for all cases.

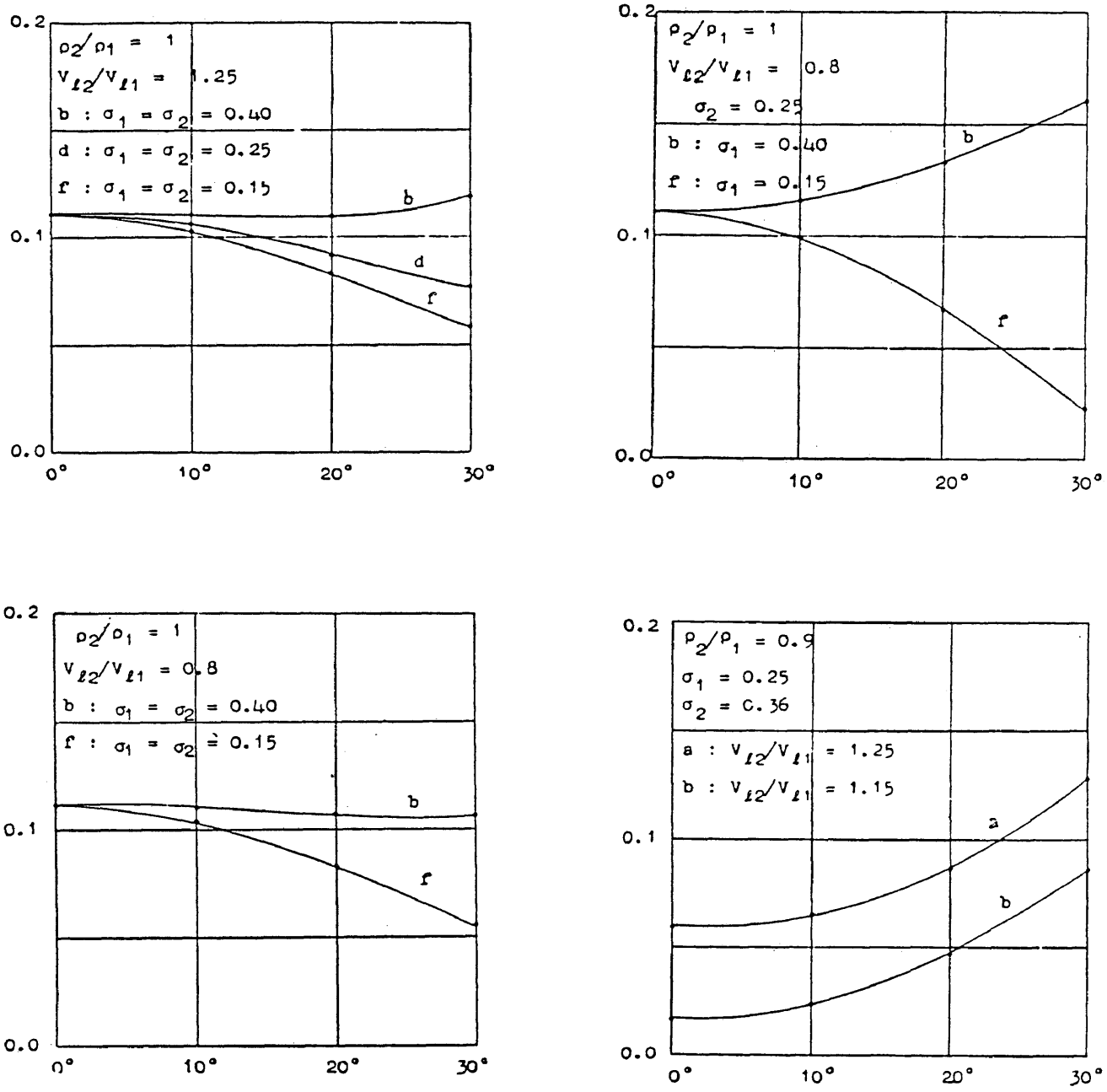

Figure 4. Reflection coefficient versus angle of incidence from Koefoed (1955).

(e) Interchanging the incident and underlying media affects the shape of the curves only slightly up to angles of incidence of 30°.

Koefoed (1962) analyzed changing V_p, POI, d, and their effect on reflection coefficients. Here he showed a general decrease in reflection coefficients with increasing angle of incidence. However, he did not investigate the case of reflected P-wave amplitude where V_{p2} is less than V_{p1} and simultaneously POI_2 is less than POI_1, which would be the case for gas-saturated rocks.

Gregory (1976) showed that lowering the P wave velocity can result in a decrease in V_p/V_s by up to 30% in consolidated rocks, which also corresponds to a decrease in Poisson's ratio. This decrease has been attributed to a change in the bulk modulus of the medium coupled with a lack of change in the shear modulus when pore fluid is changed (Gassman, 1951).

According to Almoghrabi and Lange (1986), seismic amplitudes are affected not only by pore fluids, which is primarily what offset-amplitude techniques have been used to detect, but also by layer thickness and surrounding lithology. The thickness of the layer of interest is an important factor in determining overall reflectivity due to possible interference of reflected wave components.

The lithology of adjacent rocks is an important influence on overall reflectivity because wide amplitude variations for P-waves and mode-converted S-waves occur when acoustic properties of the boundary layer are allowed to vary within the range of values typical for the lithology of interest. Amplitude analysis alone is not sufficient to define pore fluid, but when amplitude analysis is combined with phase and mode-converted shear wave behavior, it may be possible to differentiate between pore fluids.

Almoghrabi and Lange (1986) developed an integrated system to interpret seismic data, and published graphs of amplitude versus angle of incidence (Figure 5) for reflected and transmitted P-wave and mode-converted S-waves for boundaries between a sandstone saturated with either brine or gas (BS, B or GS, G, respectively) and shale and between limestone and shale (LS, L). The graph in the lower half of Figure 5 shows the curve for a 20 meter limestone bounded by shale (LS), while the graph in the upper half of Figure 5 shows the curve for a 3 meter limestone bounded by shale (L). These two graphs illustrate the effect that changing the thickness of the bed can affect the amplitude-offset curves. However, the study does not include the case of an anhydrite-carbonate boundary which is the case for the reservoir at the Wiley

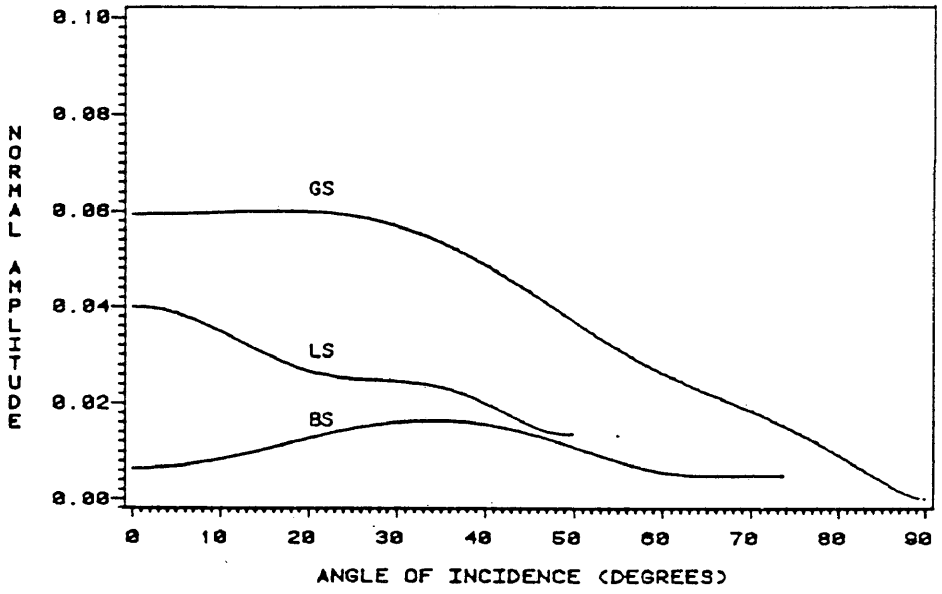

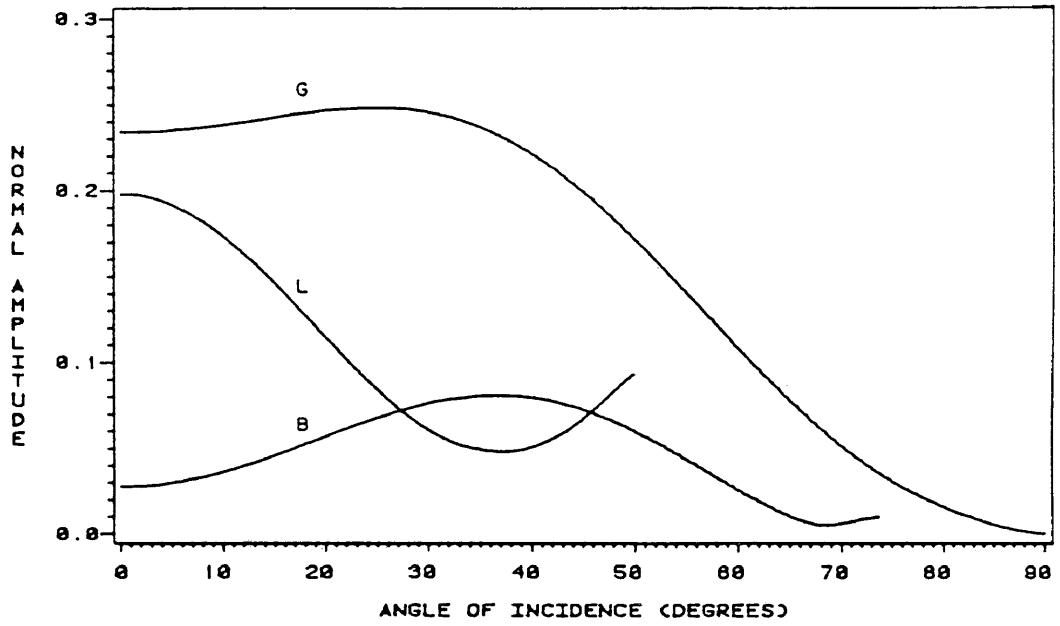

Figure 5. The normal component of the reflected amplitude of P-waves for an incident frequency of 40 Hz and a layer of either sandstone saturated with gas or brine or limestone, bounded by shale (from Almoghrabi and Lange, 1986). (a) layer thickness is 3 m. (b) layer thickness is 20 m.

Field. The importance of bed thickness and tuning effects will be discussed in this thesis as well.

Robertson (1987) used P-wave and S-wave seismic sections to determine whether variations in porosity in the Paleozoic Hunton Group in the Anandarko Basin could be detected as variations in P- and S-wave traveltimes and/or traveltime ratios. Robertson concluded that variations in P- and S-wave traveltimes delineated lateral variations in the thickness of the Hunton, and variations in the S/P traveltime ratios corresponded to lateral variations in Hunton porosity. Robertson observed that

> **"where the pore space is saturated with liquid, a systematic increase in average porosity from less than 2 percent to about 11 percent correlates with an S/P traveltime ratio from 1.84 to 1.96",**

which corresponds to POI of .29 to .32. Somewhat lower S/P traveltime ratios at several places along the line probably indicated partial gas saturation. Robertson stated that the trend of increasing S/P traveltime ratios with increasing porosity appears to be consistent with the seismic response of a petrophysical model in which the pore shapes are predominantly elongated rather than round.

GEOLOGY

The Wiley Field is located in the northeast portion of the North Dakota Williston Basin in Bottineau County. Oil production occurs primarily from the Mississippian Mission Canyon Formation, with sourcing from the Devonian Bakken Formation (Dow, 1974; Figure 6). Trapping mechanisms are structural-stratigraphic associated with facies changes from carbonate to anhydrite within the Frobisher-Alida interval of the Mission Canyon Formation (Reeve, 1986).

During the Mississippian, deposition along the northeastern edge of the Williston Basin was related to an epeiric sea covering the basin. Intertidal and subtidal carbonates and supratidal evaporites were deposited in a prograding tidal flat, coastal plain, environment (Shanley, 1983; Figure 7). At Glenburn Field to the south of the study area, porosity in the limestone reservoir was developed subaerially by diagenesis on topographic features related to paleostructures due to Devonian Prairie salt solution on the flanks of the field (Gerhard, 1985).

Reeve (1986) constructed well-log cross-sections, structure maps, and isopach maps in order to develop a

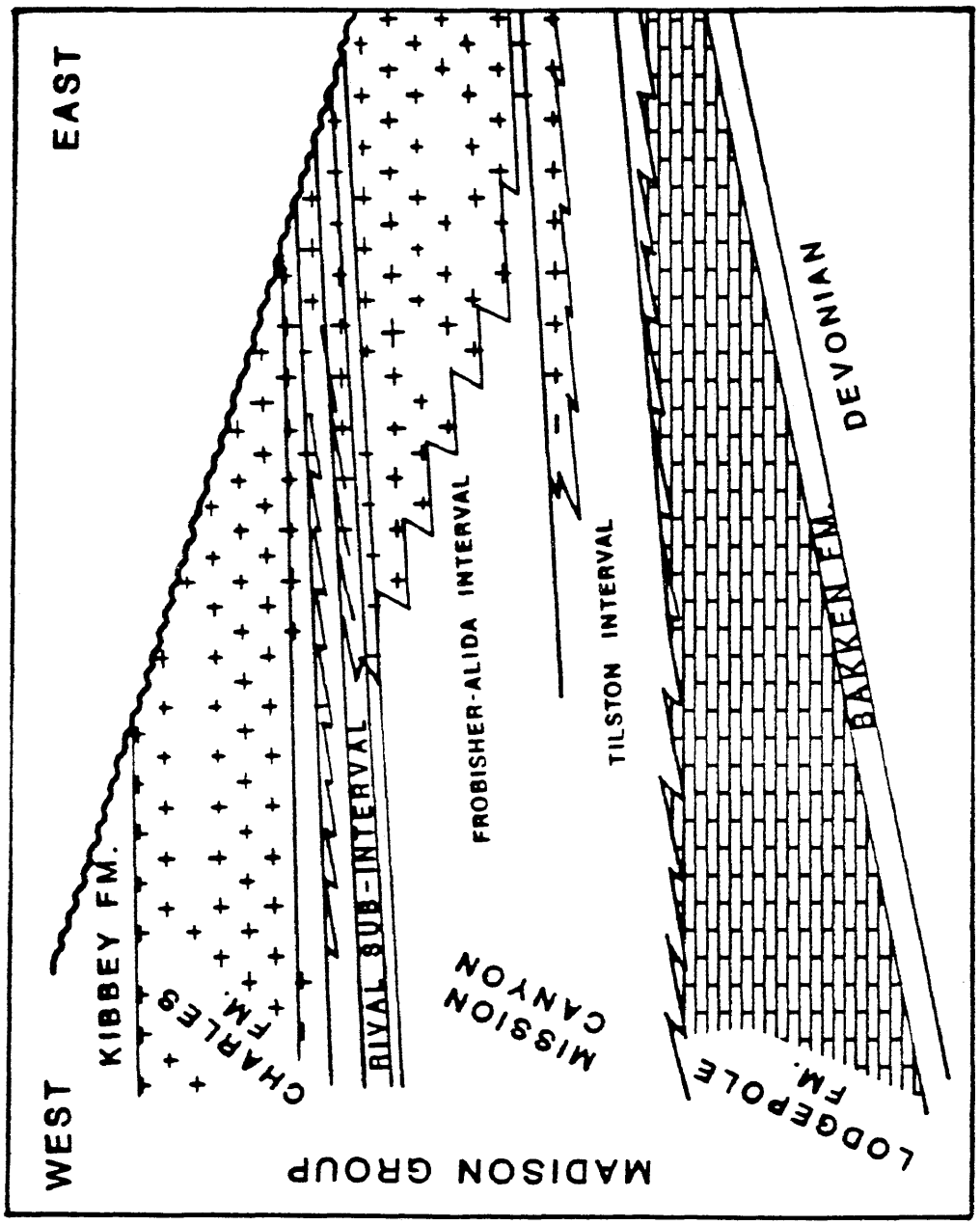

Figure 6. Generalized stratigraphic section for the Madison Group (from Reeve, 1986).

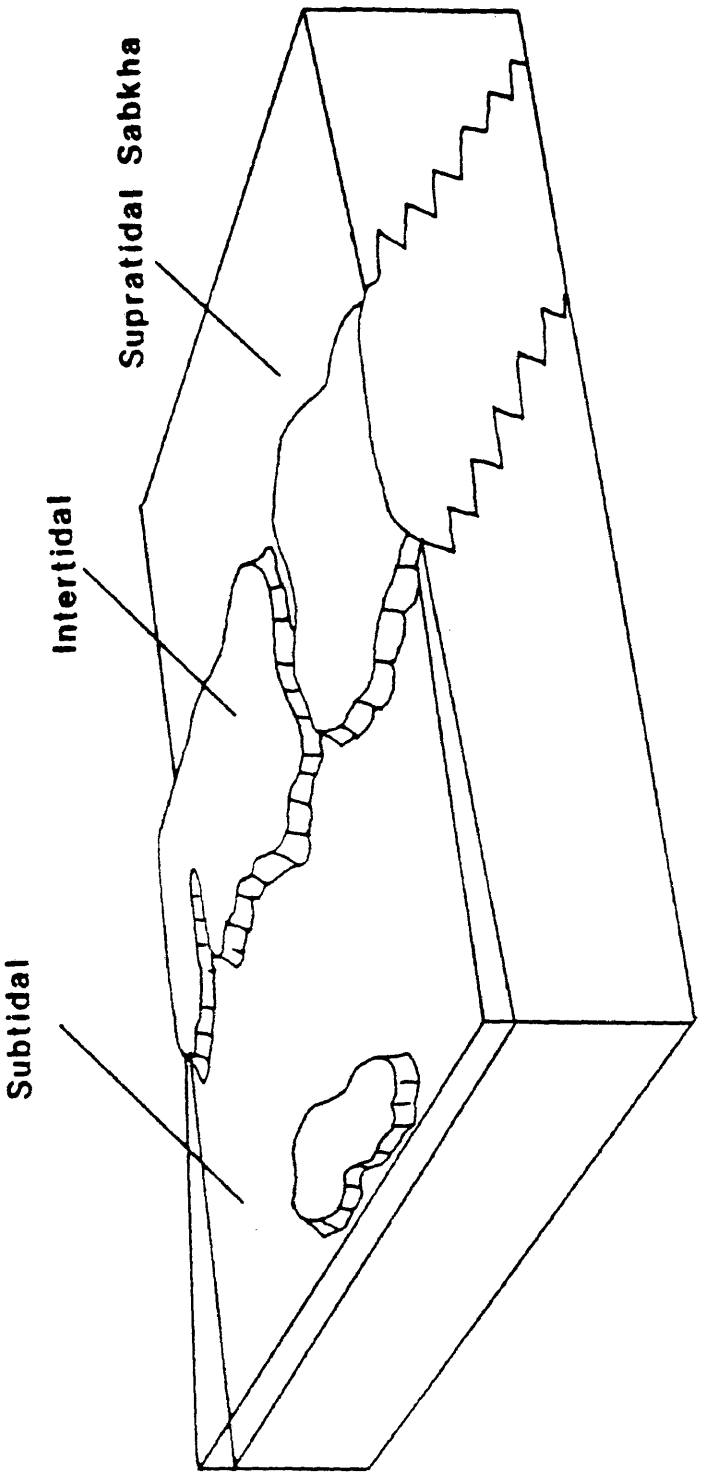

Figure 7. Depositional environment, Wiley and Glenburn Fields (from Reeve, 1986).

geologic model for the Wiley Field and to determine what factors might have controlled reservoir development. Production at the Wiley Field is from the Glenburn porous carbonate facies in the Frobisher-Alida interval (Figure 8). Massive anhydrite and anhydrite infilling of the limestone porosity form an updip permeability barrier.

Due to a facies change from intertidal carbonate to supratidal anhydrite, the anhydrite thickens off-field and thins over the Wiley field. The Glenburn carbonate facies appears to be related to a paleohigh in the Wiley Field, as indicated by the truncation of younger units by a pre-Pennsylvanian unconformity above the reservoir interval and to the east of the field (Figure 9).

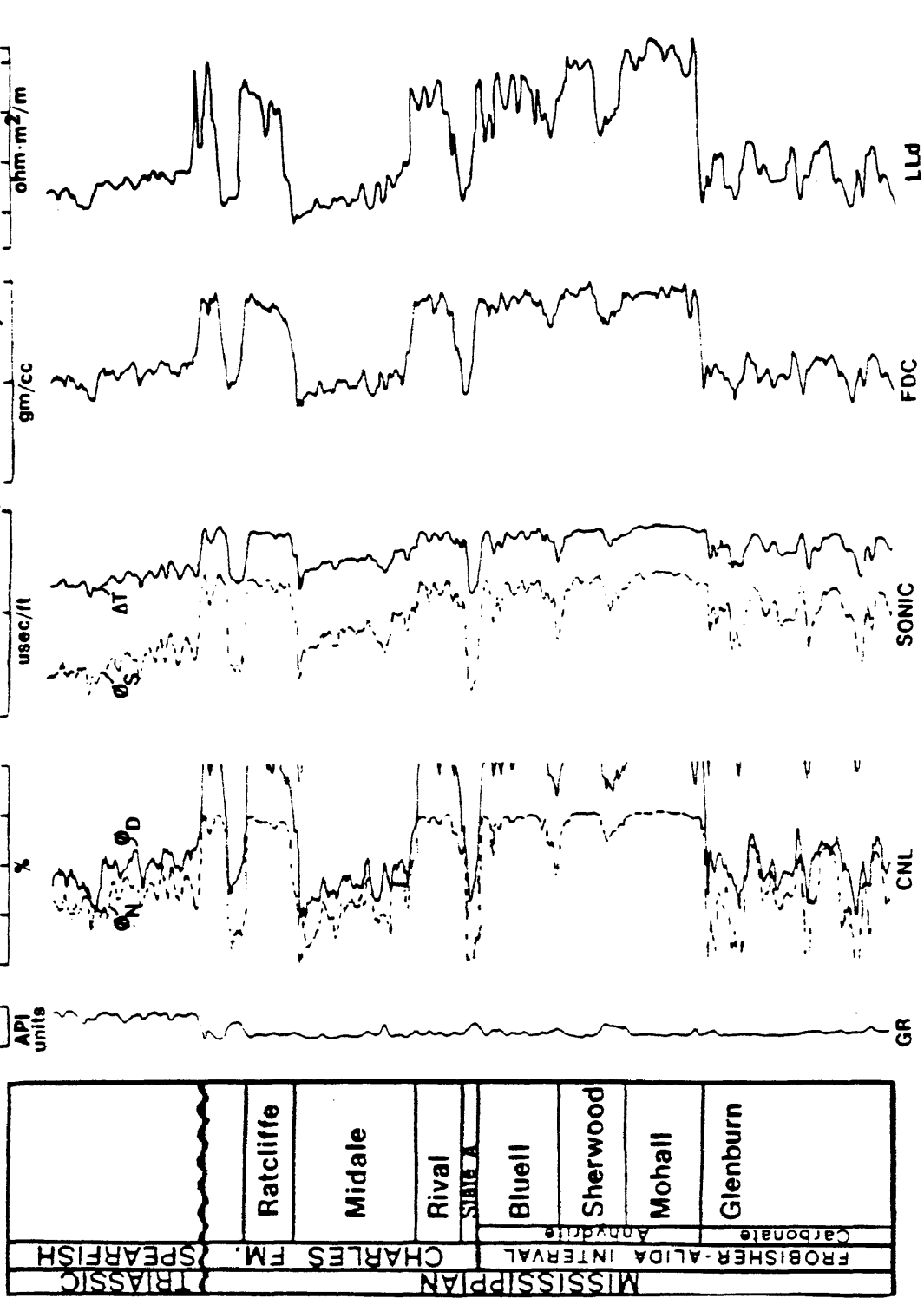

Figure 8. Well log response, Frobisher-Alida interval, Cities Wiley Rice 1-A, sw/sw/nw 27-161N-82W, Wiley Field (from Reeve, 1986).

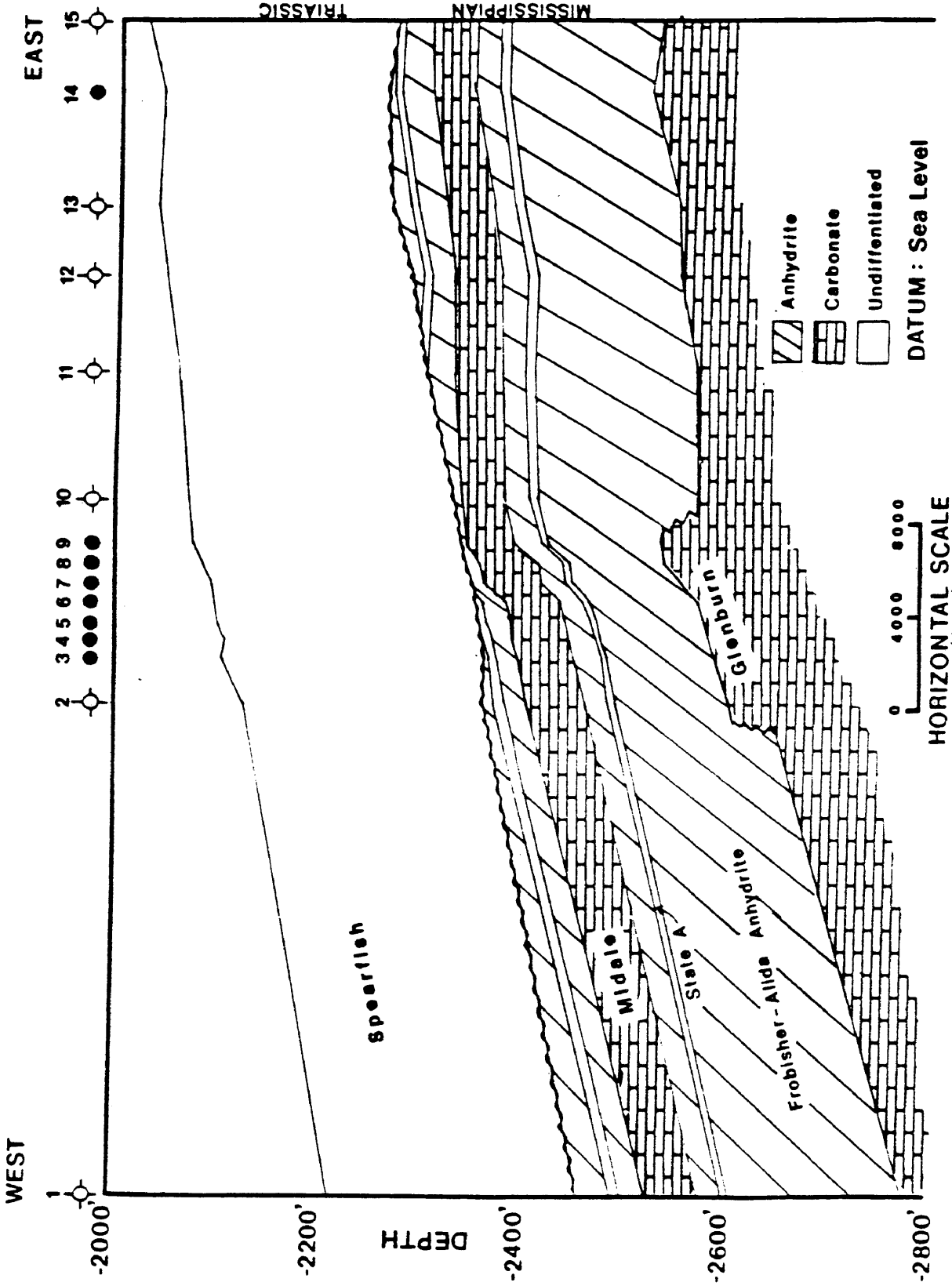

Figure 9. Schematic cross-section, Wiley Field (from Reeve, 1986).

PROCESSING

According to Ostrander (1984), there are many factors that affect amplitudes as a function of offset :

(1) Reflection coefficient

(2) Array attenuation

(3) Event tuning

(4) Noise

(5) Spherical spreading

(6) Emergence angles

(7) Reflector curvature

(8) Spherical wavefronts

(9) Transmission coefficients

(10) Instrumentation/processing

(11) Inelastic attenuation

Since the reflection coefficients are the information we wish to extract, we should correct for as many of the other factors as is possible. Array attenuation occurs because source and receiver are not point-source and point-receiver. At far offsets, the apparent dip of the reflector becomes large and the geophone array tends to reduce the amplitude of these reflections. Ostrander does not suggest a specific processing scheme to correct for array attenuation but suggests that a plot be made of

array attenuation versus two-way traveltime and shot-to-group offset, such as the one shown in Figure 10. Such a plot could be taken into consideration when interpreting the amplitude-offset data.

Correction for noise depends upon the type of noise present. Offset dependent noise may have an effect on data-dependent amplitude balancing, therefore such amplitude balancing should operate on data which have the highest signal-to-noise ratio. It may be necessary to avoid near offset traces in vibrator data sets when amplitude balancing, since these are often very noisy.

Spherical spreading causes a predictable decay in seismic amplitude with increasing time and offset. There are several approximations to correct for spherical divergence. Ordinarily a simple zero-offset correction is applied for data which will be stacked, but for amplitude-offset analysis, a correction which takes distance into account should be applied.

Amplitude balancing is a phase of processing which can be extremely critical for any kind of amplitude analysis. Balancing which takes into account variations in source and receiver strength, also called surface-consistent amplitude balancing, should be applied if

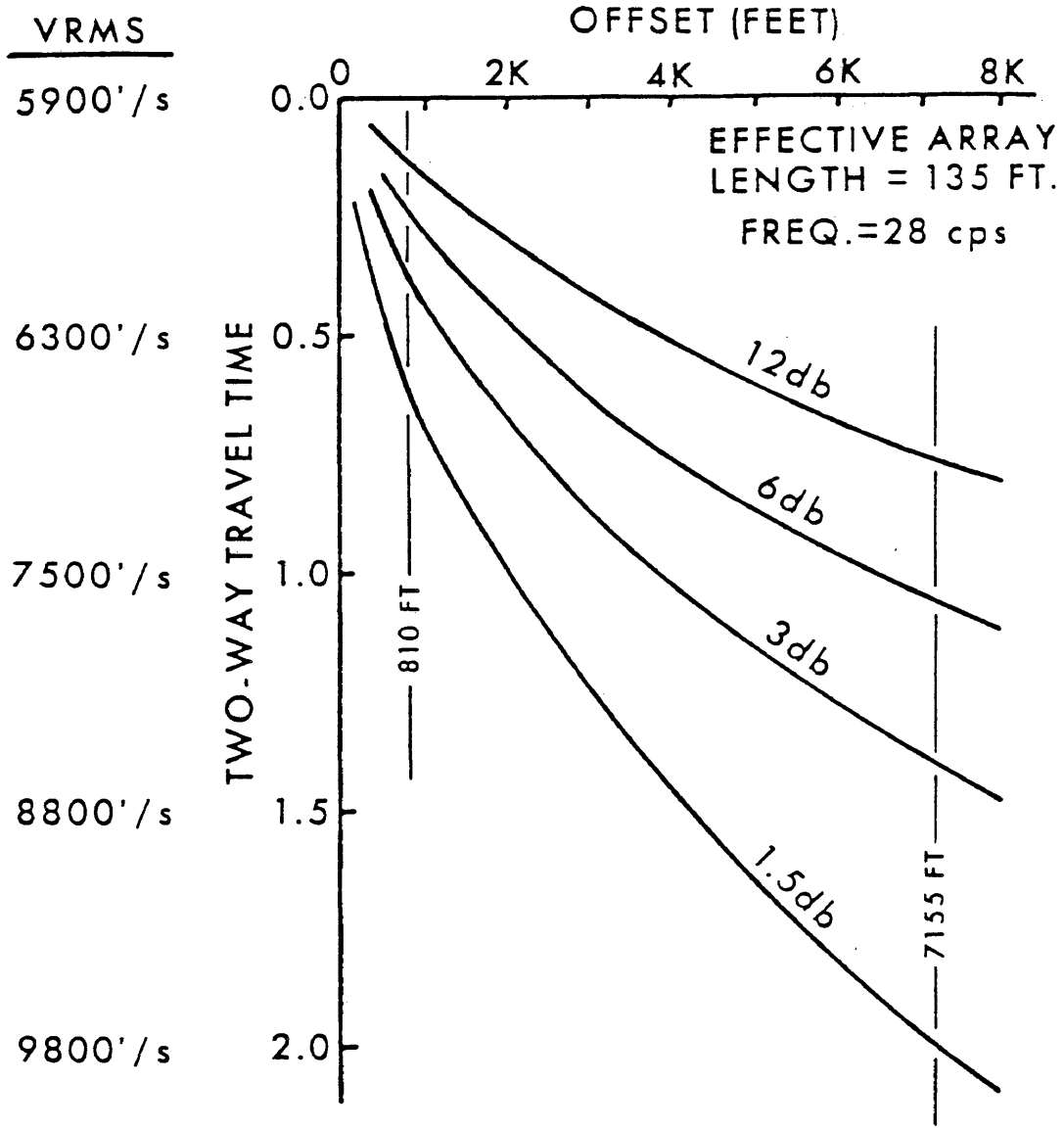

Figure 10. Array attenuation versus two-way travel time and shot-to-group offset, for an effective array length of 135 feet (from Ostrander, 1984).

there seems to be a noticeable variation (Ostrander, 1984; Yu, 1986). This approach corrects for the instrumentation/inelastic attenuation. Trace equalization over very long time gates may sometimes be used as a final step in processing, but can also lead to undesireable results (Ostrander, 1984; Yu, 1986).

Table 1 gives the acquisition parameters for the seismic line; the processing sequence for seismic line 1 is shown in Table 2. Brief explanations of those processing steps that the author does not consider to be standard will be explained below.

Surface-consistent deconvolution attempts to stabilize the seismic signature by taking into account variations in source strength and coupling and receiver coupling. The procedure involves first using spiking deconvolution in the shot domain using a single deconvolution operator for each shot record. The use of a shot domain operator should eliminate amplitude variations due to merge zones between operators, such as would occur when a four trace window is specified for the operator. The shot domain deconvolution is then followed by sorting the traces into the receiver domain and following a procedure similar to that followed in the shot domain.

Table 1. Acquisition parameters for the seismic line.

Line 1

Date: 1978

Source Parameters

Source: Vibroseis
Sweep: 12-96 Hz linear
Number of Sweeps: 6
Number of vibrators: 4
Source array length: 70 feet
Sweep length: 13 sec

Recording Parameters

Instrument: LRS 888
Sample rate: 2 msec
Record length: 3 sec
Filter: 6-124 Hz, notch out
Number of channels: 96

Geophone Arrays

Geophone: unknown
Geophones per group: 24
Group interval: 150 feet

Spread Configuration

Vibrator interval: 300 feet
Coverage: 2400%
Geometry: split spread
Near offset: 450 feet
Far offset: 7500 feet

Table 2. Processing sequence for the seismic line.

Demultiplex

Geometry Definition

Trace Edit

--------- Testing Phase: the following steps are for computational purposes only ----------

Spherical Divergence Correction for preliminary processing (standard zero-offset correction)

Testing Deconvolution for preliminary processing (4-trace operator, shot deconvolution only)

Refraction Datum Statics

Velocity Analysis

Brute Stack

Automatic Residual Statics

Velocity Analysis

Automatic Residual Statics

---------- Main Processing Phase: the following steps were applied to the original, demultiplexed data ----------

True Amplitude Recovery

Surface Consistent Deconvolution

Surface Consistent Amplitude Balancing

Final Velocity Analysis

Final and Partial Stacks

The refraction datum statics program used for this thesis computes a data-dependent solution based on Gardner's Time Delay Method. The delay times induced by velocity variations in the weathering layer are computed from a model that is based on digitized first break refractors. This model is then added to the previously computed datum statics subsurface model which is based on an empirical derivation using estimated weathering velocities.

The residual statics were computed by an automated program using an iterative computational technique to converge on a surface-consistent residual statics solution. Statics were computed by cross-correlating gated traces to a CDP pilot model. The computed statics have a zero-mean CDP shift that improves the stacking response without introducing structural distortion.

True amplitude recovery is a time-variant restoration to compensate for wave-front spreading or spherical divergence and amplitude loss due to absorption or inelastic attenuation. One form of the spherical divergence compensation may be approximated by T^x where T is traveltime and x may vary from -2 to 2, depending on the velocity gradient. T^2 should approach the correction for velocities increasing linearly in time. A more general

equation for true amplitude recovery is

$$A(T) = \text{scalar}(T)[T^x][10^{aT/20}]$$

where scalar(T)[T^x] is the spherical divergence correction and $10^{aT/20}$ is the inelastic attenuation correction factor. Scalar(T) is a scalar function of time, and a is an exponentiation factor in decibels/second. For a true amplitude recovery that uses distance instead of time to approximate a correction that includes the offset domain, it is possible to input x = 1 and substitute average P-wave velocities for scalar(T). This gives

$$\text{scalar}(T)[T^x] = V(T)*T,$$

where V(T) is the average P-wave velocity function. This is a commonly used form of the spherical divergence correction, and is the correction used in processing the data for this thesis.

Surface-consistent amplitude balancing was accomplished using a scaling process to remove amplitude effects due to variations in source and receiver strengths. This procedure leaves relative amplitudes unchanged, in both space and time. The procedure used shot records first, then receiver gathers, as did the surface-consistent deconvolution. Windows were chosen to

exclude coherent noise and include data where the signal to noise ratio is the highest. The average amplitude of the ensemble within each window was calculated and the midpoint of the window was multiplied by a scalar which was calculated using the number of non-zero points in the window. Points on the trace between window midpoints were multiplied by scalars derived by linear interpolation. However, in this case, there was one window encompassing all the data down to 2700 ms, so there was no linear interpolation necessary.

Partial stacks and summed CDP gathers were output by vertically stacking six CDPs for twelve offset ranges to enhance signal to noise ratios while retaining offset information. This resulted in summing over a 900 foot lateral range, and resulting offsets spaced by 600 feet.

MODELING

Reeve (1986) developed two-dimensional zero-offset seismic models for the Wiley field using Evergreen Geophysical Associates software. Models generated using wavelets of varying bandwidths are included here for comparison with the stacked section.

Figure 11 shows the acoustic impedance model for the Wiley Field with the Glenburn interval indicated as the horizon of interest. The seismic response of the impedance model to a zero-phase 5-10-85-95 hertz wavelet is shown in Figure 12; the facies change from porous carbonate to anhydrite is expressed as a change from a trough doublet to a poorly developed peak with a strong trough below.

Theoretical studies by Gassaway (notes from short course) have predicted that Poisson's ratio should increase with increasing porosity for fluid-filled rocks. Gassaway's method used the Voight-Reuss-Hill method to calculate elastic moduli and P- and S-wave velocities for non-porous rocks. Experimental data from Domenico and Gregory were analyzed to determine the effect of fluid-filled and gas-filled porosity. Gassaway's method of calculating Poisson's ratios indicated a trend of

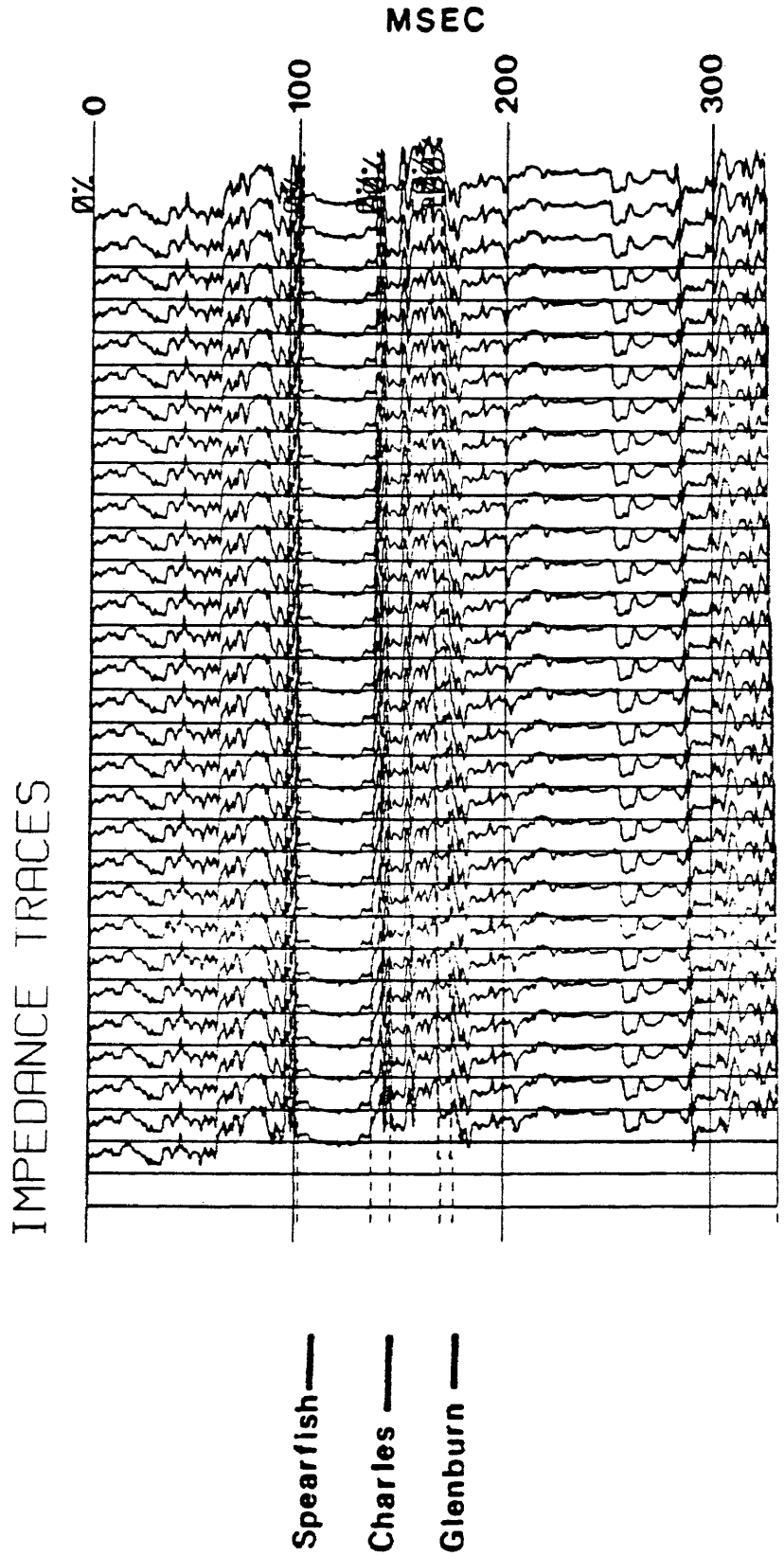

Figure 11. Acoustic impedance model for Wiley Field (from Reeve, 1986).

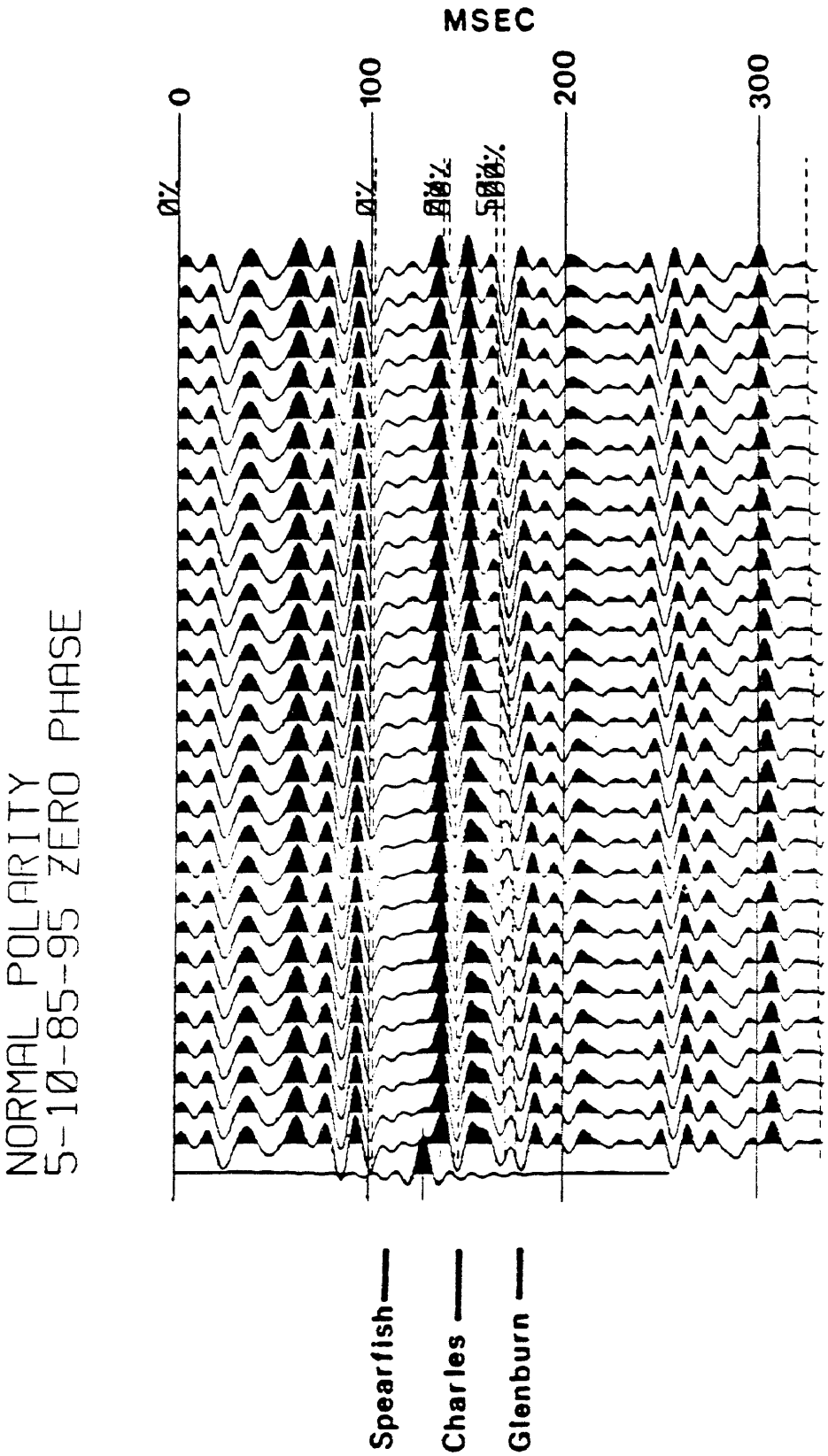

Figure 12. Wiley Field model response to a zero-phase 5-10-85-95 Hz wavelet (from Reeve, 1986).

increasing Poisson's ratio with increasing porosity for brine-filled carbonates.

Laboratory and field studies have shown conflicting results for Poisson's ratio-porosity trends: Robertson (1987) shows an increase in Vp/Vs (or equivalently, Poisson's ratio) with increasing porosity if the pores are flat, but a slight decrease in Poisson's ratio with increasing porosity if the pores are more spherical. Laboratory measurements on carbonates near the study area (Rafavich, 1984) suggest a trend of decreasing Poisson's ratio with increasing porosity, which would agree with the spherical-pore model cited by Robertson. Figures 13, 14, and 15 show the trend of Poisson's ratio versus porosity for the three most abundant lithologies from Rafavich's study: limestone, dolomite, and dolomitic limestone, respectively. For all three lithologies, there was much scatter in the Poisson's ratios of the air saturated samples, which were plotted as squares, so it was difficult to determine the trend of the data points. It was not obvious whether there was a linear trend for the air saturated samples. For the brine-saturated limestone samples, which were plotted as a plus sign, there appeared to be a linear trend of decreasing Poisson's ratio with increasing porosity, although the range of porosities for

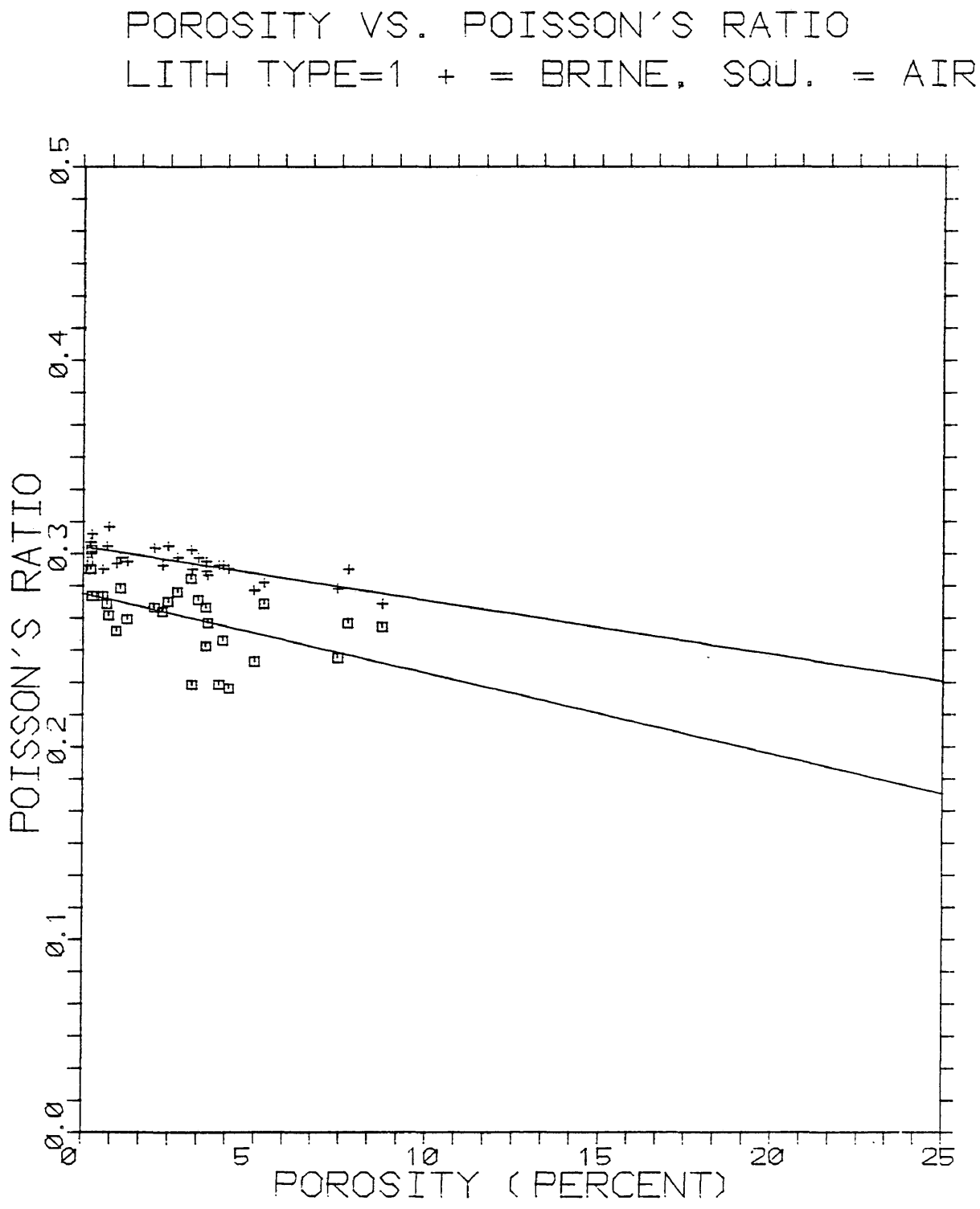

Figure 13. Porosity versus Poisson's ratio for limestone; + = brine saturated, square = air saturated. Data from Rafavich (1984).

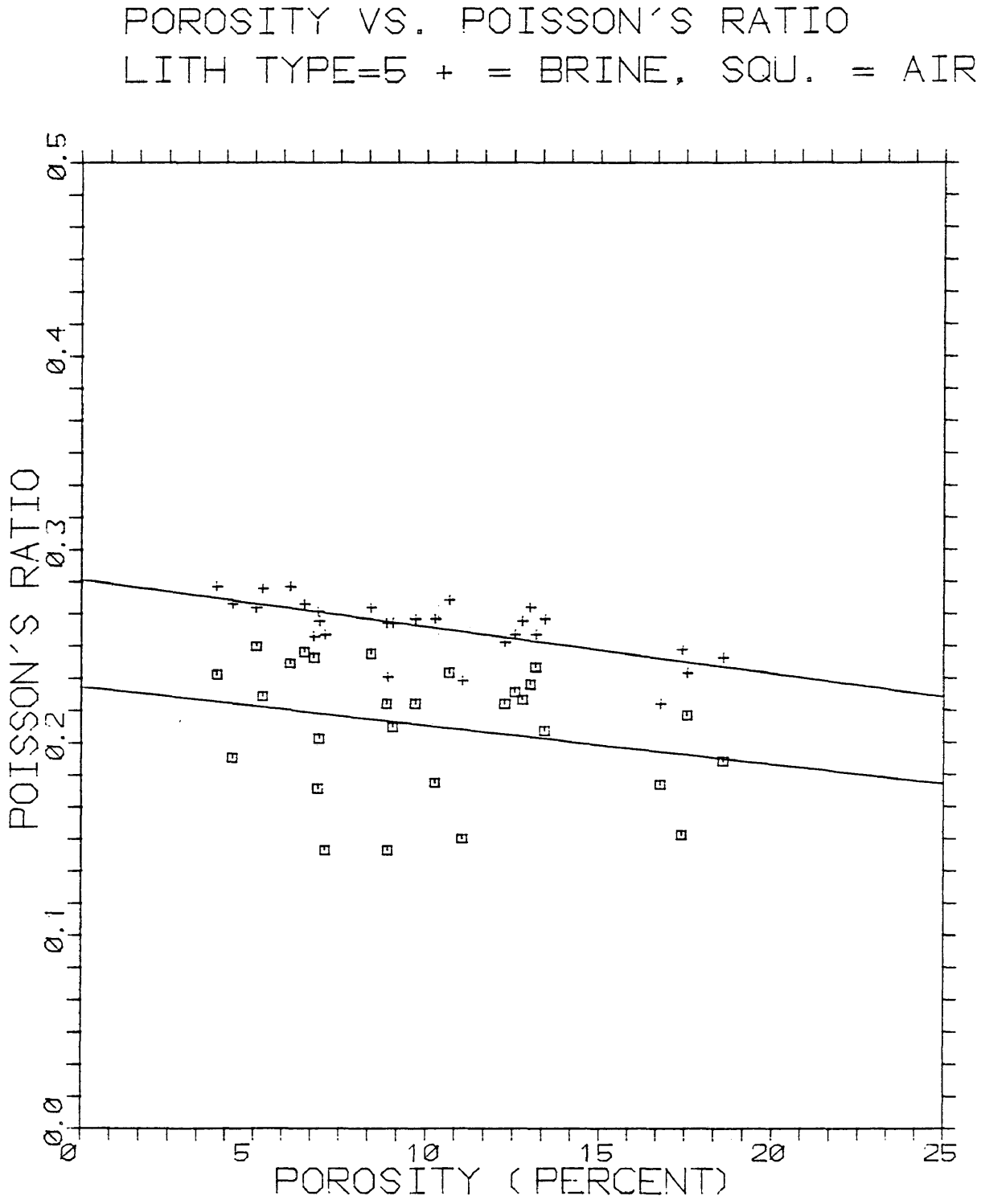

Figure 14. Porosity versus Poisson's ratio for dolomite; + = brine saturated, square = air saturated. Data from Rafavich (1984).

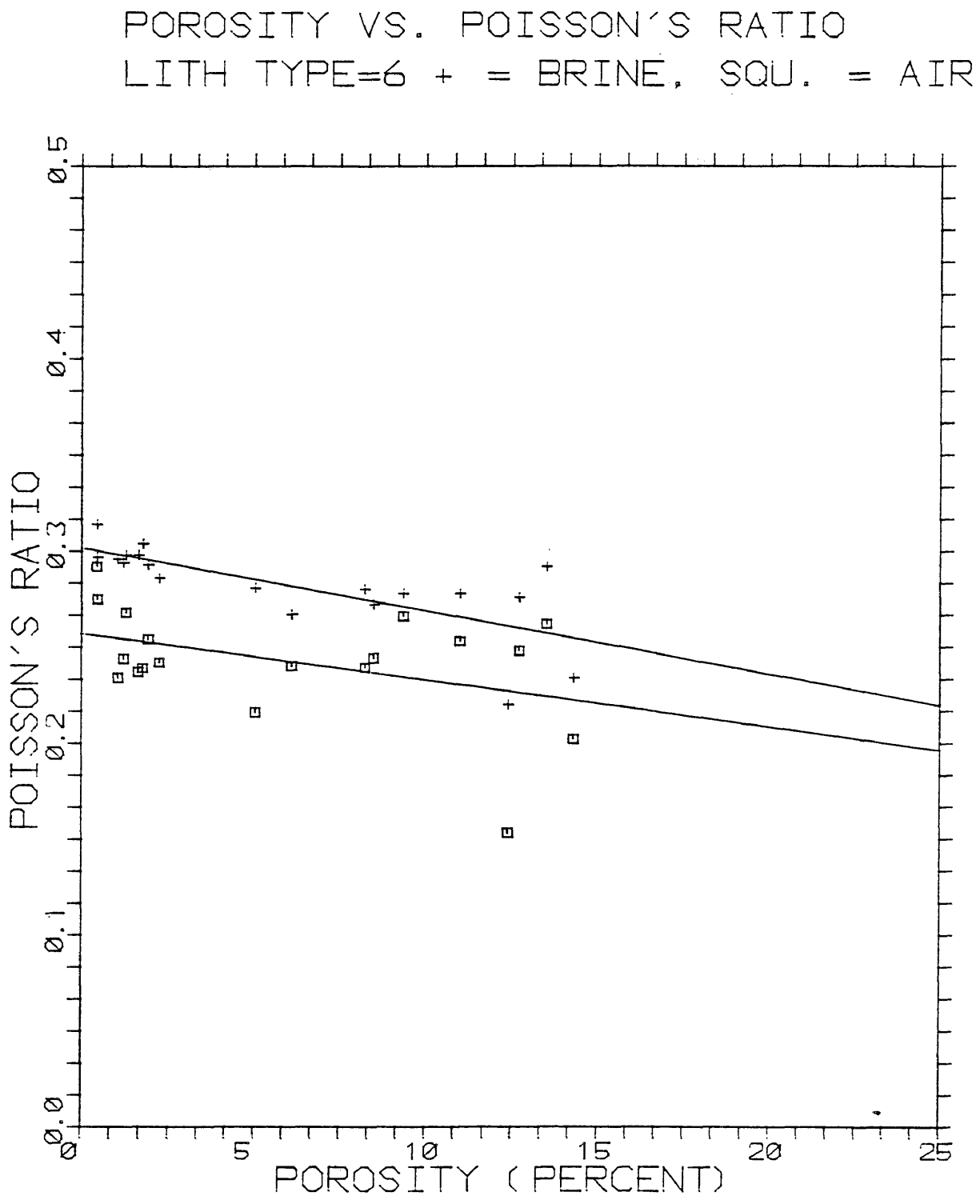

Figure 15. Porosity versus Poisson's ratio for dolomitic limestone; + = brine saturated, square = air saturated. Data from Rafavich (1984).

this lithology was rather small. The brine-saturated dolomite and dolomitic limestone lithologies had a greater range of porosities as well as more scatter in the Poisson's ratios, but there still appeared to be the suggestion of a decrease in Poisson's ratio with increasing porosity.

Because of the lack of agreement in the literature related to rock properties in carbonates, especially the relationship between porosity and Poisson's ratio, it was determined that core measurements for V_p and V_s should be made for the Wiley Field study area. Cores were available from the U.S.G.S. Core Library in Denver for the Inexco Oil Co. Olsen #1-12 and Monsanto #2 Ring wells. These cores were part of a suite of core descriptions made by Shanley (1983) in his stratigraphic analysis of the Mission Canyon Formation. Although neither well is in the Wiley field, they were the closest wells with cores available from Shanley's study. The Inexco Olsen #1-12 is rather far away but the reservoir is considered to be similar to that at the Wiley field; the Mohall rather than the Glenburn is the producing interval there. Figures 16 and 17 show the well log character for these cores and the depths at which cores were available.

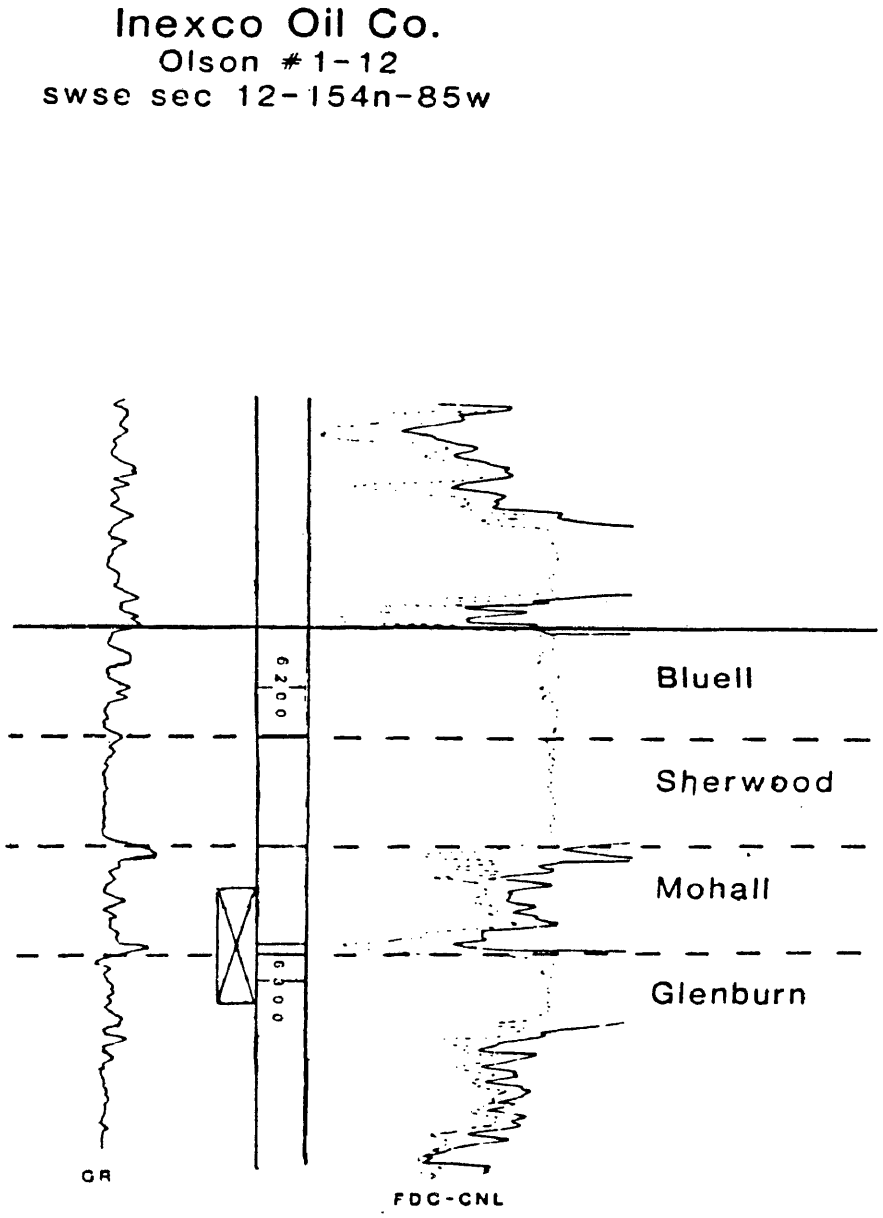

Figure 16. Well log character and depths of core for Inexco Olson #1-12 (adapted from Shanley, 1983).

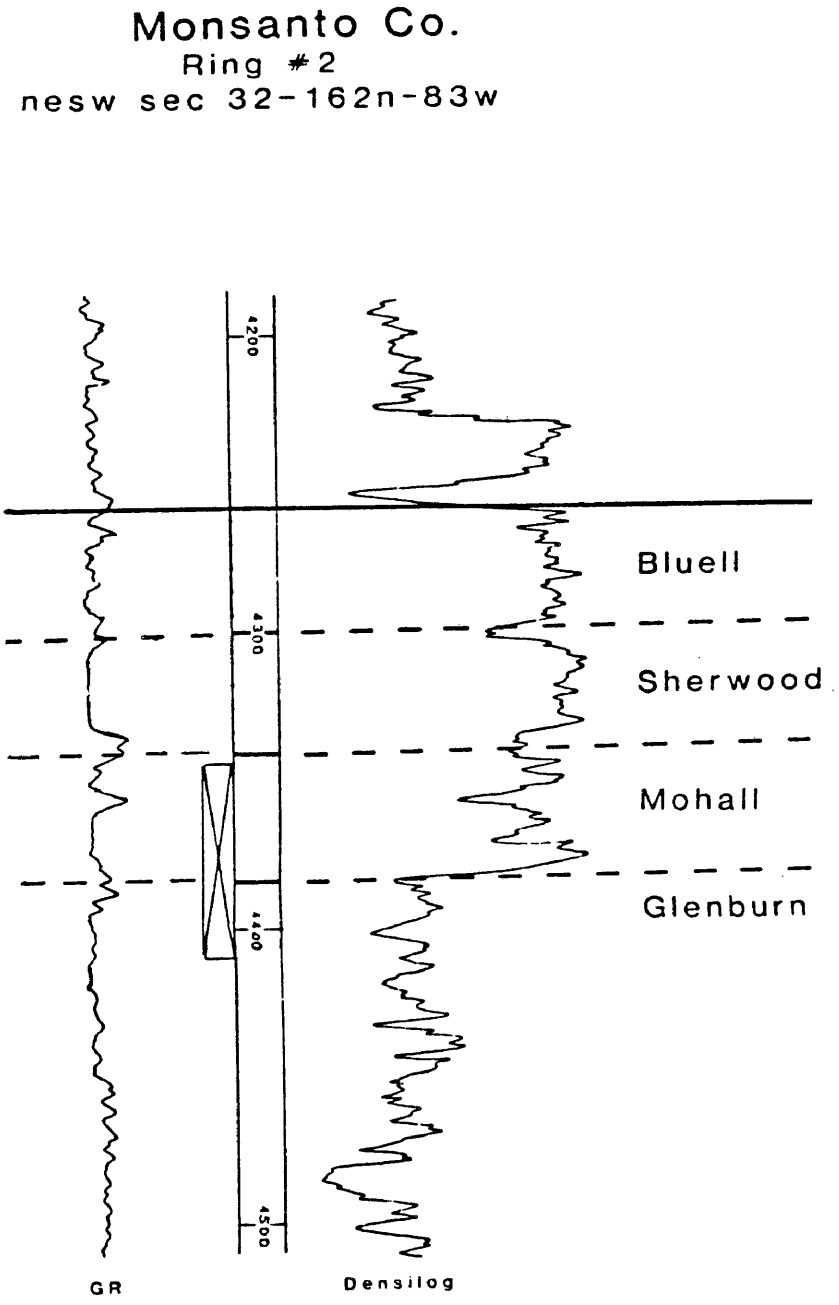

Figure 17. Well log character and depths of core for Monsanto Ring #2 (adapted from Shanley, 1983).

A field study by Chiburis (1987) showed a trend of increasing amplitude with increasing offset for oil saturated carbonates at depths of 2000 to 3000 feet. Although the target depth of the study area is deeper than for Chiburis' study, an investigation was undertaken to determine if it would be possible to detect oil-filled carbonates as opposed to brine-filled carbonates by an increase in amplitude with increasing offset.

Core Measurements

Poisson's ratio from laboratory measurements can be used for compressional reflectivity calculations if effective pressures that correspond to those at depth are used. For this study, target depths were approximately 4000 feet. Corresponding overburden pressures were determined to be 4000 to 5000 psi, based on a generally accepted overburden pressure gradient of 1 psi/foot (Domenico, 1985). Domenico analyzed the relationship between V_p and V_s and rock lithology and porosity using laboratory core measurements. That study assumed that differential pressure increased at a rate of .57 psi/foot, based on the theory that velocity is principally dependent on differential or effective stress or pressure rather

than geostatic or pore fluid pressure separately. According to Domenico (1985), the generally accepted rate for geostatic pressure is 1 psi/foot and that for pore fluid pressure due to brine in the pore spaces is .43 psi/foot, which leads to a differential pressure gradient of .57 psi/foot.

Core measurements were made on samples that were, on the average, 0.97 inches in length and 1.0 inch in diameter.

Values needed for modeling were porosity, bulk density, V_p, V_s, and POI. Porosity and density were calculated using the Archimedes method, which uses samples weighed wet, dry, and submerged in pore saturant. Density and porosity were based on these weights for each sample. P- and S-wave velocities were calculated using travel times measured using equipment at PBT, Inc. in Golden, Colorado. Figures 18 and 19 show the apparatus used for the travel-time measurements. The apparatus is designed so that confining pressure and pore pressure can be controlled. A toggle switch allows P- and S-wave traveltimes to be measured at precisely the same pressures. Appendix 1 lists sample measurements and derived quantities needed for modeling. Samples were taken to maximize lengths of samples, however, the average

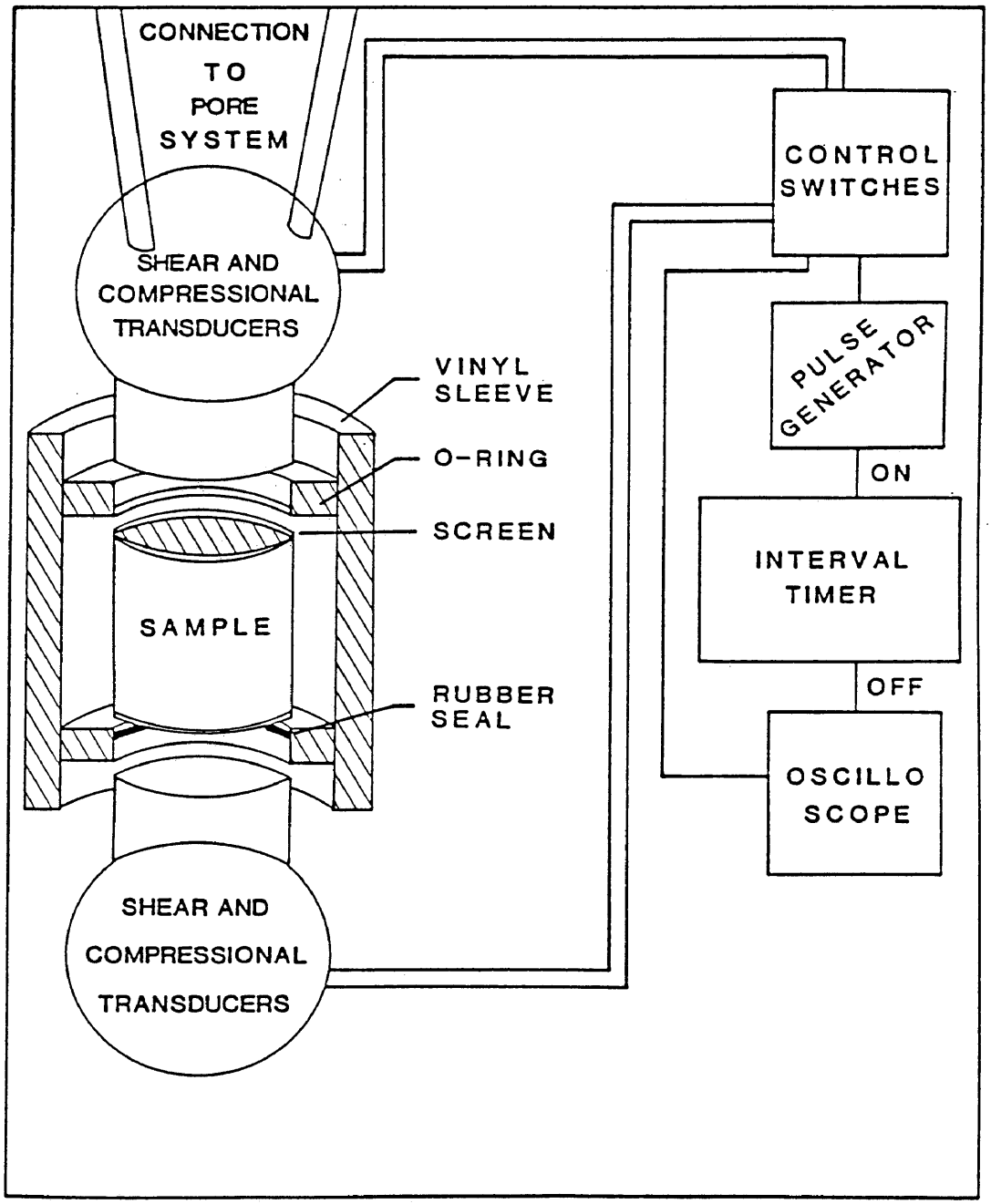

Figure 18. Diagram of the electrical system and sample housing used to measure velocities of core samples (from Mueller, 1987).

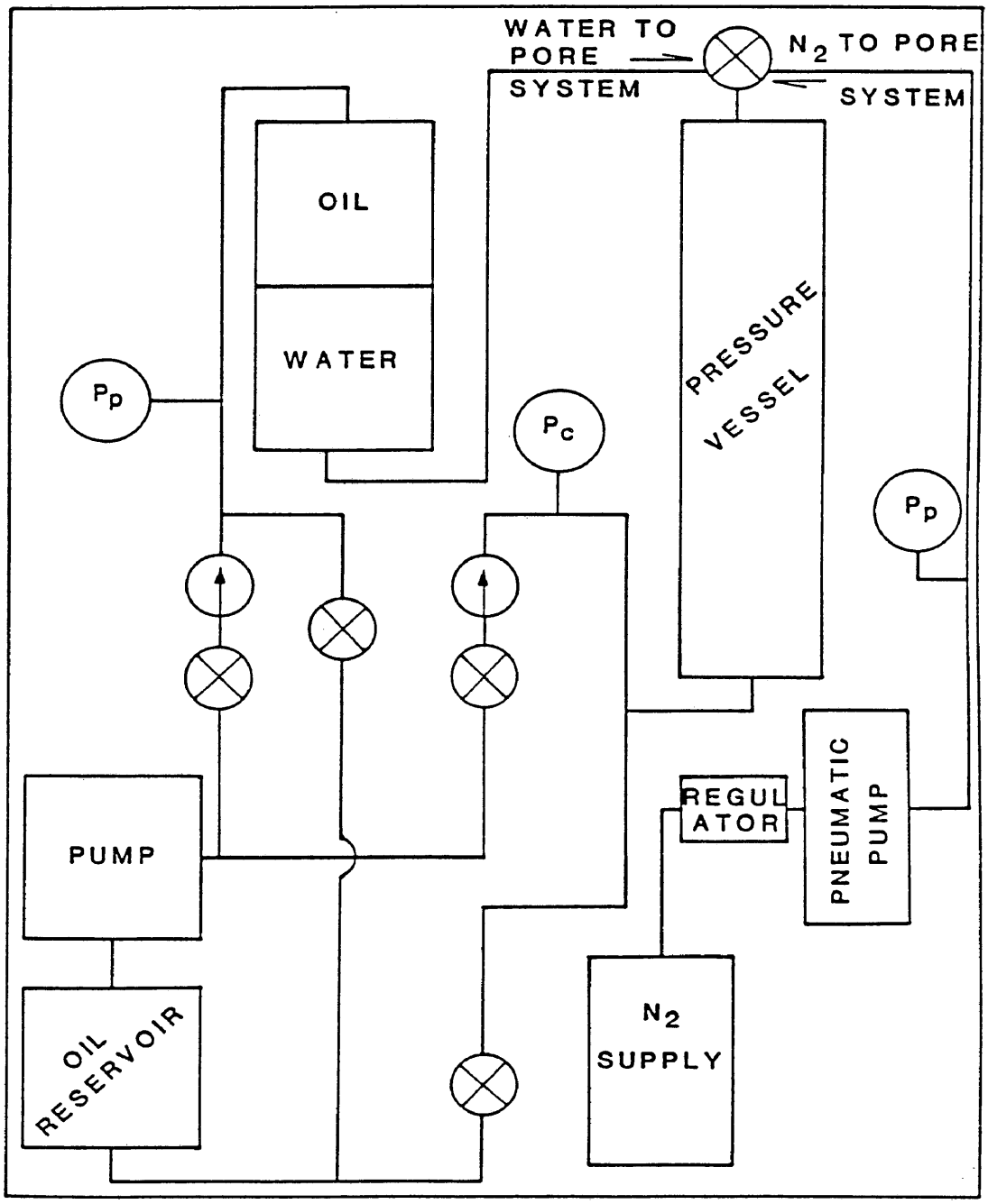

Figure 19. Diagram of the hydraulic system used to measure velocities of core samples (from Mueller, 1987).

length was only approximately 1 inch.

Velocities were calculated using transit times through the samples:

$$\text{Velocity} = \frac{1}{(T_t - T_{tr})/L_s} * 12 \times 10^6$$

where T_t = transit time

T_{tr} = time through transducers

L_s = length of sample

Upon comparison of P-wave velocities measured from the core with velocities indicated by the sonic logs in the area, it was evident that the velocities measured from cores were somewhat higher than expected. Because there were no shear wave data available for comparison, it is not known whether the core-derived S-wave velocities are correspondingly high.

Velocities were measured at two different pore pressures, while confining pressure was varied to maintain the same effective pressure. Average velocities were calculated as the average of the two measurements at each effective pressure. Poisson's ratios from the cores used in this study were calculated by plotting average

velocity squared vs. the cube root of effective pressure for P- and S- wave velocities, which gives an approximately straight-line relationship (Towle, 1978) and using the ratio of the equations of the lines for V_p^2 and V_s^2 at a pressure of 5000 psi. A pressure of approximately 2500 psi should have been used , given the depth of the Glenburn, but the higher pressure actually used only caused a 2 to 4% reduction in the Poisson's ratios for the samples, which is insignificant. Figures 20 and 21 are representative of the best fit lines for V_p and V_s for a sample. The graphs for the remaining samples are contained in Appendix 2. Although the number of samples was small for the core measurements made in this thesis, the results appeared to support the trend indicated by the study by Rafavich (1984), i.e. Poisson's ratio slightly decreasing with increasing porosity, rather than that suggested when Gassaway's method was used.

Modeling for amplitude-offset analysis was performed using two different modeling programs: a program developed in the CSM Geophysics Department by Ma Xiochun (1986) and AIMS* III.

*Trademark of GeoQuest

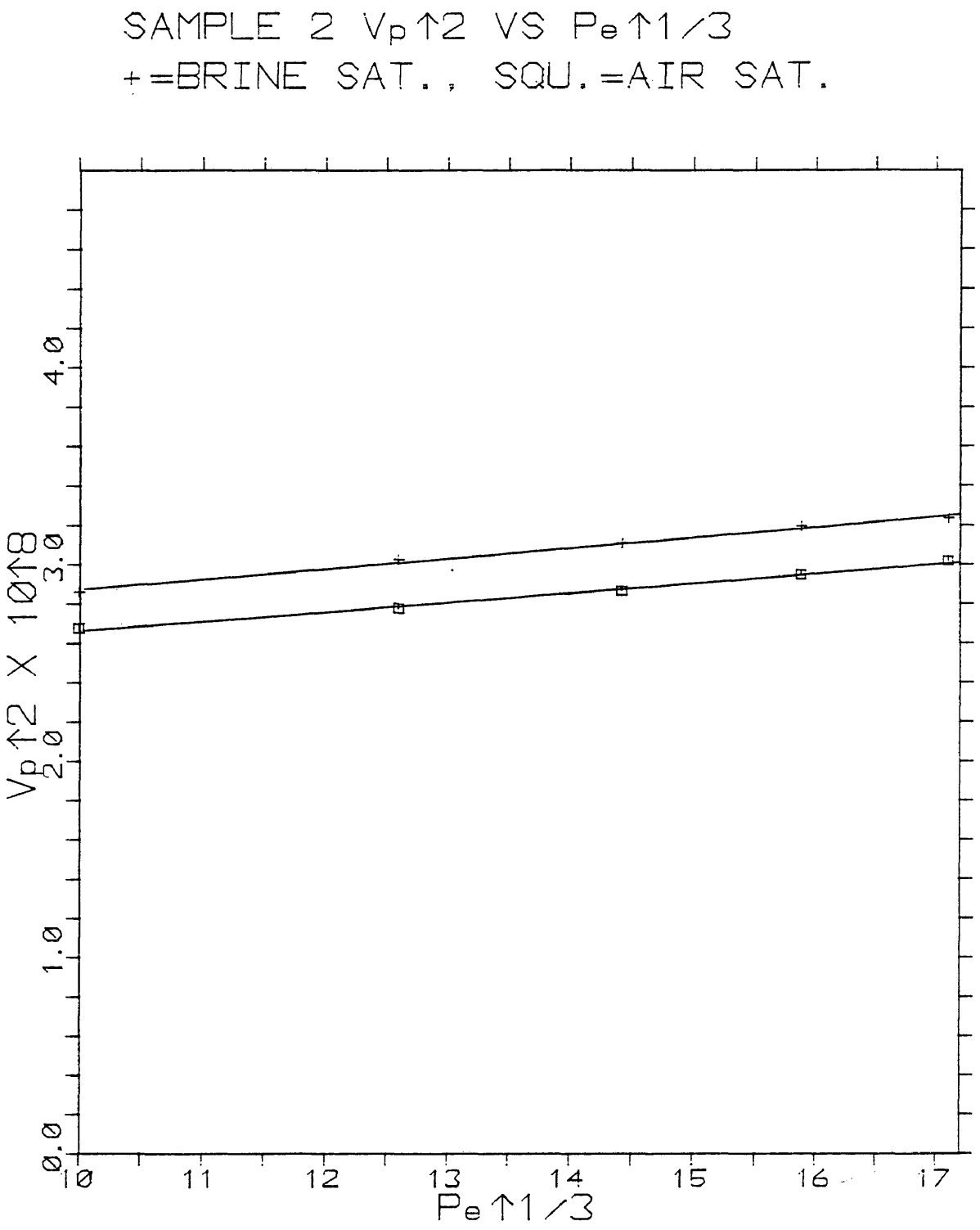

Figure 20. Vp^2 versus $(Pe)^{1/3}$ for sample 2 for brine and air saturated rock (from Inexco Olson #1-12).

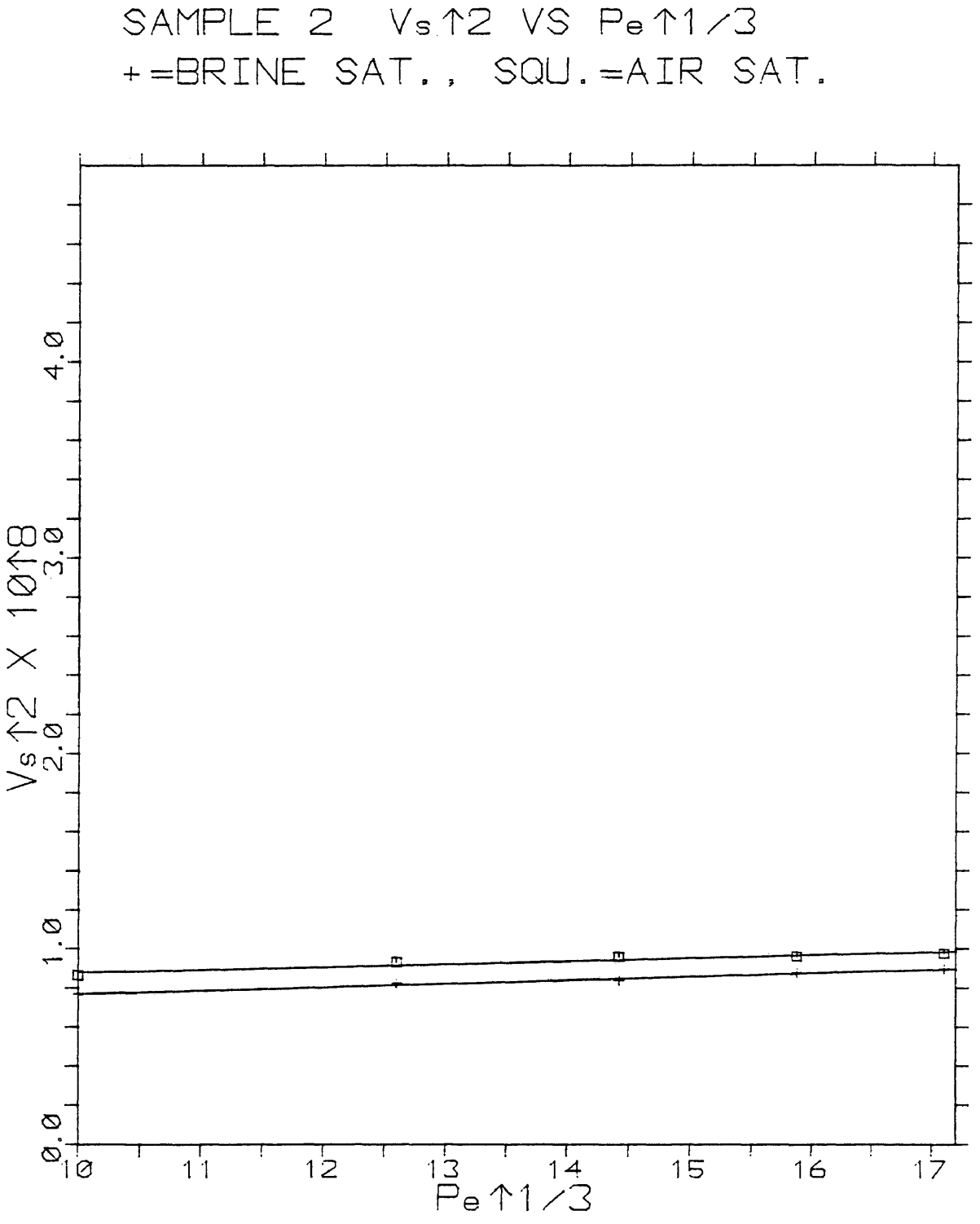

Figure 21. Vs^2 versus $(Pe)^{1/3}$ for sample 2 for brine and air saturated rock (from Inexco Olson #1-12).

Zoeppritz equation program

Ma Xiaochun's Zoeppritz program used Nafe's (1957) general solutions for Zoeppritz equations in terms of energy and amplitude for an interface for reflected and transmitted P- and S-waves. The user inputs the type of incident wave desired (P or S), and P-wave velocity, density, and Poisson's ratios for both media. The program then calculates reflected and transmitted P- and S-wave energy and amplitude.

Velocity and density measurements for both the Zoeppritz equation program and AIMS* were obtained from well logs near the seismic line. Poisson's ratios were obtained from core measurements except for two cases. The Poisson's ratio for the shale layer was obtained from a table of rock properties included in Gassaway's short course notes. The Poisson's ratio for the Gassaway porous carbonate was calculated using the method outlined in the course notes.

Figure 22 shows the graph of the program's output for a shale-anhydrite interface, which corresponds roughly to the Top of Paleozoic unconformity. The reflected P- and S-wave amplitude curves show a dramatic increase approaching a 45° angle of incidence, which should

*Trademark of GeoQuest

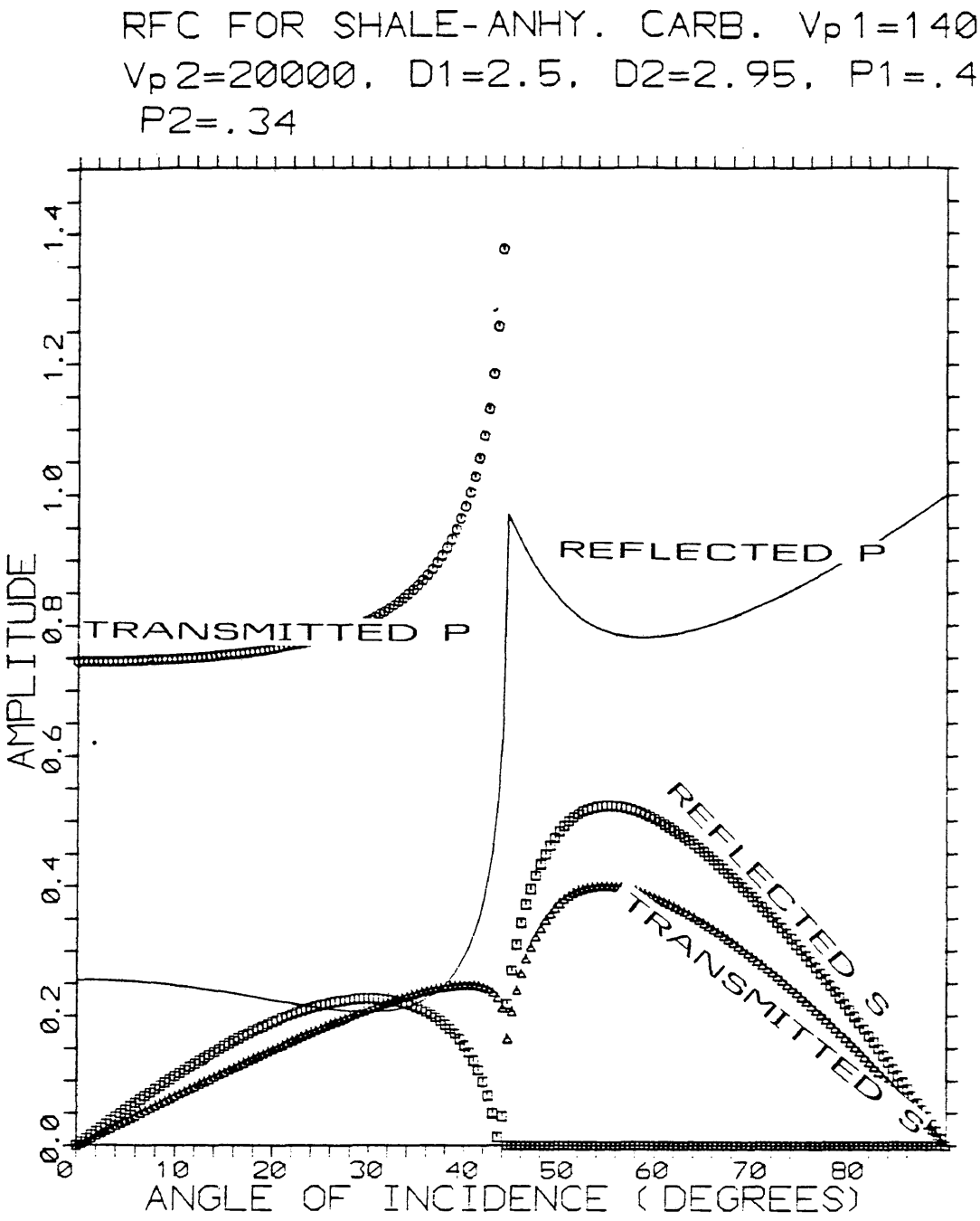

Figure 22. Amplitude versus angle of incidence for a shale-anhydrite interface. Vp_1 = P-wave velocity for layer 1, D_1 = density for layer 1, P_1 = Poisson's ratio for layer 1.

correspond to the critical angle.

Figures 23 and 24 show the amplitudes for an anhydrite-"porous carbonate" boundary. Due to the lack of agreement in the literature about the Poisson's ratios of porous fluid-filled carbonates, models were generated using Poisson's ratios obtained from core measurements (Figure 23) and from Gassaway's method (Figure 24). The plots show that while zero-offset reflected P-wave amplitudes are the same for both models, the amplitude decreases faster with increasing offset using the Poisson's ratio from Gassaway's method.
The plot for an anhydrite-"non-porous carbonate" model (Figure 25) shows lower zero-offset reflected P-wave amplitude, but not much change in amplitude with offset in the range of angle of incidence estimated to correspond to that in the real seismic data.

Although the graphs of amplitude versus offset from Xiochun's program do not show a great difference between the response of the non-porous and porous carbonates, they do lead to an important observation. Because the carbonates at the Wiley Field are overlain by a higher velocity anhydrite layer, most of the P-wave energy from the carbonates is transmitted rather than reflected, which means that very little energy from the carbonate layers is

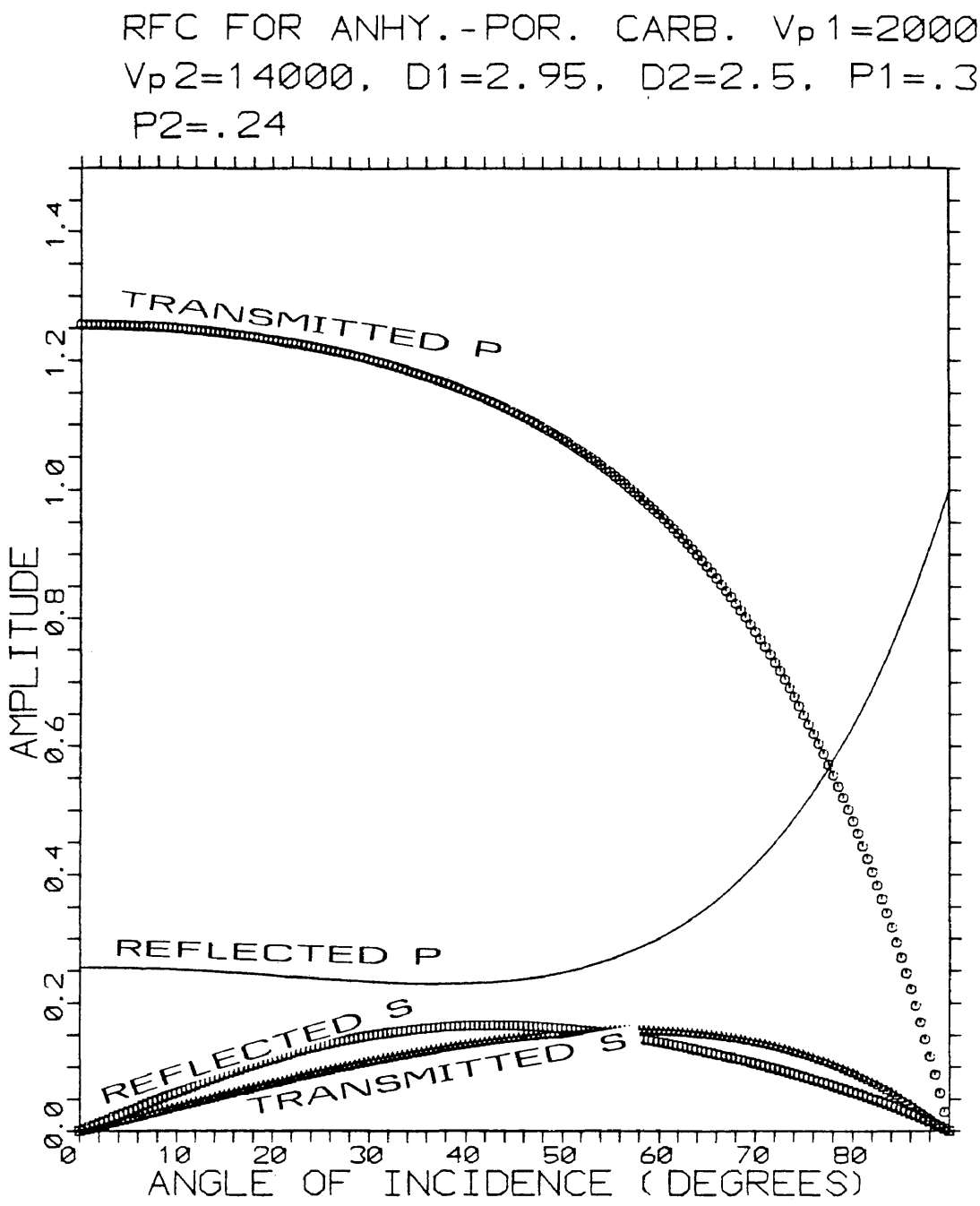

Figure 23. Amplitude versus angle of incidence for an anhydrite-porous carbonate interface. Vp_1 = P-wave velocity for layer 1, D_1 = density for layer 1, P_1 = Poisson's ratio for layer 1.

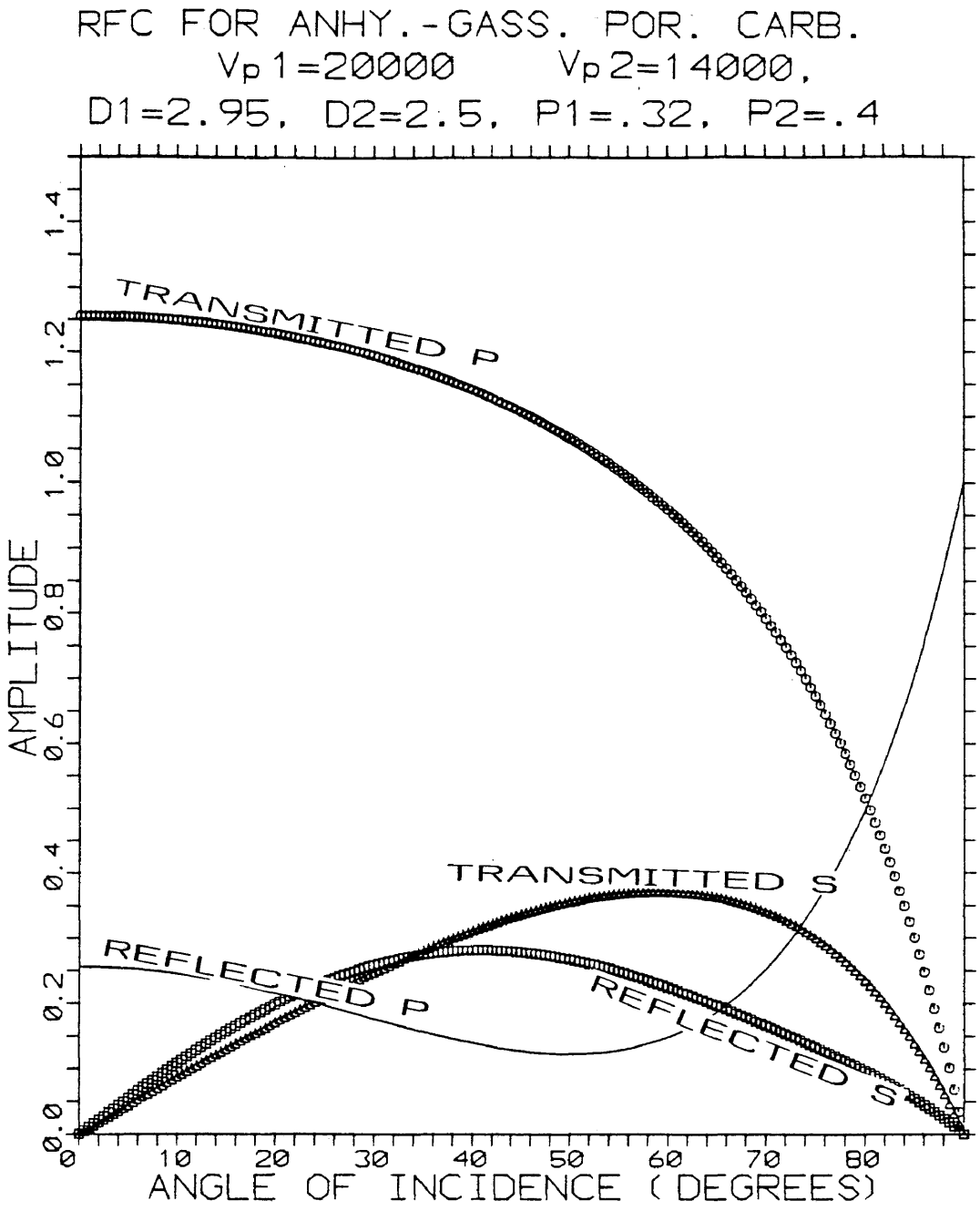

Figure 24. Amplitude versus angle of incidence for an anhydrite-Gassaway porous carbonate interface. Vp_1 = P-wave velocity for layer 1, D_1 = density for layer 1, P_1 = Poisson's ratio for layer 1.

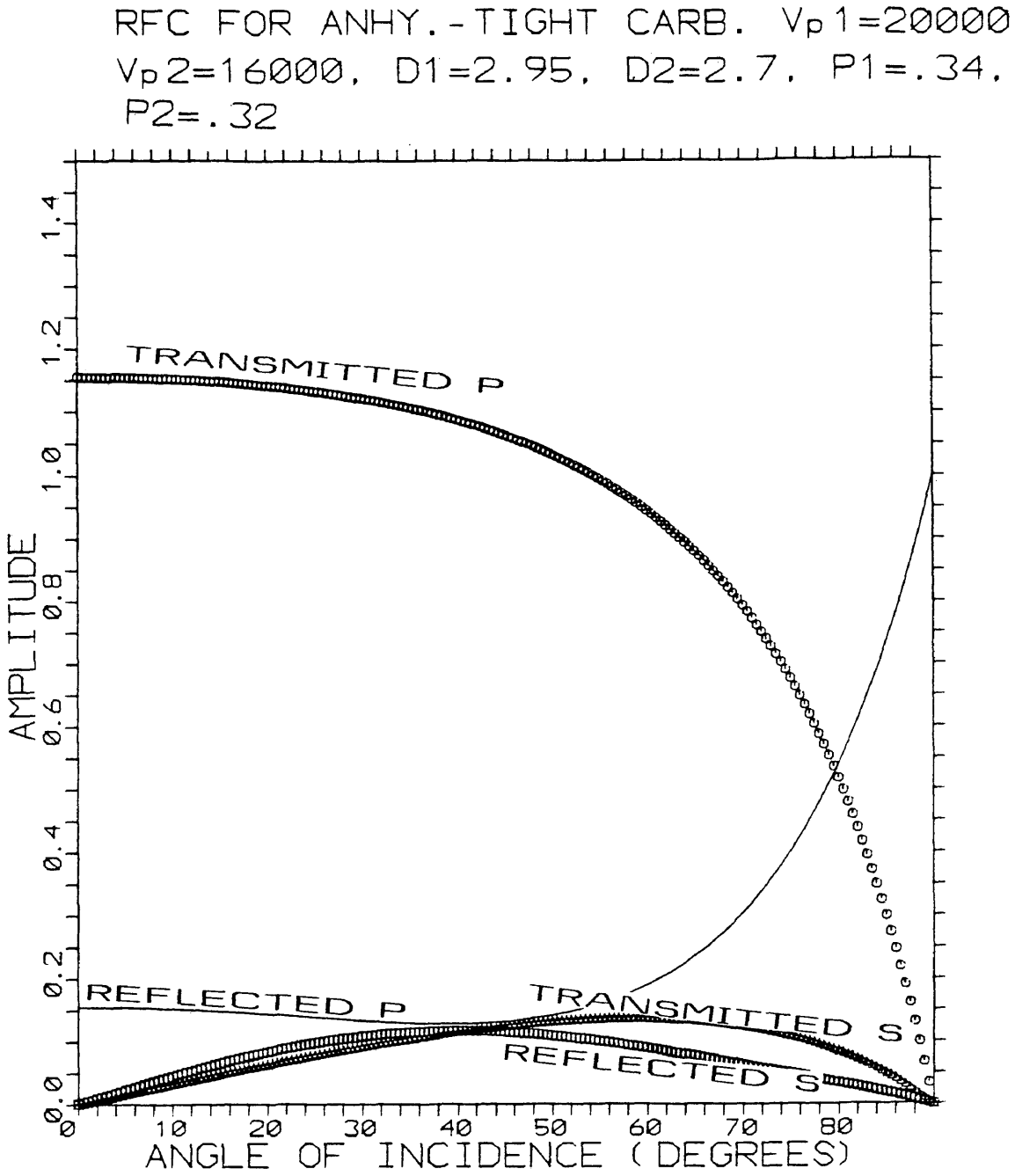

Figure 25. Amplitude versus angle of incidence for an anhydrite-nonporous carbonate interface. Vp_1 = P-wave velocity for layer 1, D_1 = density for layer 1, P_1 = Poisson's ratio for layer 1.

going to come through as reflected wave energy with conventional recording techniques.

AIMS* non-zero offset ray theory

Common source point (CSP) modeling was chosen because it is more economical than common depth point (CDP) modeling. In addition, the model did not involve lateral inhomogeneities, so CSP modeling should give similar results to those that might be obtained with CDP modeling.

Although both ray theory and Kirchhoff wave theory calculations are available in AIMS*, only the ray theory computation will use shear velocity information from user-supplied Poisson's ratios. Therefore ray-theory modeling was used for this thesis. For non-zero offset ray tracing, rays are traced downward from the surface through user-defined horizons and then traced back up again to the surface. These rays are computed according to Snell's Law (Figure 26 and Equation 1).

$$(1) \quad \frac{\sin \theta_i}{a_1} = \frac{\sin \phi_i}{\beta_1} = \frac{\sin \theta_t}{a_2} = \frac{\sin \phi_t}{\beta_2}$$

In AIMS* version 3.0, only P-wave propagation is simulated.

*Trademark of GeoQuest

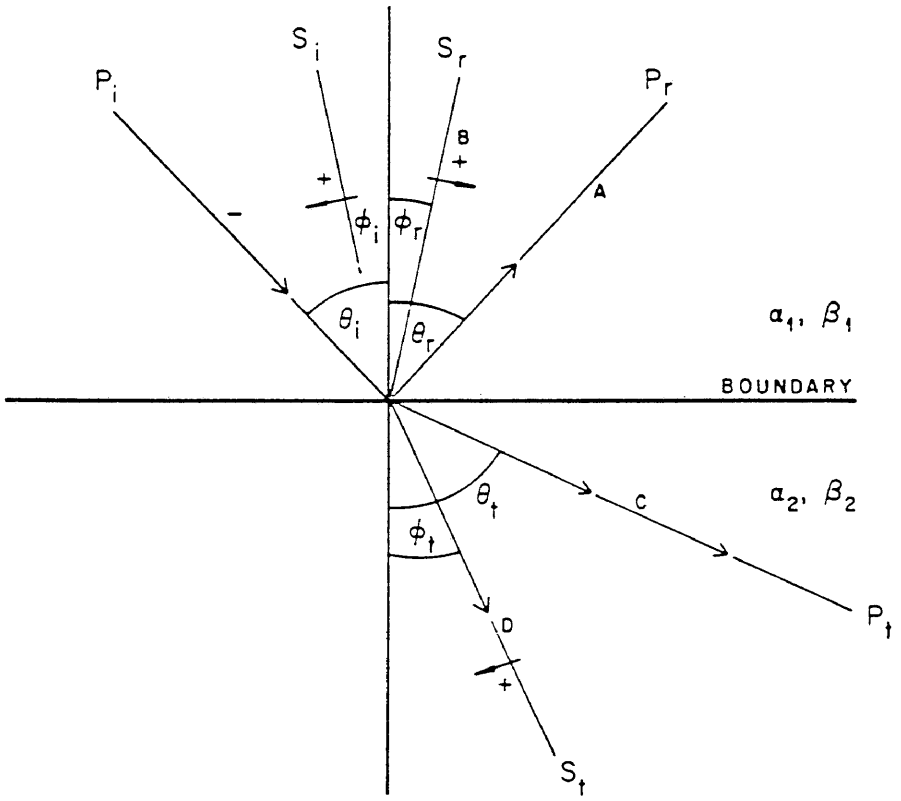

Figure 26. Reflected and transmitted P- and S-waves at a boundary (from Waters, 1981).

However, because a P-wave with non-normal incidence at a plane boundary generates new waves via mode conversions, AIMS* uses the Knott-Zoeppritz energy equations to compute the amplitudes at each interface. The Knott-Zoeppritz energy equations are based on the laws of continuity of normal and tangential displacement and continuity of normal and tangential stress at a boundary (equations 2, 3, 4, and 5 respectively).

(2) continuity of normal displacement

$$\cos \theta_i - A \cos \theta_r + B \sin \phi_r = C \cos \theta_t + D \sin \phi_t$$

(3) continuity of tangential displacement

$$\sin \theta_i + A \sin \theta_r + B \cos \phi_r = C \sin \theta_t - D \cos \phi_t$$

(4) continuity of tangential stress

$$- \sin 2\theta_i + A \sin 2\theta_r + (a_1/\beta_1) B \cos 2\phi_r$$

*Trademark of GeoQuest

$$= - \frac{d_2 \beta_2^2 a_1}{d_1 \beta_1^2 a_2} C \sin 2\theta_t + \frac{d_2 \beta_2 a_1}{d_1 \beta_1^2} D \cos 2\phi_t$$

(5) continuity of normal stress

$$\cos 2\phi_i + A \cos 2\phi_r - (\beta_1/a_1) B \sin 2\phi_r$$

$$= \frac{d_2 a_2}{d_1 a_1} C \cos 2\phi_t + \frac{d_2 \beta_2}{d_1 a_1} D \sin 2\phi_t$$

where A = amplitude of reflected P wave

B = amplitude of refracted P wave

C = amplitude of reflected SV wave

D = amplitude of refracted SV wave

Ideally, modeling would use digitized well logs such as were used in the zero-offset models by Reeve (1986). However, lack of shear log data and lack of access to modeling routines capable of generating non-zero offset models from digitized well logs prohibited such modeling in this study. Therefore, simple plane-layer models were used in this study.

Two models were developed to simulate "off-field" and

"on-field" geology. Off-field geology is represented by a five-layer model shown in Figure 27. On-field geology is represented by the four-layer model shown in Figure 28. The on-field model shows the thinner Frobisher-Alida anhydrite as well as the truncation of younger Mississppian evaporites by the Top of Paleozoic unconformity. CSP records were generated for each of these models, and for models obtained by varying the velocity, density, and Poisson's ratio of the layer representing the Glenburn carbonate. These variations were made to represent a nonporous carbonate and a porous carbonate from core measurements, and a porous carbonate from Gassaway's method of calculation.

The off-field model was constructed as shown in Figure 27. Layer 1 corresponds to the Triassic shalesand redbeds, with P-wave velocity of 13,700 feet/sec, density of 2.5 gm/cc, and Poisson's ratio of 0.38. Layer 2 corresponds to the evaporites in the Mississippian Charles Formation, with V_p of 19,500 feet/sec, density of 2.85 gm/cc, and POI of 0.34. Layer 3 represents the Midale porous carbonate with a V_p of 14,000 feet/sec, density of 2.5 gm/cc and POI of .24. Layer 4 represents the Frobisher-Alida anhydrite with properties the same as Layer 2 were used in modeling. Layer 5 corresponds to the

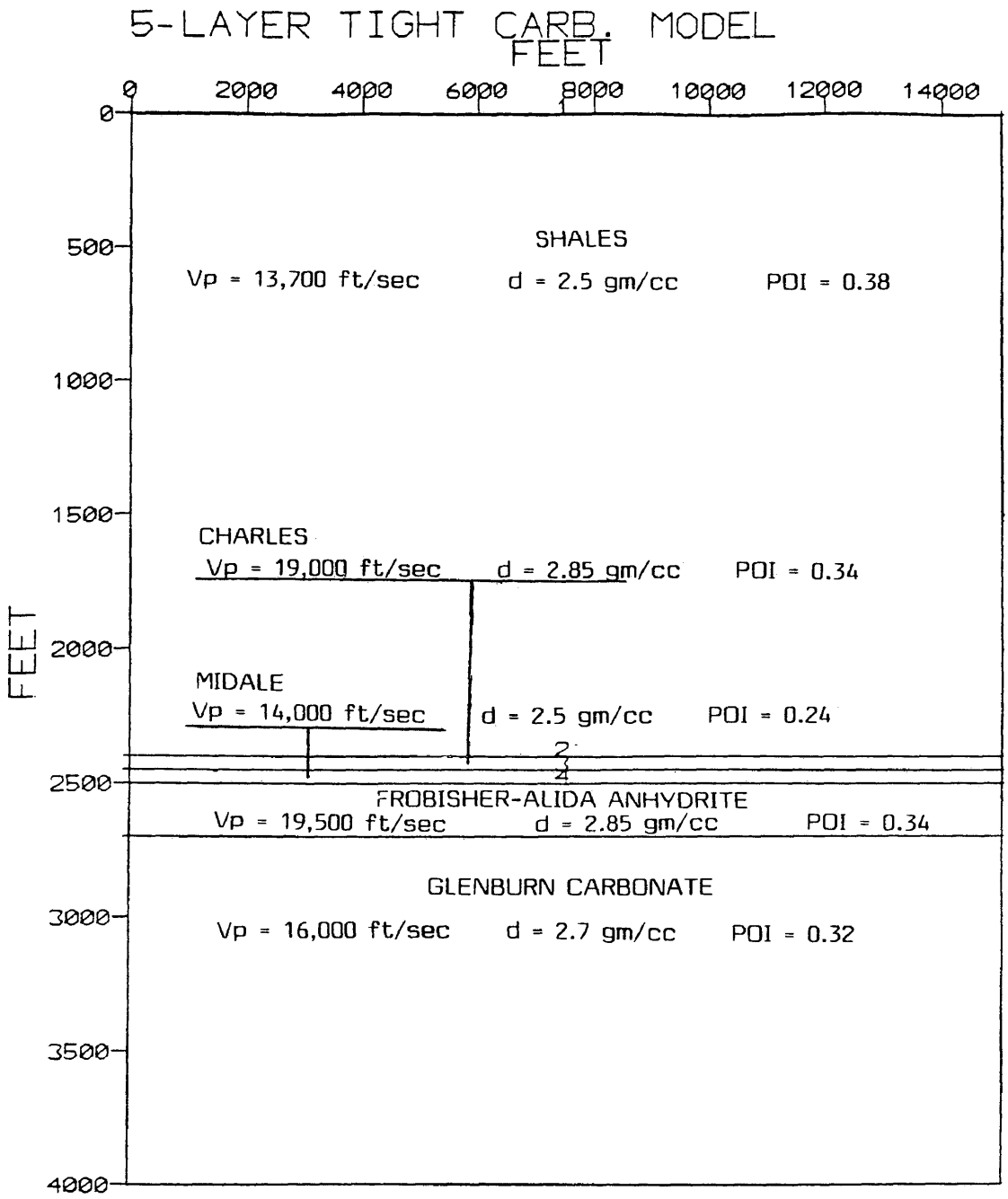

Figure 27. AIMS 5-layer plane layer off-field depth model. Nonporous carbonate model for Glenburn.

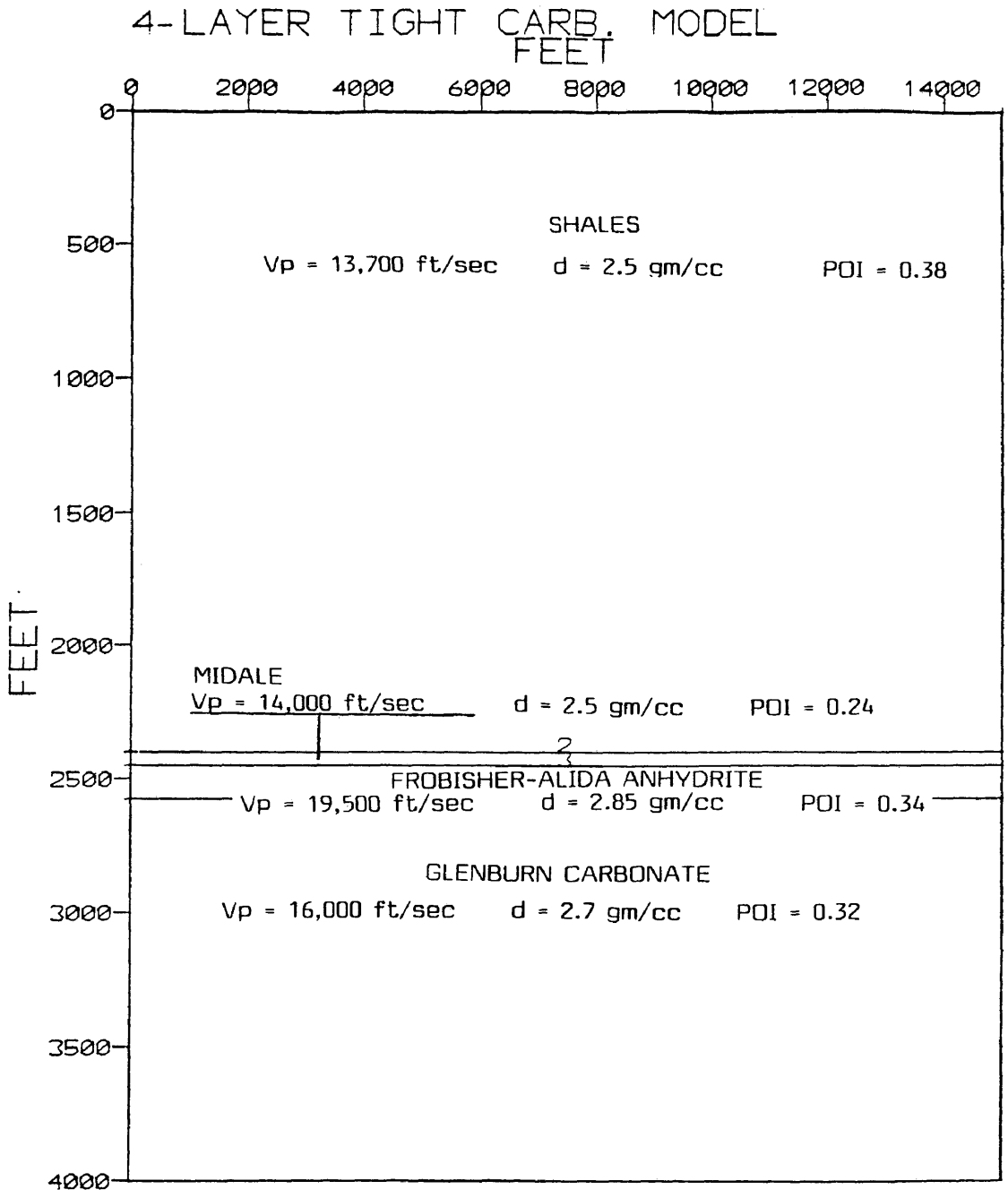

Figure 28. AIMS 4-layer plane layer on-field depth model. Nonporous carbonate model for Glenburn.

Glenburn carbonate. For the porous carbonate model of Figure 28 the properties of Layer 3 were used, while for the non-porous carbonate model, V_p of 16,000 feet/sec, density of 2.7 gm/cc, and POI of .32 were used.

The on-field model is similar to the off-field model with the following exceptions: Layer 2 of the off-field model has been removed, and layer 4 of the off-field model is 100 feet thick rather than 200 feet thick.

Figure 29 shows the CSP model for the 5-layer off-field model with the Glenburn porous carbonate, using core-derived Poisson's ratios for the Glenburn, and generated using a Klauder 12-96 Hz wavelet. The Upper Mississippian evaporites and the Midale carbonate are expressed as a peak and trough respectively at the near offset. The Frobisher-Alida anhydrite is represented by a peak doublet, and the Glenburn porous carbonate is expressed as a poorly developed trough at near offset. The amplitudes of the peak-trough-peak above the Glenburn carbonate trough decrease steadily until an offset of about 4500 feet is reached. At offsets of greater than 4500 feet, the Midale trough disappears and the peak-trough-peak becomes a single high-amplitude peak. At an offset of 4800 feet, the peak appears to begin to change

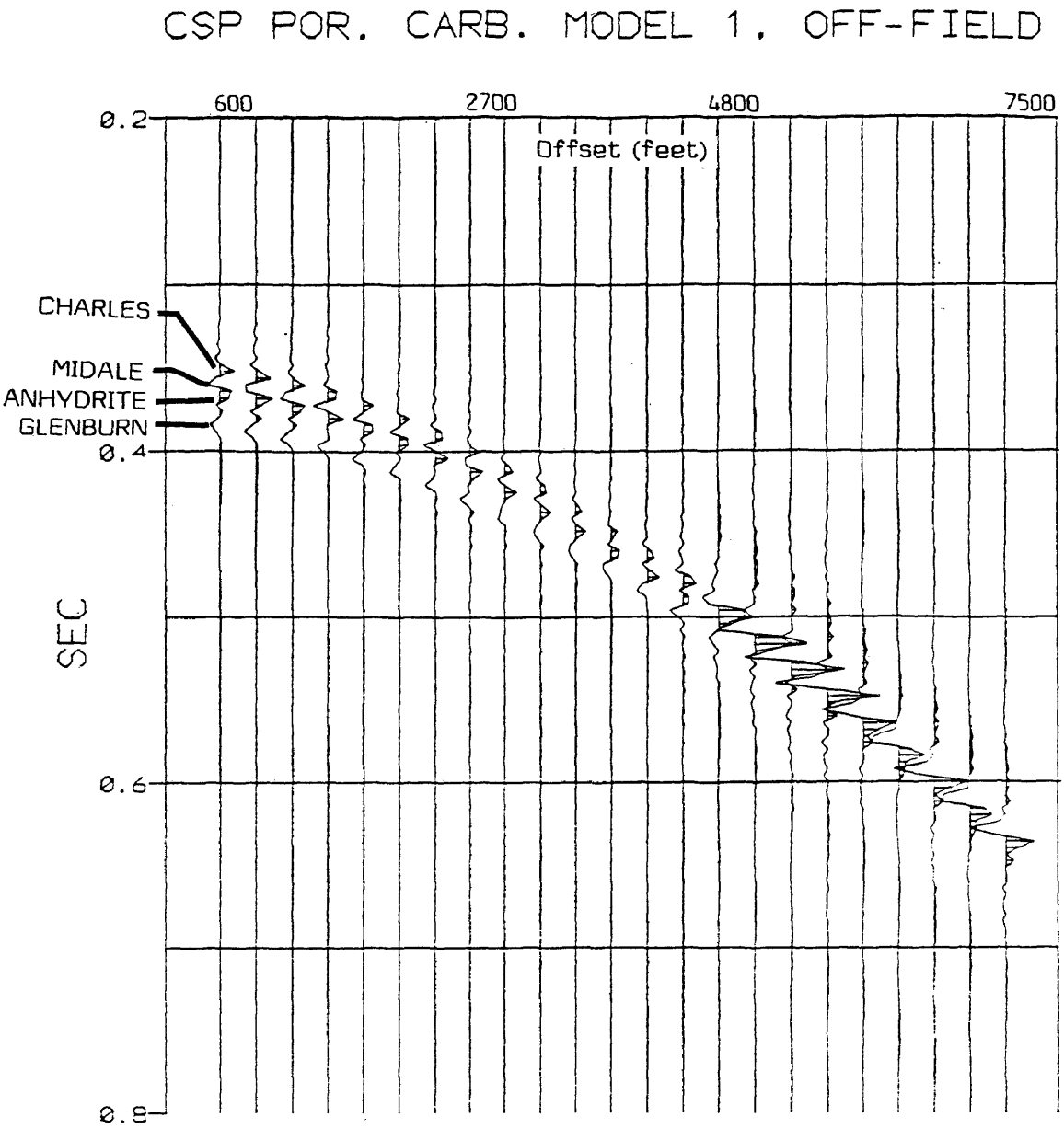

Figure 29. AIMS common shotpoint non-zero offset off-field porous carbonate model.

phase, and the amplitude of the peak increases. The amplitude of the Glenburn trough decreases until an offset of 3600 feet is reached, then the amplitude increases slightly. At 5100 foot offset, the Glenburn trough is obscured by the phase change of the events above it. Figures 30 through 34 show the AIMS* CSP response to the remaining models described above. The models shown in Figures 29 through 32 used core-derived Poisson's ratios for the Glenburn, while the models in Figures 33 and 34 used Poisson's ratios obtained by using Gassaway's method. The 4-layer models do not appear to match Reeve's zero-offset models very well, probably because the AIMS* 4-layer models lack a thin layer of Charles evaporite that is shown on the well-log model. In general, the CSP models do not show a very different response between the porous and nonporous carbonate models.

Upon comparison of the curve output by Xiaochun's Zoeppritz equation program (Figure 22) with the AIMS* CSP model (Figure 29), the large amplitude increase of the peak above the Frobisher -Alida carbonate may correspond to the large amplitude increase indicated for the shale-anhydrite interface as the critical angle is approached. The curve generated by Xiaochun's program does not, however, indicate a phase change.

*Trademark of GeoQuest

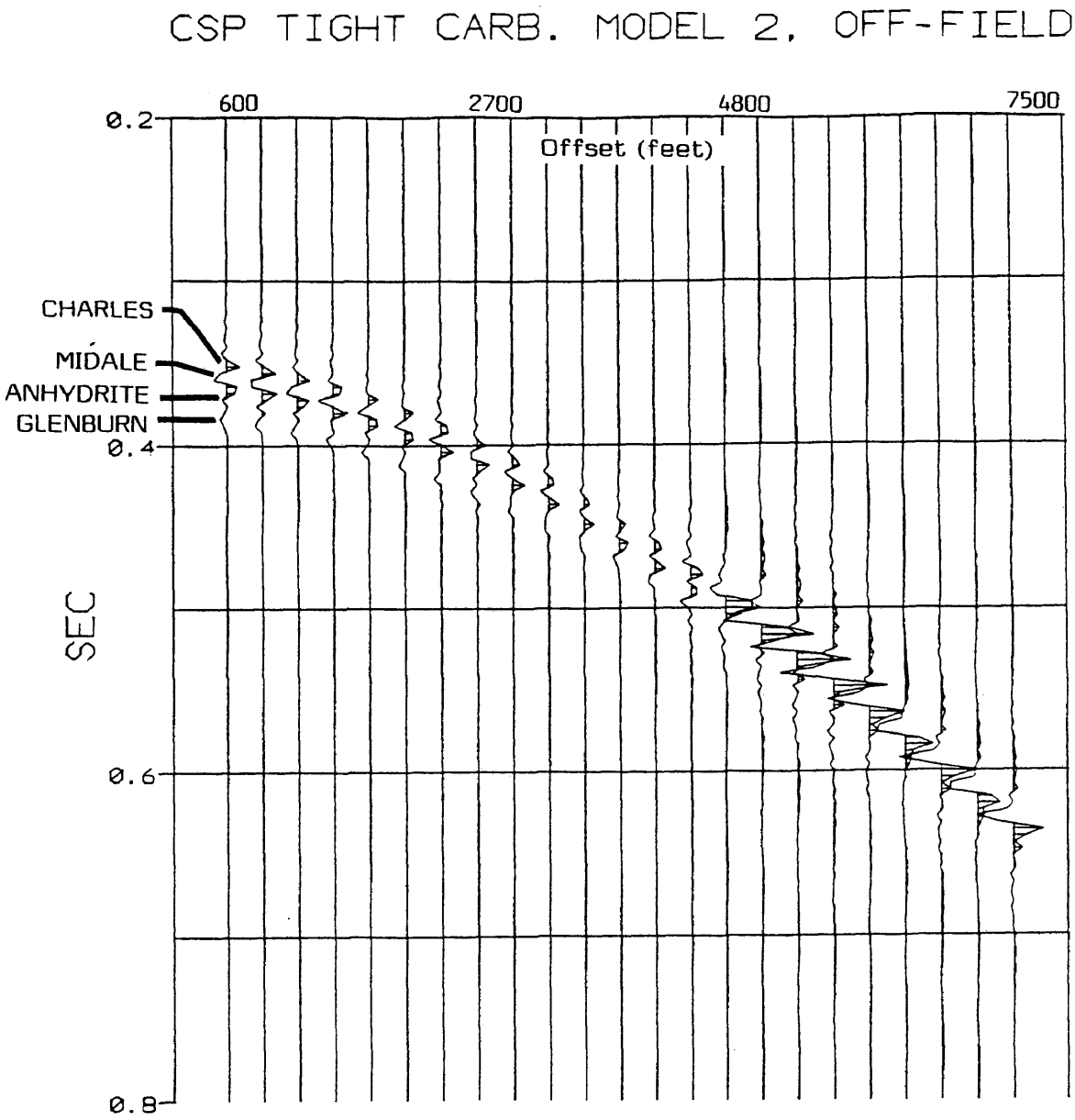

Figure 30. AIMS common shotpoint non-zero offset off-field nonporous carbonate model.

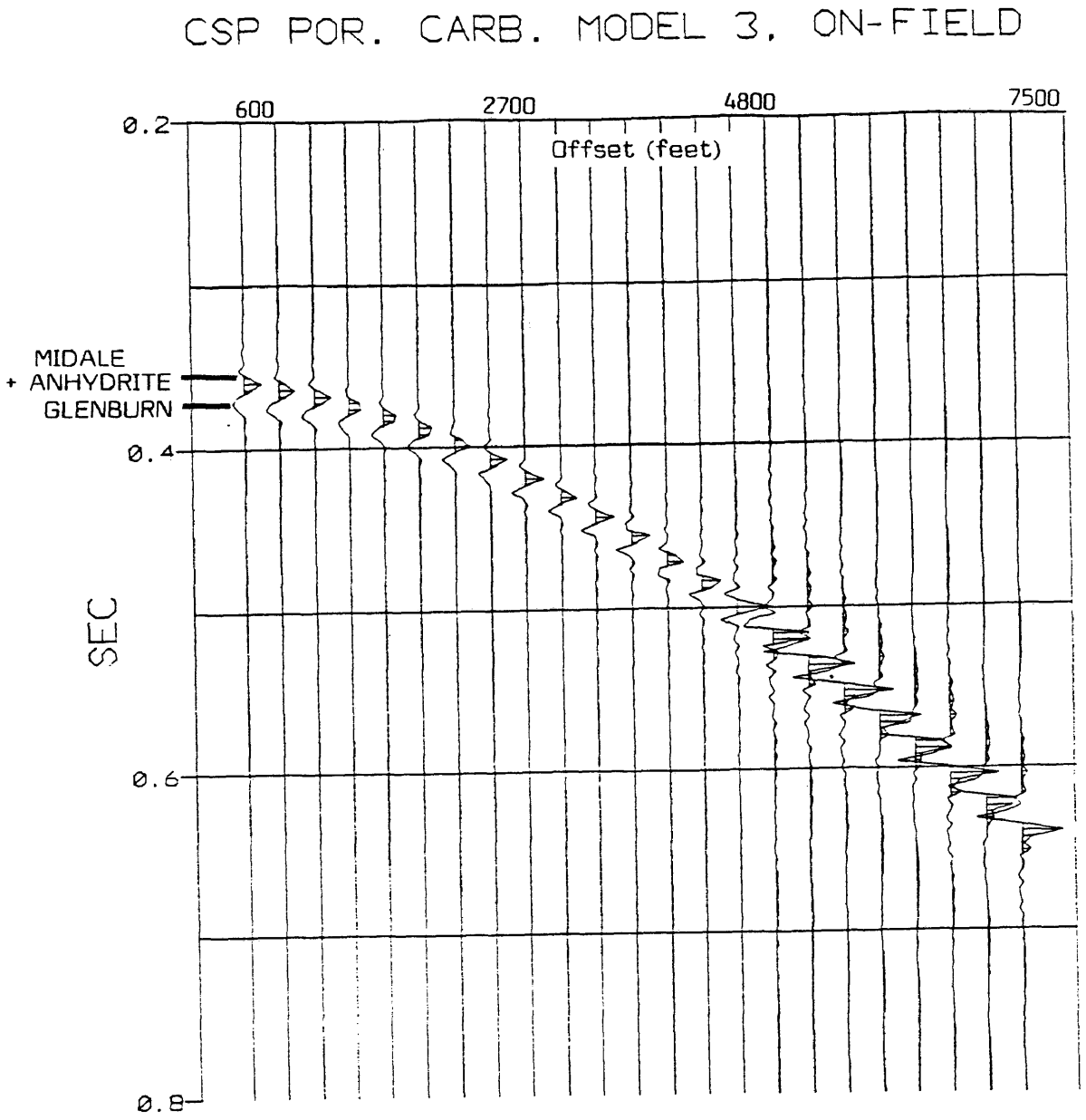

Figure 31. AIMS common shotpoint non-zero offset on-field porous carbonate model.

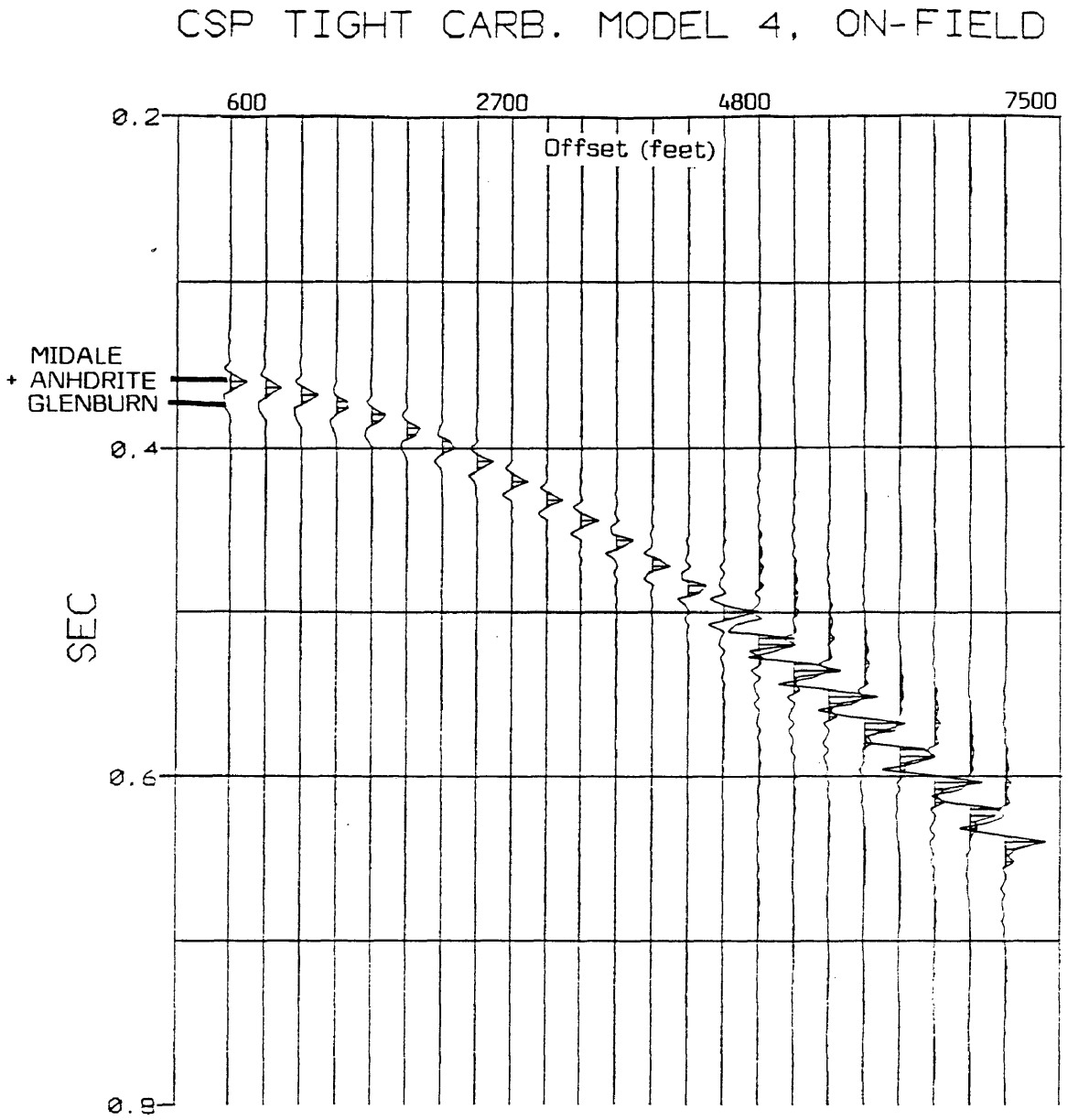

Figure 32. AIMS common shotpoint non-zero offset on-field nonporous carbonate model.

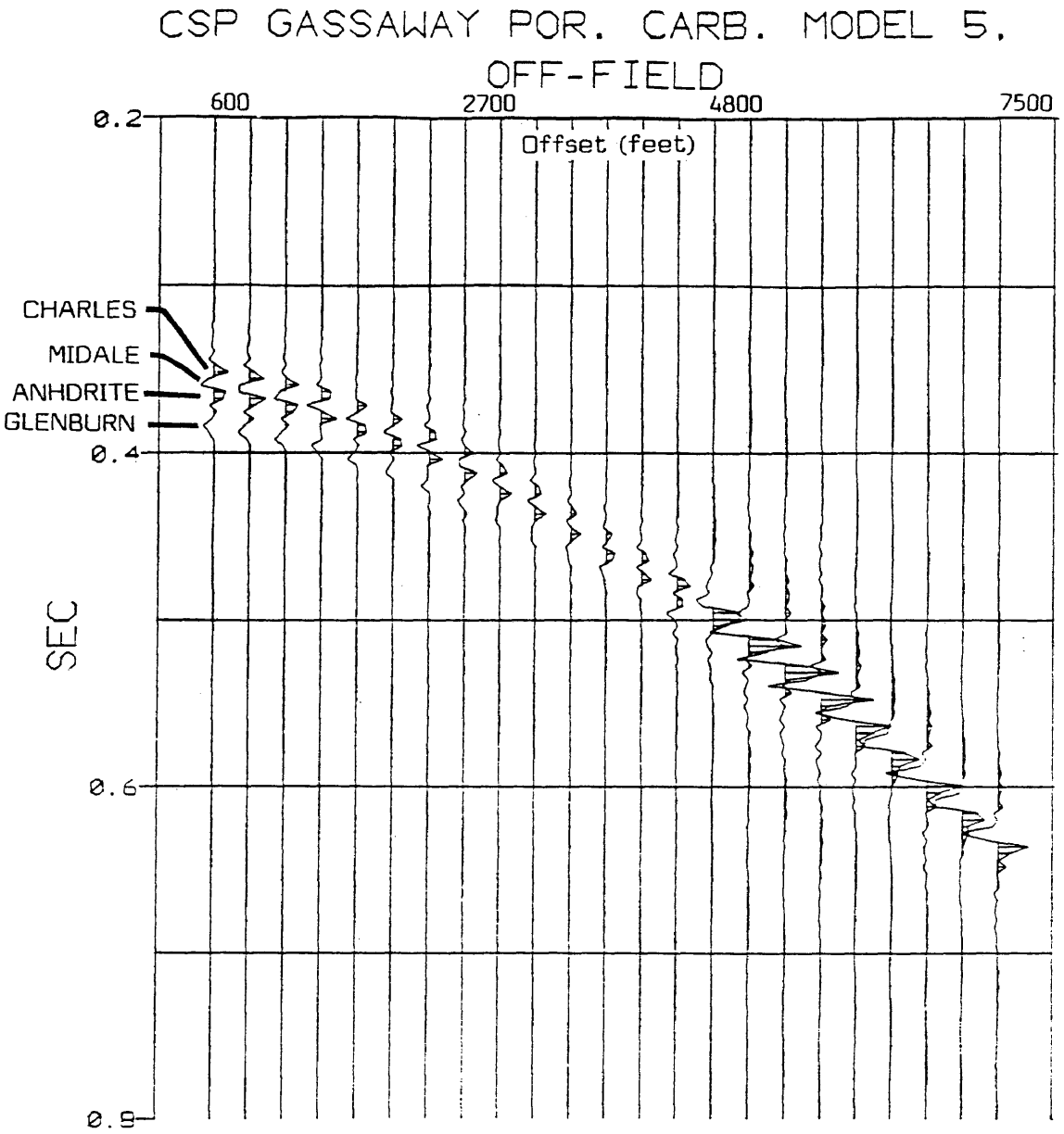

Figure 33. AIMS common shotpoint non-zero offset off-field Gassaway porous carbonate model.

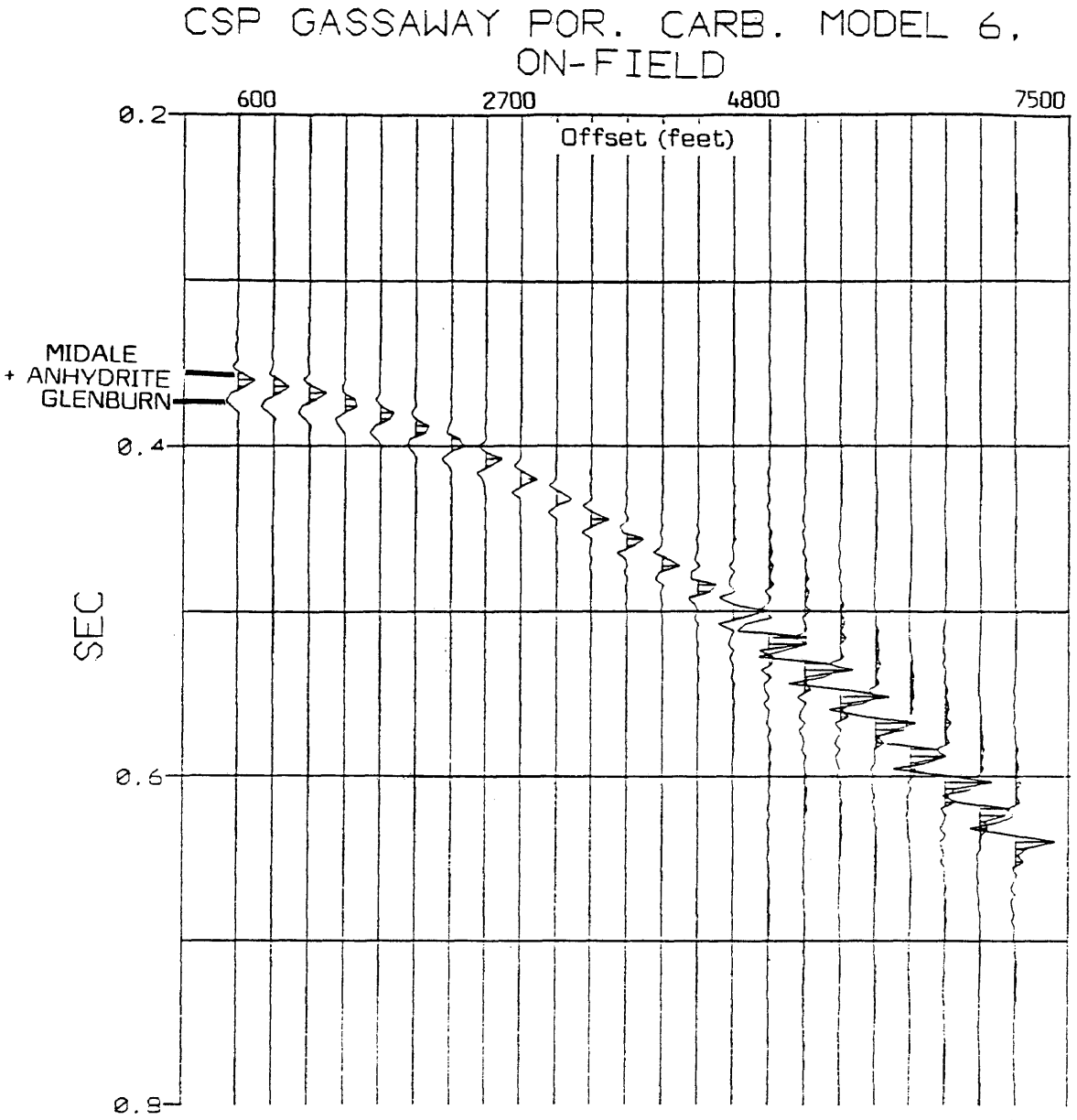

Figure 34. AIMS common shotpoint non-zero offset on-field Gassaway porous carbonate model.

A comparison of the zero-offset seismic model produced by Evergreen software with the zero-offset response from AIMS* leads to the following observations:

(1) Reeve's zero-offset normal polarity 10-85 Hz seismic model (Figure 12) shows a broad peak for the Frobisher-Alida anhydrite which becomes an asymmetric peak doublet where the anhydrite is thicker and the Glenburn porosity is absent. The Frobisher-Alida trough is a trough doublet with a poorly developed peak in between and changes to a strong trough with a small peak above it where the Glenburn porosity is absent. The trough is higher amplitude where porosity is absent and lower amplitude where porosity is present; the amplitude difference may be due to a thinner anhydrite coupled with a more gradational impedance boundary where the Glenburn carbonate is porous.

(2) The AIMS* 5-layer model, which should correspond to the right side of Figure 12 where the anhydrite is thicker and porosity is present, shows a top-loaded peak doublet for the Frobisher-Alida anhydrite and a poorly developed trough singlet for the Glenburn carbonate. When properties for a nonporous carbonate are used for Layer 5 (Figure 30), the trough has a lower amplitude than when

*Trademark of GeoQuest

the properties for a porous carbonate are used. This is to be expected, because there is more of an impedance contrast between the porous carbonate layer and the anhydrite layer than there is between the nonporous carbonate layer and the anhydrite layer. However, this does not match with Reeve's model, probably because the anhydrite-carbonate boundary is, in reality, more gradational.

(3) The 4-layer AIMS* model, which should correspond to the left-hand side of Figure 12, shows a single peak for the Midale carbonate and the Frobisher-Alida anhydrite, and a trough singlet for the Frobisher-Alida carbonate. This model does not match Reeve's model very well, again because it does not allow for gradational contacts and thin-layer seismic response.

(4) The CSP models generated using the Poisson's ratios calculated from Gassaway's method do not appear to be dramatically different from those generated using laboratory-determined Poisson's ratios.

AIMS* offers the option of outputting reflection coefficients for each trace for each horizon. Figures 35, 36, and 37 show the graph of the absolute value of the reflection coefficient and the ratio of the reflection coefficient to the near offset reflection coefficient

*Trademark of GeoQuest

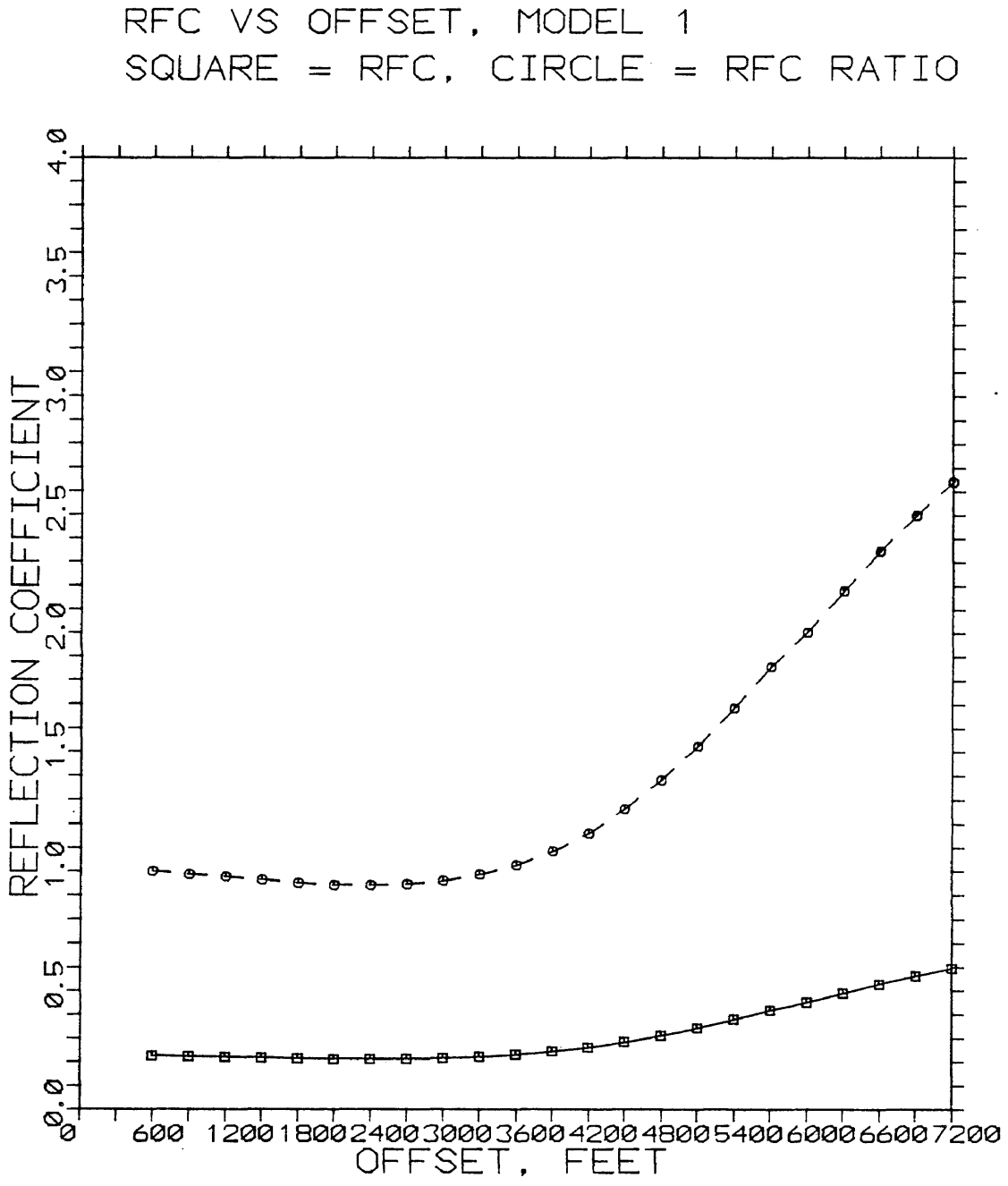

Figure 35. Reflection coefficient versus offset output by AIMS for the porous Glenburn carbonate horizon.

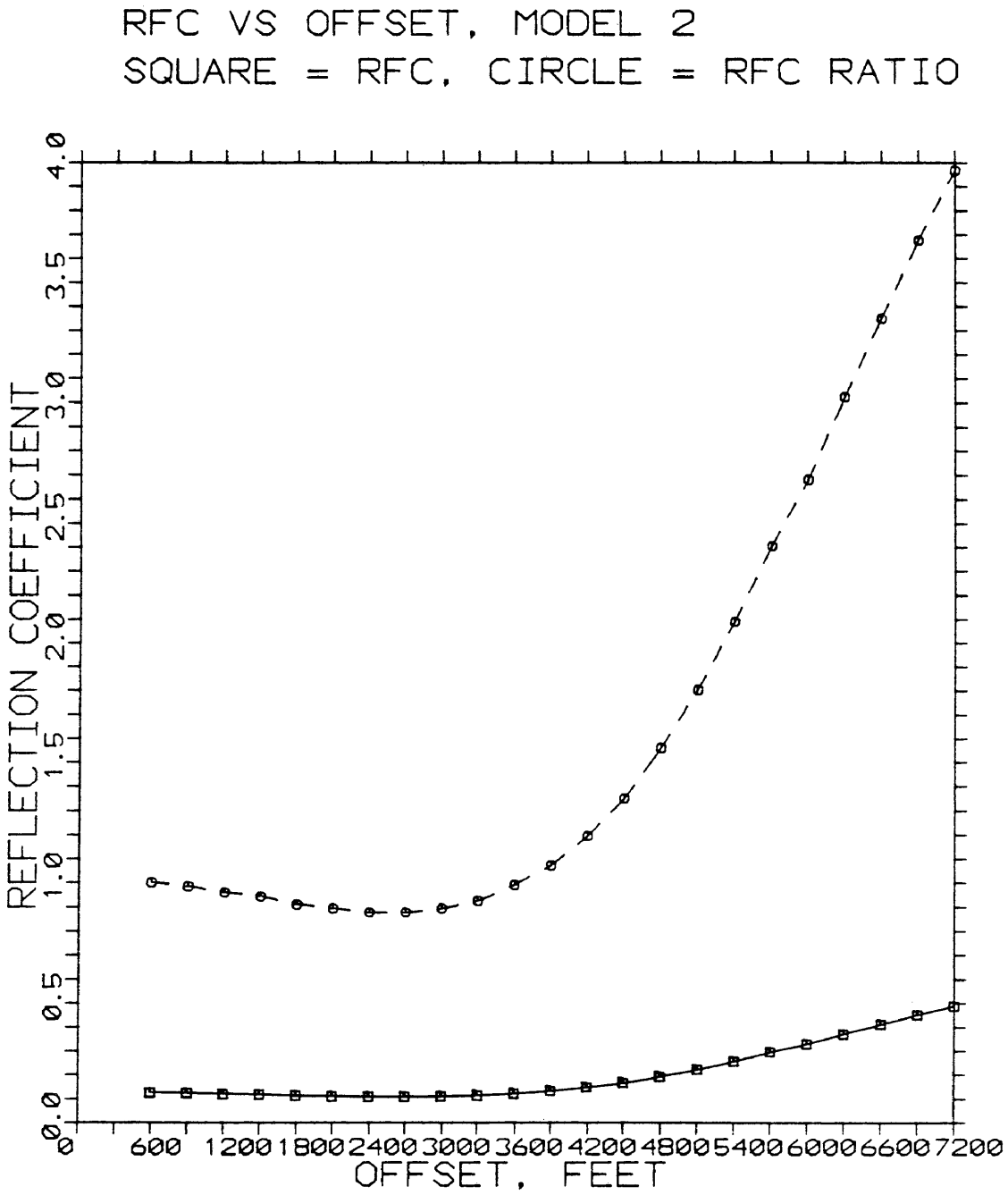

Figure 36. Reflection coefficient versus offset output by AIMS for the nonpor. carbonate horizon.

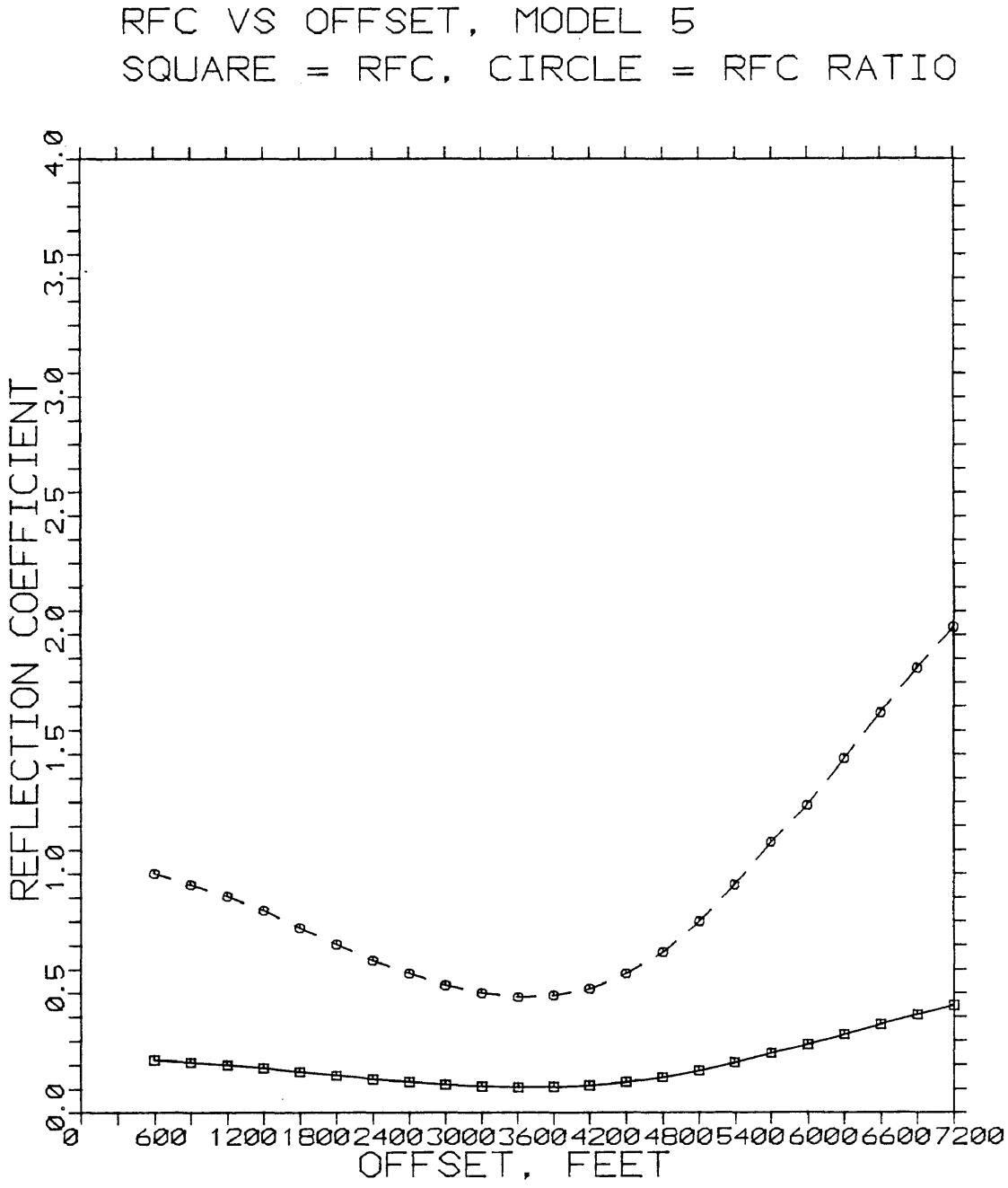

Figure 37. Reflection coefficient versus offset output by AIMS for the porous Gassaway carbonate horizon.

versus offset in feet for models 1, 2, and 5, respectively. Similar graphs were not produced for the other models because they would be redundant.

The graphs for the off-field porous carbonate and non-porous carbonate models (Figure 35 and 36) show very little difference between the reflection coefficient ratio curves out to an offset of about 4500 feet. At offsets greater than that, the reflection coefficient ratio increases faster with increasing offset for the non-porous carbonate model than for the porous carbonate model. However, the CSP model shows that, for offsets greater than 4500 feet, the high amplitude peak for the horizons above the Frobisher-Alida carbonate is undergoing a phase change and obscuring the carbonate trough. If this effect occurs on the real data, then it would be difficult to compare the amplitude of the real data to the reflection coefficients of the model. This is because reflection coefficients are not what is actually extracted from the real data.

The curve of reflection coefficient ratio versus offset for the Gassaway porous carbonate model (Figure 37) shows a 50% decrease in the ratio between 600 and 3600 feet of offset. Beyond 3600 feet, the ratio increases

again out to 7200 feet of offset. However, most of the relavent literature and laboratory studies cited previously in this study indicate that a Poisson's ratio of 0.34 is too high for a porous carbonate, so this model may be unrealistic.

The general shape of the reflection coefficient curves from AIMS* seem to agree with those generated by Xiaochun's program, although the shape of the AIMS* curves suggest that the range of angles of incidence is larger than was expected for the far offset and depth of the target given in the model.

Although simple modeling has not indicated distinct amplitude-offset trends, it may be that the model being used is too simple. Detailed shear-wave or Poisson's ratio information from well logs is not available for this study, so it is not possible to construct a more realistic model. If it were possible to use log information for non-zero offset modeling, more definitive results might be obtained. The difference in character between the zero-offset synthetic seismic section generated using sonic and density logs, and the near-offset traces of the CSP models which used simple plane-layer models illustrates the importance of using well log data in modeling.

*Trademark of GeoQuest

SEISMIC DATA

Comparison of Reeve's 5-10-85-95 Hz normal polarity seismic model (Figure 12) with the normal polarity true-amplitude processed seismic section (Plate 1) shows good agreement between the data and the model. Plate 2 is the synthetic seismogram used to verify the horizon correlations and phase of the data. A comparison of the synthetic with the data did not indicate an obvious phase shift, so it was assumed that the data were near zero-phase.

The portion of the model that shows the on-field seismic response (left side of Figure 12) shows a broad peak for the Charles evaporites and a trough doublet with a poorly developed peak in between for the Frobisher-Alida interval; the Glenburn porous carbonate is expressed as the lower trough of the doublet. Projections of the producing wells at the Wiley Field onto the seismic line are shown in Figure 38. Figure 39 shows the relationship between the well locations and the seismic line. Shotpoints and well identifications could not be shown due to the proprietary nature of the data. The Frobisher-Alida interval is expressed on the seismic data (Figure 39) as a broad trough with a poorly developed peak. The

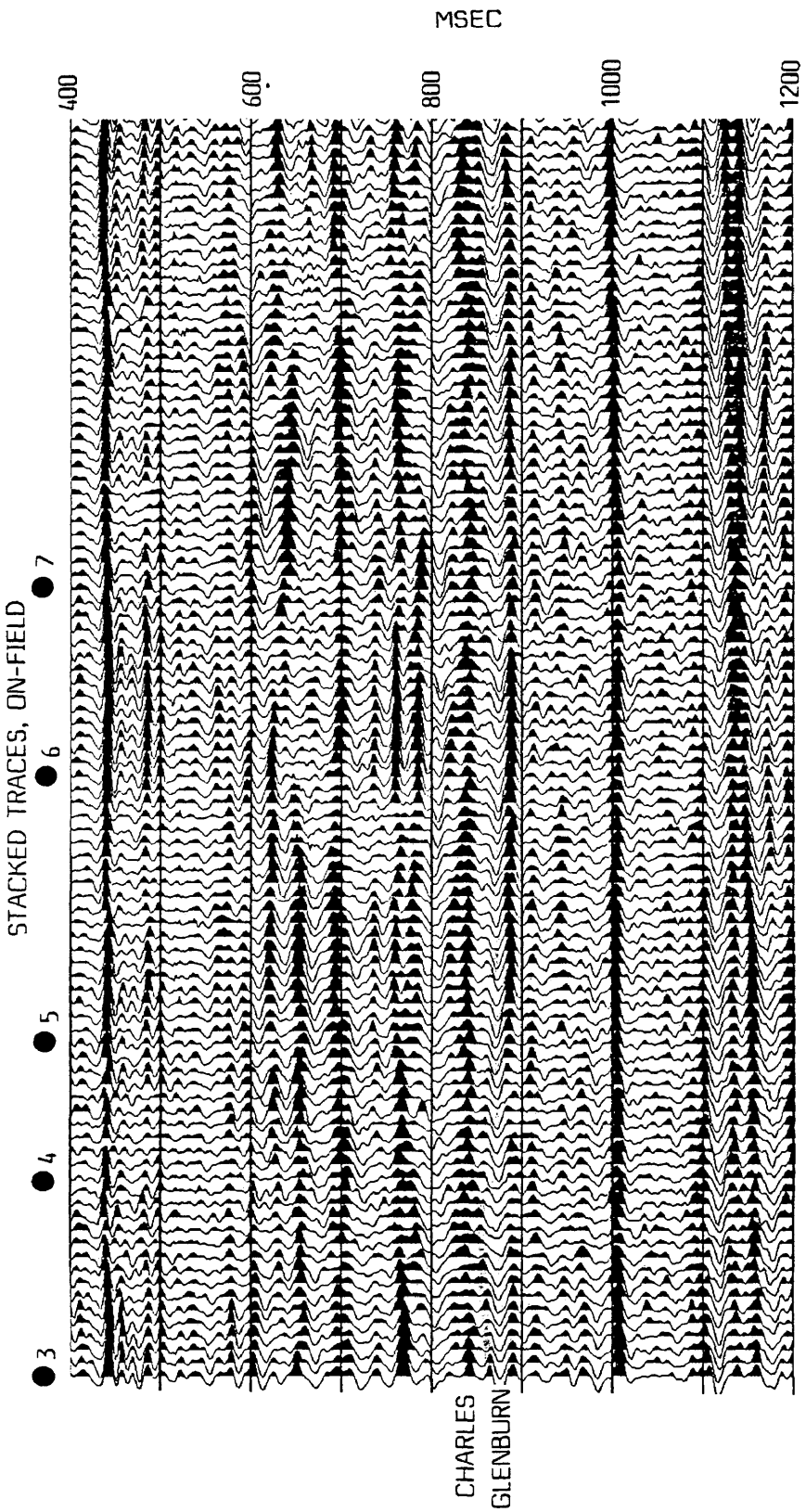

Figure 38. Portion of the stacked section that corresponds to producing wells in the Wiley Field.

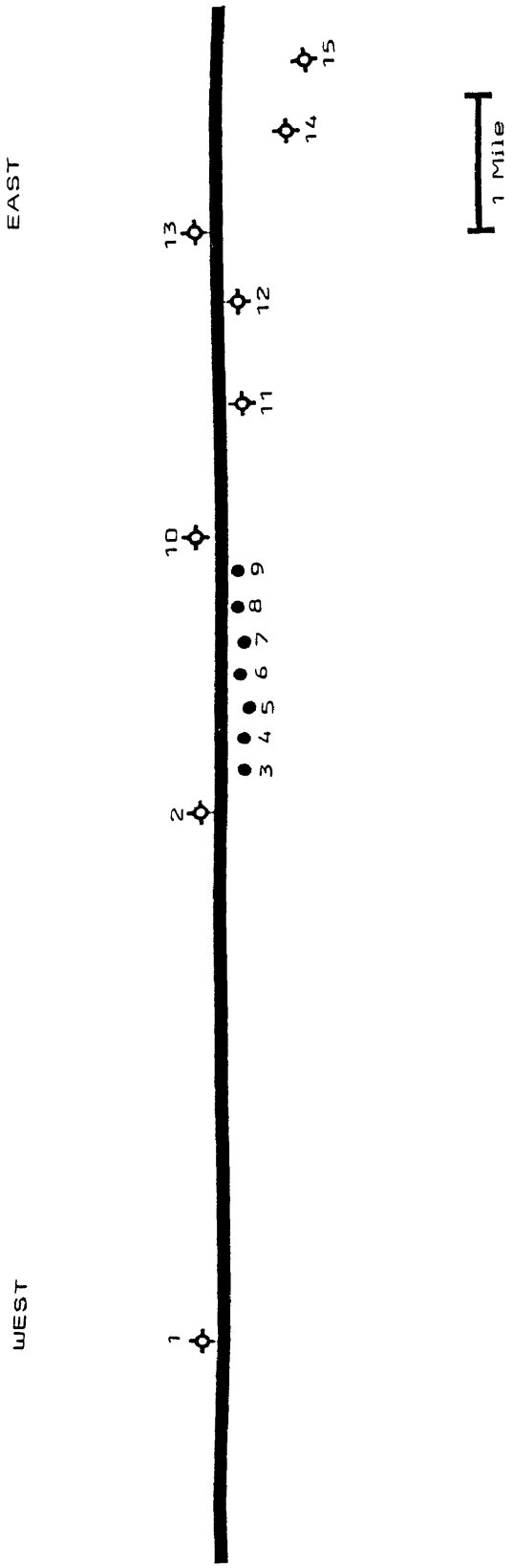

Figure 39. Map showing well positions with respect to the seismic line (to scale).

Charles is expressed as a broad peak or peak doublet above the broad trough. The appearance of an extra peak (red) above the Glenburn (blue) at the projection of well 3 may be due to that well's location at the periphery of the Wiley Field. The change in the character of the Glenburn trough from a broad trough to a sharp trough, to the right of well 7 is most likely due to the Top-of-Paleozoic unconformity over the eastern portion of the field. Reeve (1986) showed that the unconformity could mask the broad trough character of the Glenburn if it cut low enough into the Mississippian section above the Glenburn. Examination of CDP gathers for that portion of the seismic section showed the velocities and statics to be accurate.

The off-field portion of the seismic model (right side of Figure 12) shows the Charles expressed as a sharp peak, while the thicker Frobisher-Alida anhydrite is expressed as an extra smaller peak between the Charles peak and the Glenburn trough. The non-porous Glenburn carbonate shows up as a sharp trough singlet of higher amplitude than the porous Glenburn carbonate in the on-field portion of the seismic model.

The data show a very similar character to the model in most of the off-field portion of the line (Figure 40).

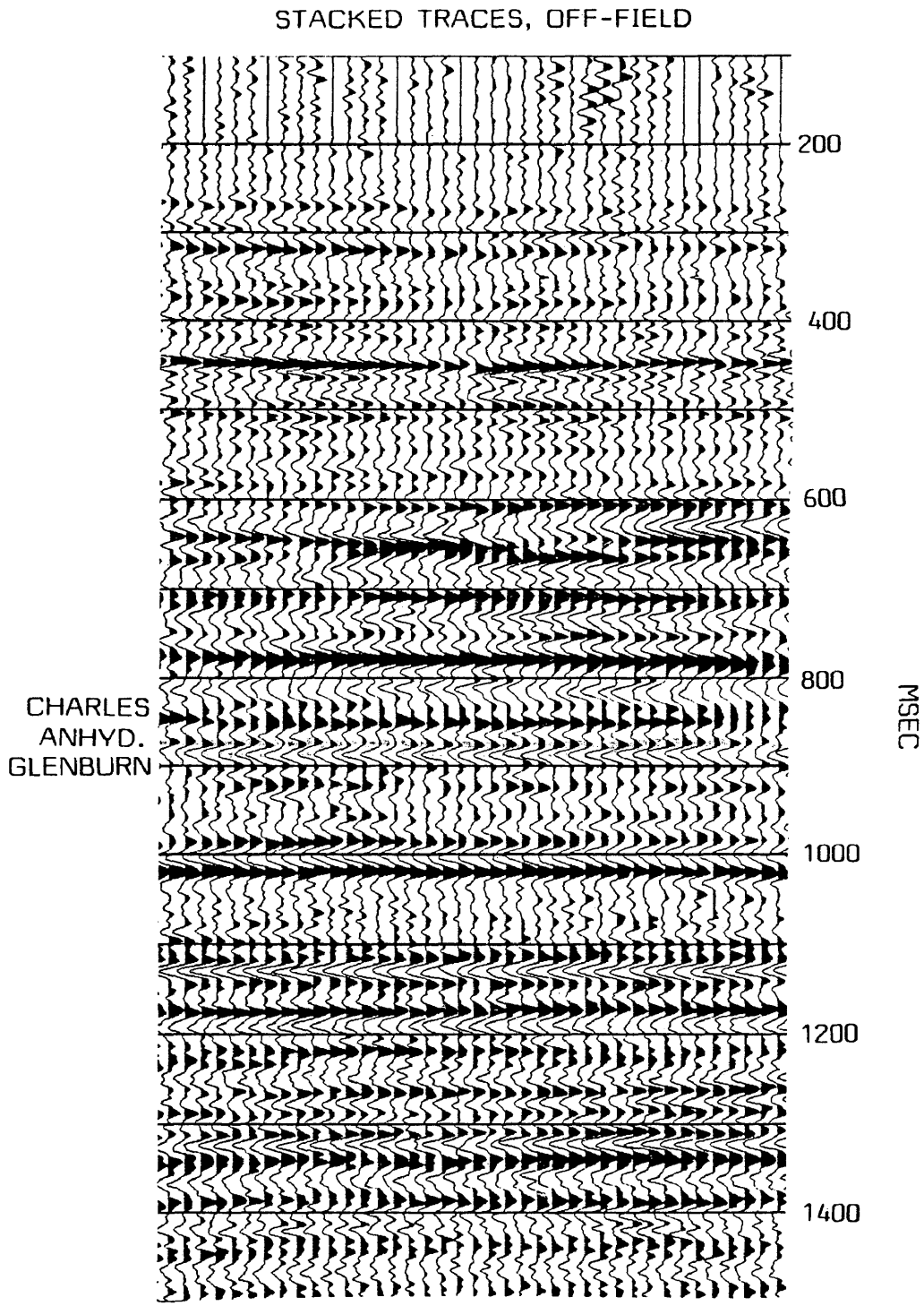

Figure 40. Portion of the seismic section that shows off-field seismic character.

At least two areas where the data do not show this character off-field may be attributable to poor velocity picking because of multiples and/or inadequate statics corrections. Analysis of the summed CDP gathers (Figure 41) for the stacked traces shown in Figure 42 indicate that the data show a poor match to the off-field model primarily because of poor statics correction rather than poor velocity picking or geologic changes. The poor match of the stacked traces in Figure 43 to the model appears to be mostly due to velocities that were picked too low (Figure 44).

Zones of porous Glenburn carbonate have been interpreted by Gerhard (1985) to have formed by subaerial diagenesis on paleohighs related to Devonian Prairie Salt solution. The stacked seismic section (Plate 1) does not show evidence that two areas referenced in the preceding paragraph are located above such paleohighs, whereas it can be seen on the section that the Wiley Field is located above a high at the level of the Prairie evaporite/Winnepegosis.

Further examination of the CDP gathers illustrates the necessity of examining the pre-stack data throughout the processing procedure and even during interpretation of the stacked section. The final velocity analysis shown in

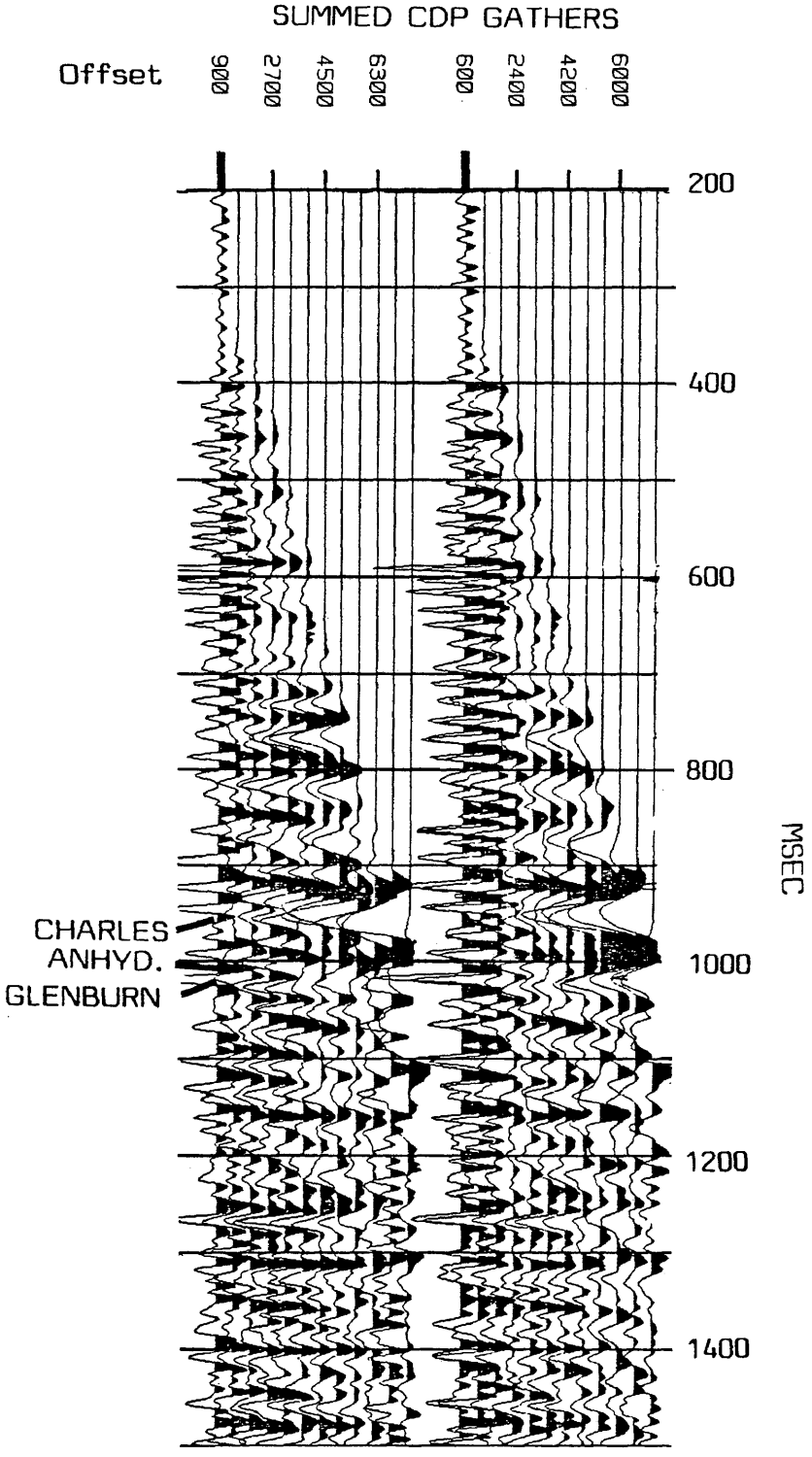

Figure 41. Summed CDP gathers with statics problem.

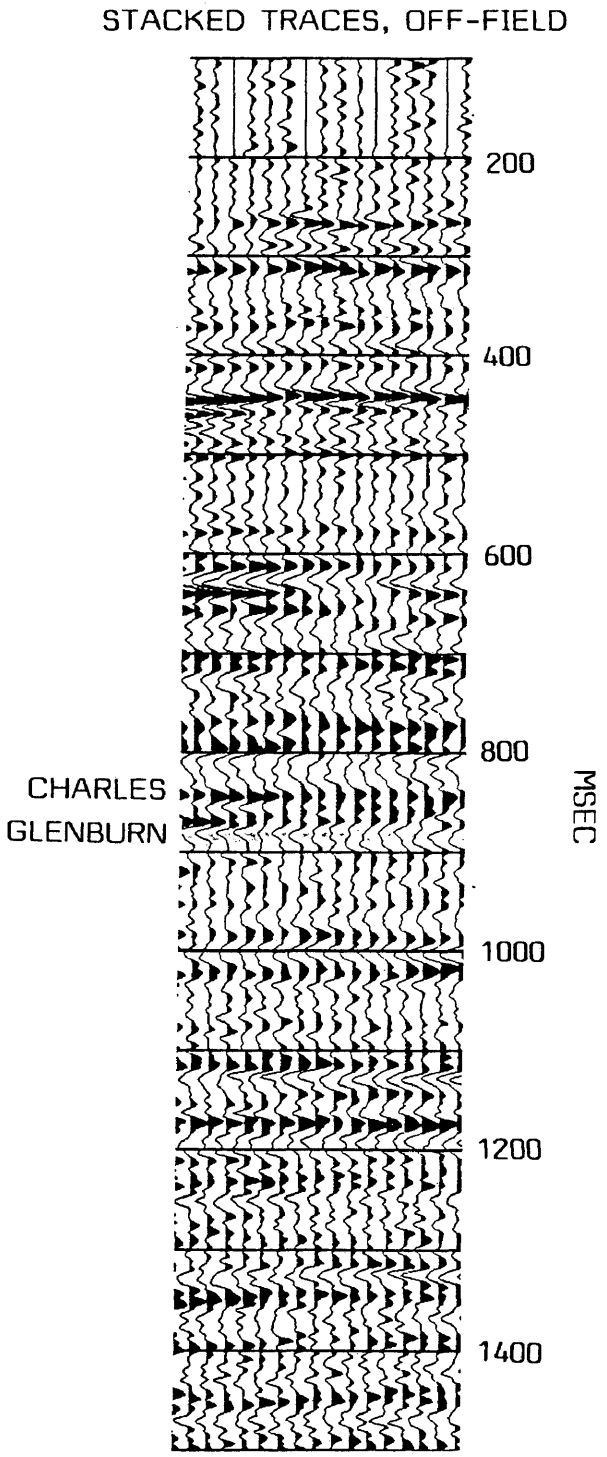

Figure 42. Off-field stacked traces that appear to show on-field seismic character, due to poor statics correction.

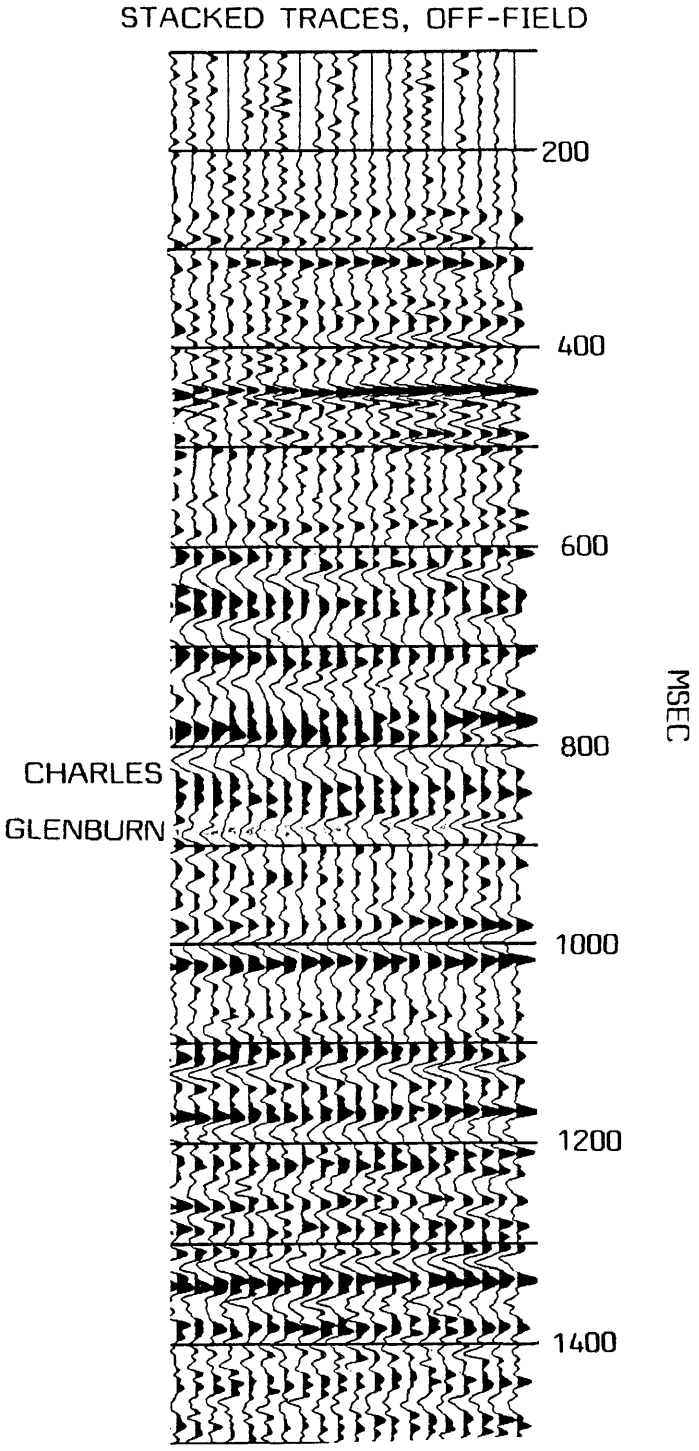

Figure 43. Off-field stacked traces that appear to show on-field seismic character, due to poor NMO before stack.

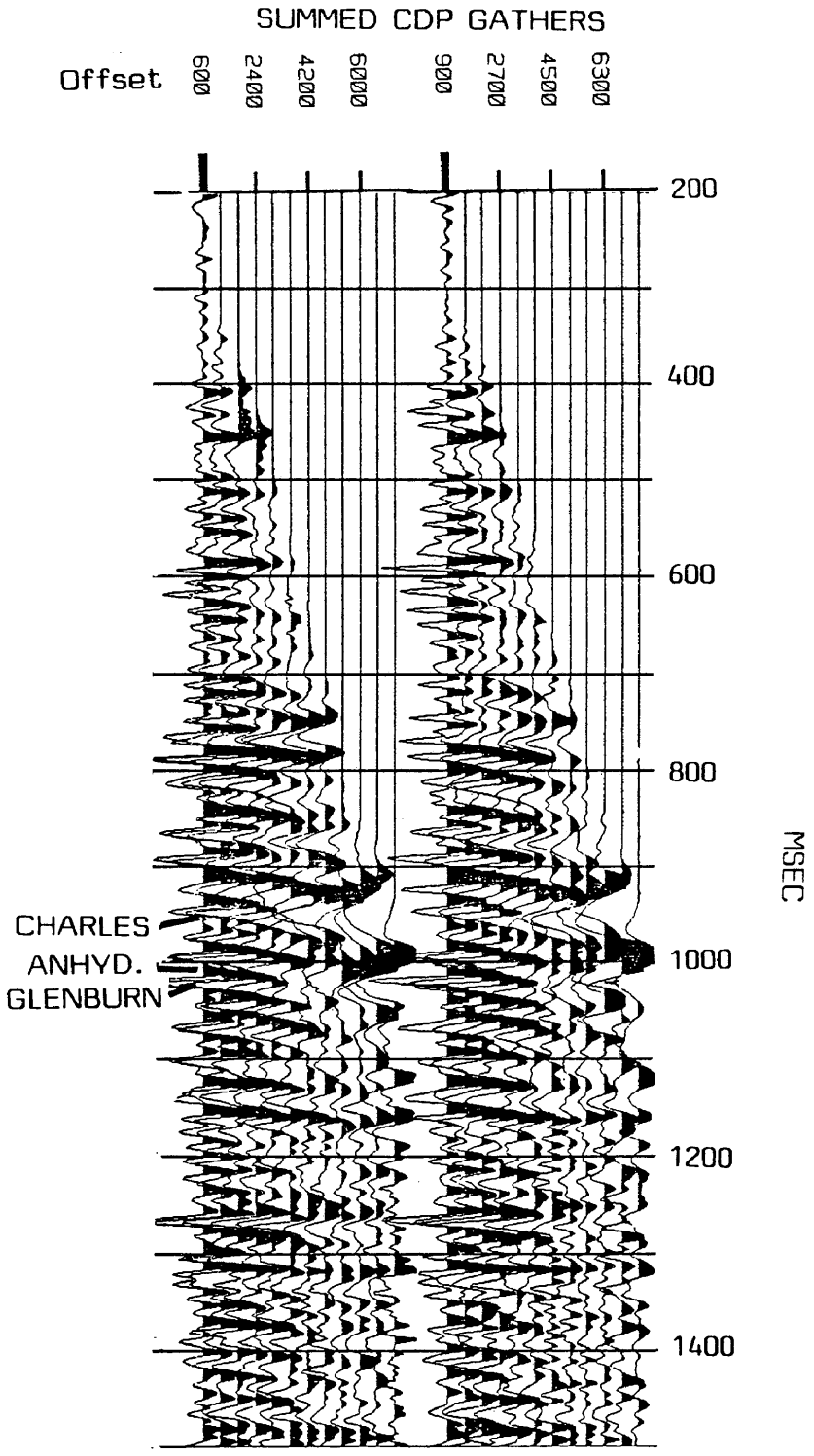

Figure 44. Summed CDP gathers showing low NMO velocities.

Table 2 was deemed necessary when the stacking velocities obtained from previous analyses were applied to the CDP gathers. When the gathers were displayed, it was apparent that the velocities were too high. Therefore, velocities were picked by hand from the CDP gathers displayed by the final velocity analysis. Multiples, especially from 800 to 1200 ms, further complicated the velocity analyses, and resulted in velocities that were too slow over some portions of the seismic line that had interpolated velocities between the control points.

Figure 45 shows two representative summed CDP gathers from the on-field portion of the seismic line. The Glenburn trough shows a decrease in amplitude with increasing offset out to about 4200 feet. The amplitude of the trough then increases out to the far offset. However, it is very likely that there are interference effects from the events immediately above the Glenburn trough, because there are two or three peaks above the Glenburn trough at about 975-995 ms that appear to "tune" into one very high amplitude, low frequency event at far offsets. In addition, there are two or three peaks at about 890-910 ms that exhibit a similar phenomenon. Because the Glenburn trough is less than a cycle away from

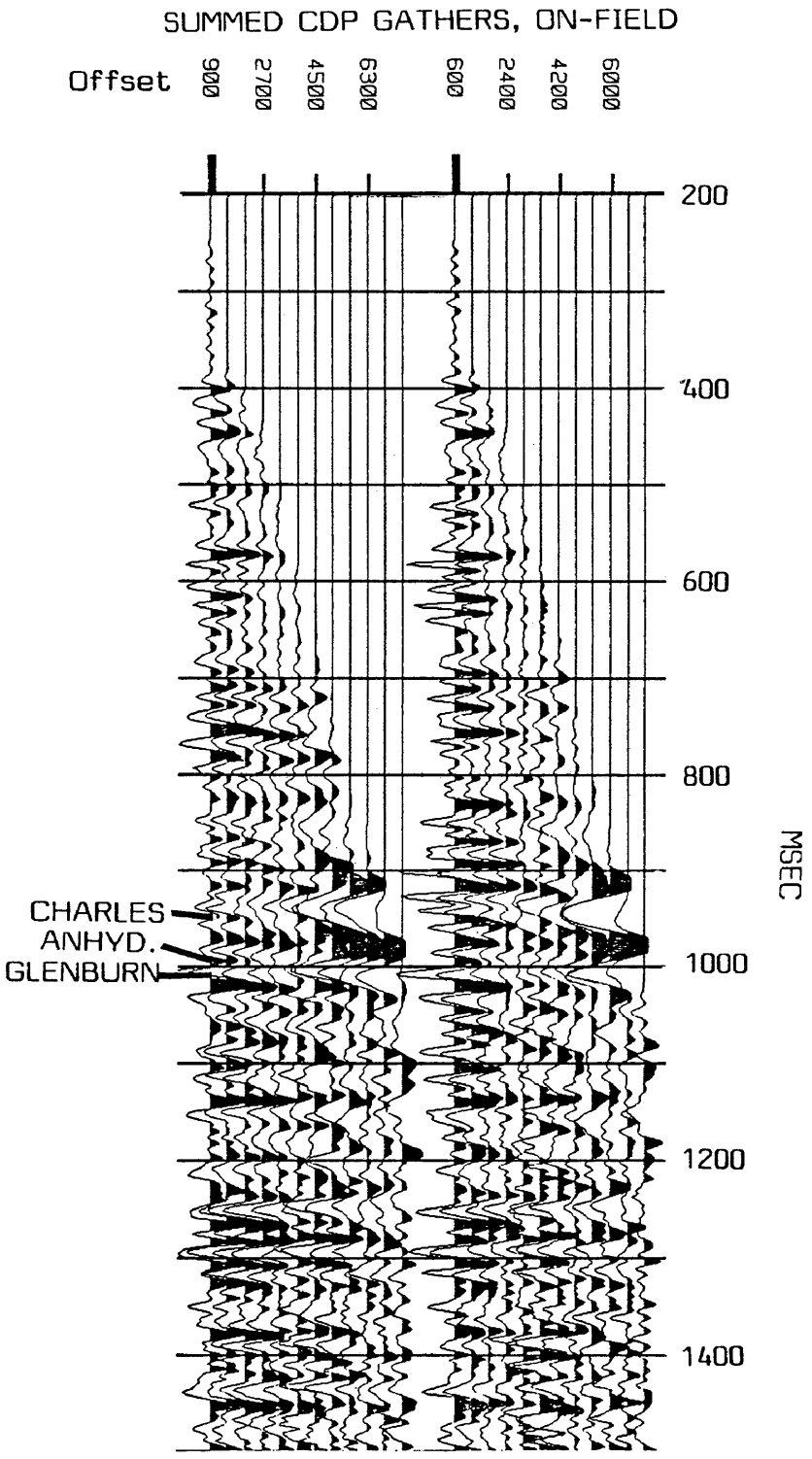

Figure 45. Representative on-field summed CDP gathers.

these high amplitude, low frequency events, the interference from these events appears to override the lithologic amplitude-offset changes that were to be analyzed by this thesis. The previously mentioned multiples also provide interference.

A contributing factor to the increase in amplitude at far offsets is linked to the modeled response of the shale-anhydrite interface. This response shows a large increase in amplitude as the critical angle is approached (Figure 22). It may be possible that a factor contributing to the amplitude increase seen at far offsets on the data is related to offsets that approach the critical angle. Although an estimate of the angle of incidence using a linear increase in velocity estimated from sonic logs showed a maximum angle of incidence of 35 degrees for the offset range of the seismic data, this estimate may be on the low side. The CSP models (Figures 29 - 34) also show an increase in amplitude, constructive interference, and a phase change at far offsets.

When the constructive interference of the events above the Glenburn trough becomes very noticeable, at offsets of 4200 to 4500 feet, the amplitude of the Glenburn dramatically increases again. Therefore, tuning effects appear to dominate at offsets greater than about

4200 feet. These tuning effects illustrate the danger of examining only changes in amplitude with offset. Although the tuning effects do not appear to change much across the seismic line used in this thesis, in other regions where there are abrupt changes in bed thickness or lithology, there may be abrupt character and amplitude changes with offset that are related to tuning effects.

Figure 46 shows two representative summed CDP gathers from the off-field portion of the seismic line. The most noticeable difference between the on-field and off-field summed CDP gathers at the Glenburn level appears to be the amplitude of the peak above the Glenburn trough. The peak represents the Frobisher-Alida anhydrite, and shows a reduced amplitude for the on-field locations on both the stacked section, where it essentially disappears, and the summed gathers. The reduced amplitude agrees with what might be expected because the anhydrite is much thinner over the Wiley field than it is off-field.

In addition to tuning and critical angle approach causes for the amplitude and frequency changes at far offsets, it is also possible that some NMO stretch may play a role due to the sudden increase in velocities at the shale-anhydrite interface. Whatever the reason for

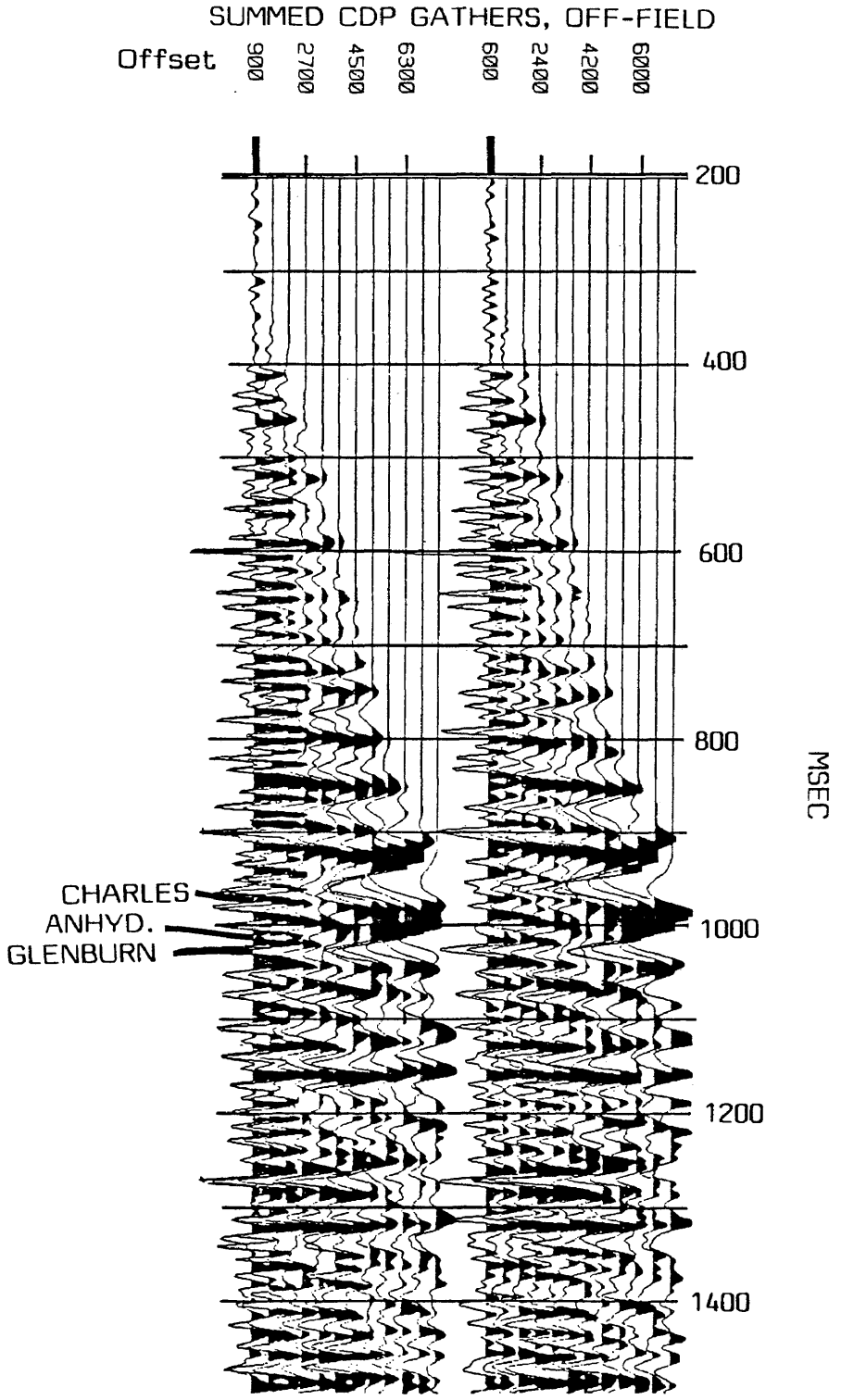

Figure 46. Representative off-field summed CDP gathers.

the change in frequency and amplitude at far offsets, in order for the modeled character of the Frobisher-Alida interval to be expressed on the seismic data, it was necessary to apply a vertical mute at an offset of 3600 feet from about 750 ms to 1010 ms to exclude the previously mentioned phenomenon from the stacked section.

Amplitude-Offset Analysis

Amplitude-offset analysis was done using an automatic tracking program called HTRACK that output times and amplitudes for the event of interest. The program picked the event based on user-supplied time control points, and chose the largest trough amplitude value within a 6 ms time window. Each amplitude value was linearly interpolated between 3 adjacent samples.

Only CDP gathers that were close to well projection locations were selected for analysis. The absolute value of amplitudes output by HTRACK were plotted versus feet of offset for display and analysis. These displays did not reveal any consistent difference between on-field and off-field locations. The overall amplitude levels appeared to be similar for the two cases.

The attempt at quantifying the amplitude-offset

differences using HTRACK may have been unsuccessful for several reasons:

(1) the HTRACK program was rather inflexible, and did not always choose the correct amplitude and time values when interpolating between control points.

(2) A characteristic amplitude-offset trend for the off-field versus the on-field locations may have been more obvious if all the summed CDP gathers had been analyzed, rather than only those that were adjacent to well projection locations. However, due to the large amount of operator control required by HTRACK, that was not feasible for this study. An interactive tracking program might have yielded better results.

(3) Amplitude analysis alone may not be sufficient. Character and phase changes would provide more conclusive information than amplitude alone.

Common offset stacks were displayed by sorting the vertically summed CDP gathers by offset. These common offset displays revealed noticeable differences in seismic character between the on-field and off-field locations. The near-offset stack (Figure 47) shows a decrease in the amplitudes of the peak-trough-peak sequence above the Glenburn trough and a change of this sequence to a peak

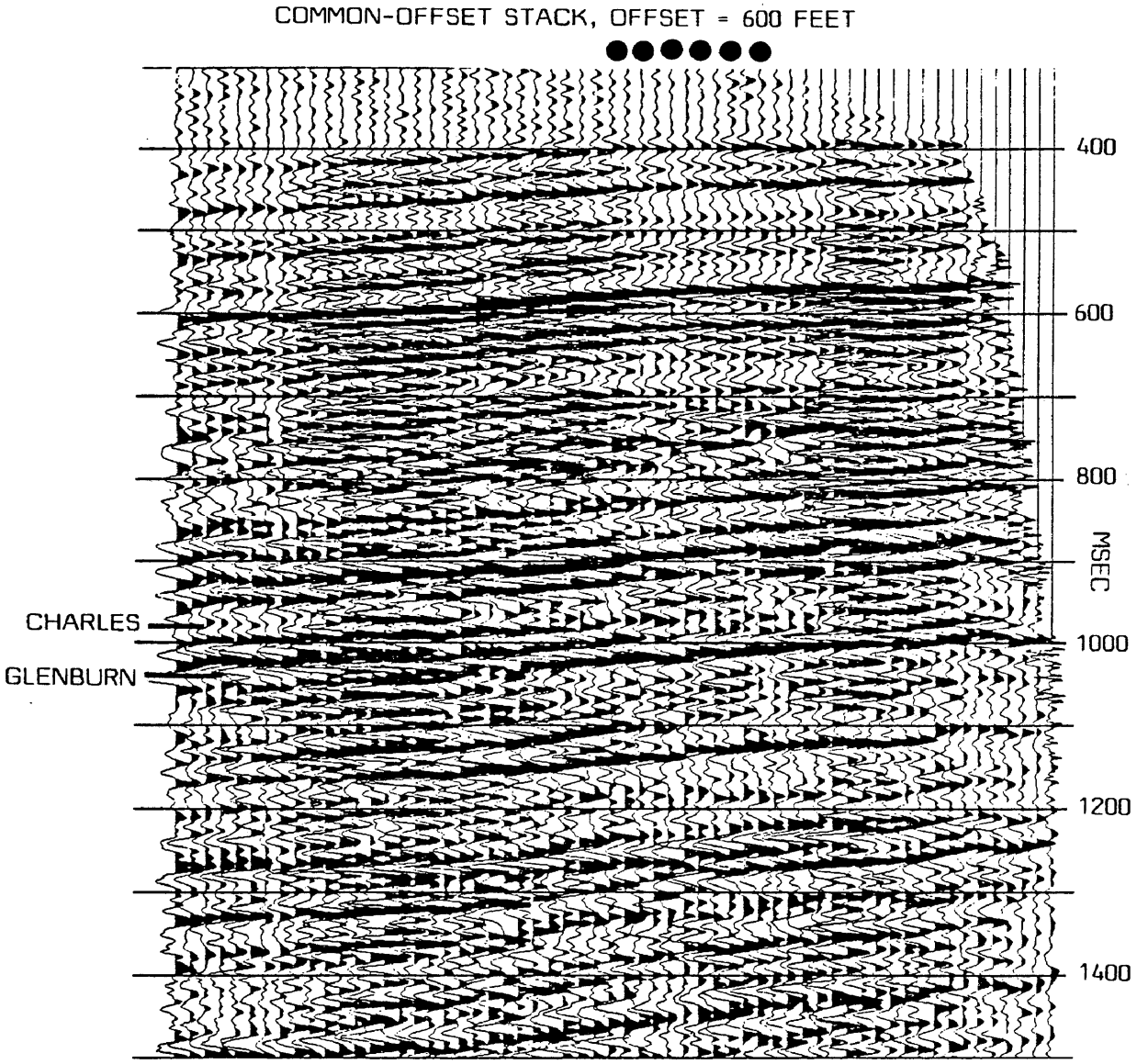

Figure 47. Near offset stack (common offset = 600 feet).

doublet as the difference between off-field and on-field seismic character at that level.

The change in character of the events above the Glenburn trough, and the relative decrease in amplitude of the Glenburn trough when comparing off-field and on-field seismic character become more evident as offset distance increases, out to about 2700 feet (Figure 48). At offsets greater than this, the character of the events begins to degrade. At offsets greater than about 4500 feet (Figure 49), the change in frequency of the events in the neighborhood of the Glenburn trough becomes apparent, and it is difficult to see a change in character or amplitude between the off-field and on-field locations.

The analysis of the commmon-offset stacks suggests that there is a subtle difference between off-field and on- field seismic character and amplitude of the Glenburn trough that is not evident from simple amplitude-offset analysis. However, it is difficult to separate the contributing causes of the overall response, i.e. lithologic changes, thickness , and porosity.

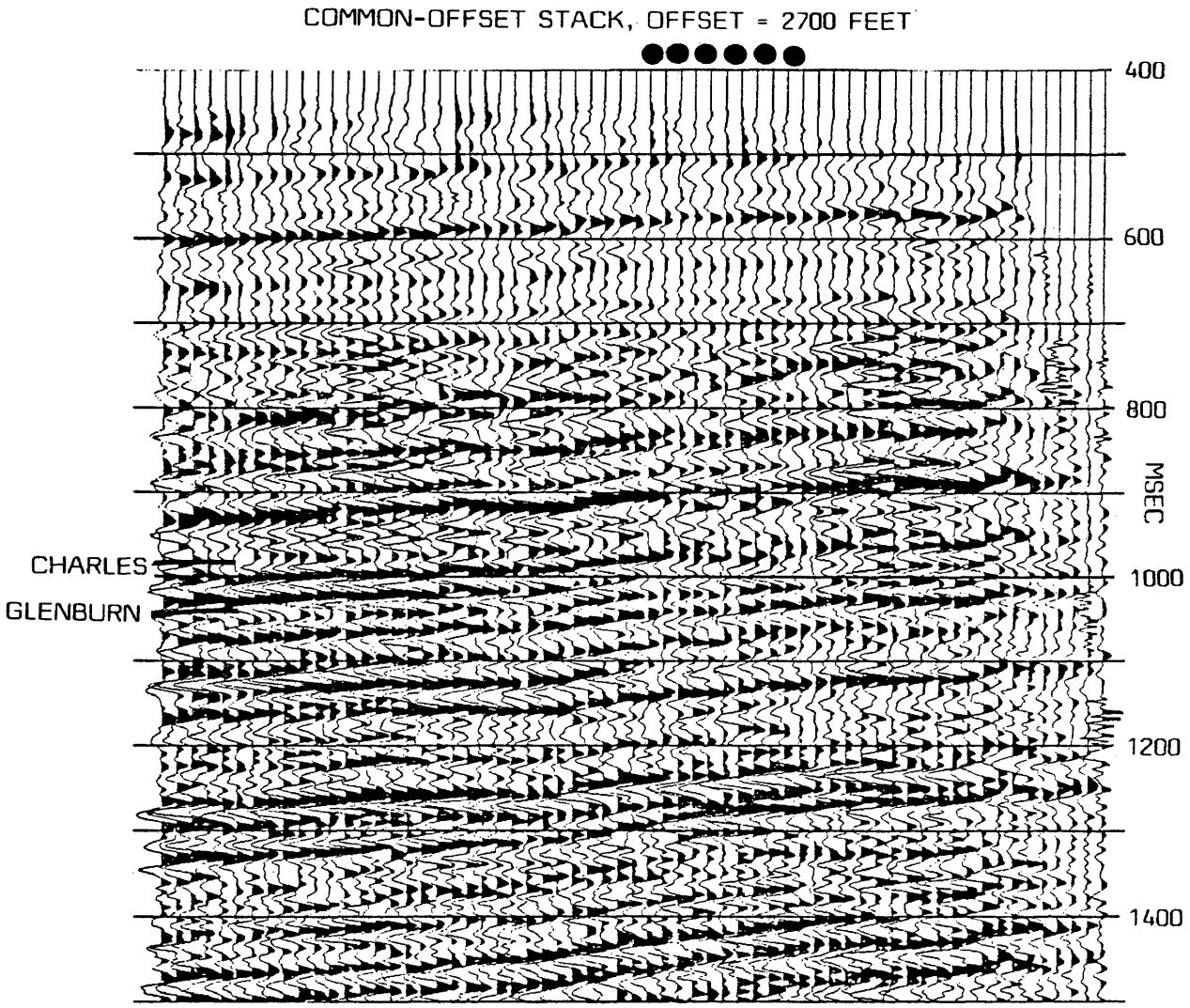

Figure 48. Intermediate offset stack (common offset = 2700 feet).

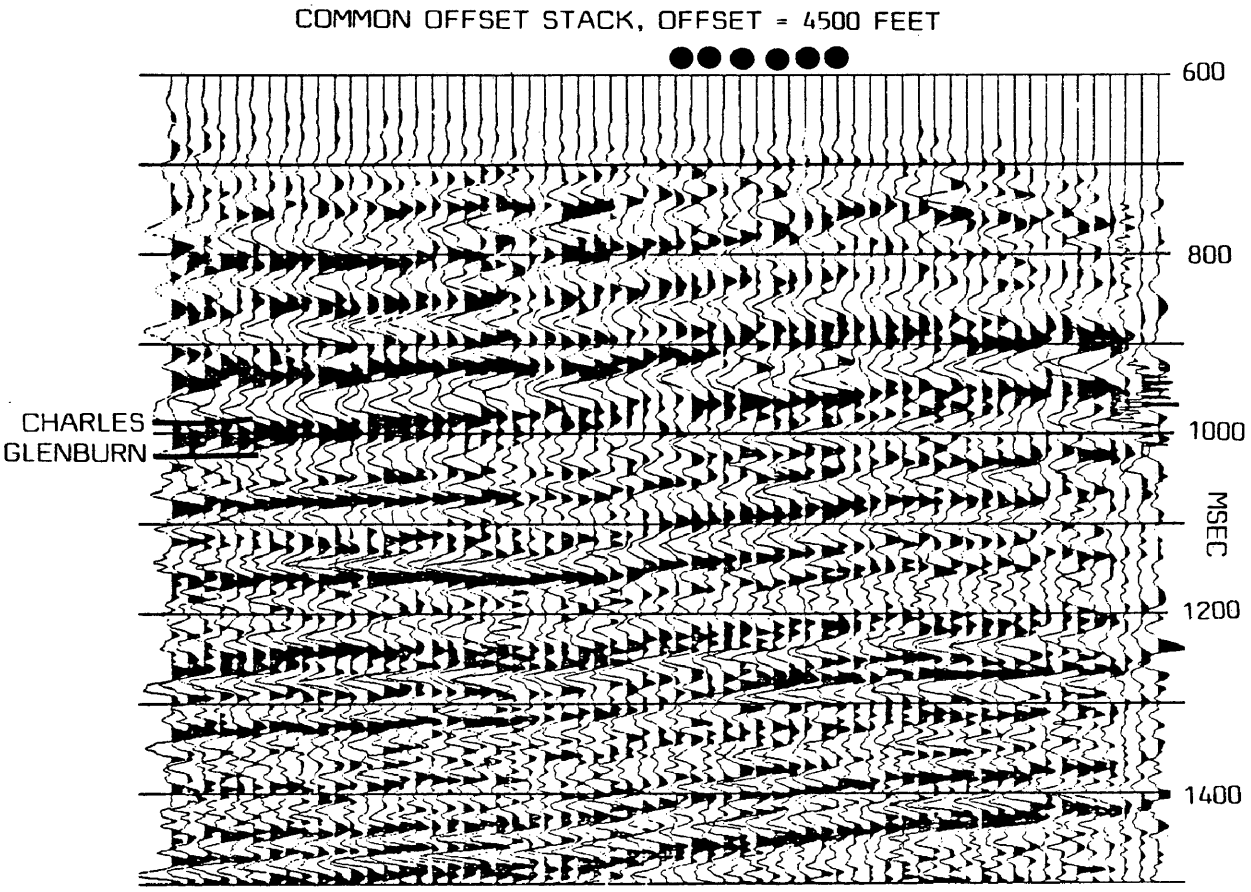

Figure 49. Far offset stack (common offset = 4500 feet).

FUTURE WORK

Future work that could help to better define the offset related character and amplitude changes at the Wiley Field include:

1) Amplitude-offset modeling involving the use of well logs, to account for gradational impedance boundaries and thin-layer effects.

2) Modeling with a wave-equation based algorithm may give more accurate results than the ray-theory based programs used in this thesis.

3) Inclusion of phase information in the amplitude-offset analysis.

4) Use of an interactive work station based amplitude tracking program should allow for more accurate amplitude picking and may allow for quantitative amplitude-offset analysis.

5) Comparison of P- and S-wave stacked sections such as those used by Robertson may delineate porous carbonates better than amplitude-offset analysis.

6) Shooting a three-component seismic survey across the Wiley Field.

CONCLUSIONS

From this study the following conclusions are drawn:

1) Constructive interference (tuning) of events above the Glenburn trough is the dominant effect at offsets greater than 4500 feet. Amplitude increase with offset due to critical angle approach for the events directly above the Glenburn may also contribute at far offsets. Dramatic amplitude and frequency changes at longer offsets can have important effects on stacked seismic sections, including erroneous velocity analyses and unexpected amplitude changes. Proper muting is essential.

2) The character and amplitude change that delineates the change from off-field to on-field geology is most evident at offsets centered on 2700 feet. The character is more evident at offsets beyond zero offset out to the distance of approximately 3600 feet. Common offset stacks are a useful interpretation tool.

3) Use of moved-out CDP gathers during velocity analysis, rather than only stacked traces should lead to more accurate velocities. Correct velocities are essential, especially when analyzing character and amplitude changes on stacked or partially stacked traces.

Accurate static corrections are also necessary for amplitude and character analysis.

4) Amplitude changes with offset are probably insufficient to allow detection of the difference between porous carbonate and nonporous carbonate. However, the magnitude of the amplitude from the common offset stacks may discriminate sufficiently to outline the facies change from evaporite to carbonate in the Glenburn Member of the Mission Canyon Formation. The facies change from carbonate to anhydrite, and the related thickness changes, rather than changes in porosity, were determined to be the dominant cause for the character and amplitude changes between on-field and off-field locations.

REFERENCES CITED

Almoghrabi, H. and J. Lange. 1986. Layers and bright spots. Geophysics 51 (3): 699 - 709.

Chiburis, E. F. 1987. Studies of amplitude versus offset in Saudi Arabia. Expanded Abstracts. 57th Annual National Convention, Society of Exploration Geophysicists: New Orleans, Louisiana, p. 614-616.

Domenico, S. N. 1984. Rock lithology and porosity determination from shear and compressional wave velocity. Geophysics 49 (8): 1188 - 1195.

Gassaway, G. S., A. R. Brown, and L. E. Bennett. 1986. Pitfalls in seismic amplitude versus offset analysis: Case histories. Expanded Abstracts. 56th Annual National Convention, Society of Exploration Geophysicists: Houston, Texas, p. 332-334.

Gassaway, G. S. and H. J. Richgels. 1983. SAMPLE: Seismic amplitude measurements for primary lithology estimation. Expanded Abstracts. 53rd Annual National Convention, Society of Exploration Geophysicists: Las Vegas, Nevada, p. 610 - 613.

Gassaway, G. S. N.d. Seismic lithology and pore fluids using the SAMPLE method. Terra Linda Group, Inc., notes from short course, 42 p.

Gassman, F. 1951. Über die elastizität Porözer Medien: Natur. Gesellschaft Zurich, Vierteljahrssch. 96, p. 1-23.

Gregory, A.R. 1976. Fluid saturation effects on dynamic elastic properties of sedimentary rocks. Geophysics 41 (5): 895-913.

Koefoed, O. 1962. Reflection and transmission coefficients for plane longitudinal incident waves. Geophysical Prospecting 10: 304-351.

Koefoed, O. 1955. On the effect of Poisson's ratio of rock strata on the reflection coefficients of plane waves. Geophysical Prospecting. 381-387.

Mueller, T.L. 1987. A seismic-stratigraphic analysis of Starkey and Winters Gas Reservoirs, using amplitude-offset studies from the Crossroads Field, Sacramento Valley, California. Master's Thesis no. T-3370, Colorado School of Mines, Golden, Colorado. 131 p.

Muskat, M. and M.W. Meres. 1940. Reflection and transmission coefficients for plane waves in elastic media. Geophysics 5: 115-155.

Nafe, J.E. 1957. Reflection and transmission coefficients at a solid-solid interface of high velocity contrast. Bull. Seis. Soc. of America.

Ostrander, W.J. 1984. Plane wave reflection coefficients

for gas sands at non-normal angles of incidence. Geophysics 49 (10): 1637-1648.

Rafavich, F., C.H.St.C. Kendall, and T.P. Todd. 1984. The relationship between acoustic properties and the petrographic character of carbonate rocks. Geophysics 49 (10): 1622-1636.

Reeve, D.M. 1986. Seismic detection of Mississippian Frobisher-Alida Facies, Wiley and Mouse River Park Fields, Bottineau and Renville Counties, Williston Basin, North Dakota. Master's Thesis no. T-3255, Colorado School of Mines, Golden, Colorado. 87 p.

Robertson, J.D. 1987. Carbonate porosity from S/P traveltime ratios. Geophysics 52 (10): 1346-1354.

Shanley, K.W. 1983. Stratigraphy and depositional model, Upper Mission Canyon Formation (Mississippian) northeast Williston Basin, North Dakota. Master's Thesis, Colorado School of Mines, Golden, Colorado. 172 p.

Towle, G. 1978. Stress effects on acoustic velocities of rocks. Master's Thesis no. T-1702, Colorado School of Mines, Golden, Colorado. 235 p.

Waters, K.H. 1981. Reflection Seismology: A tool for energy resource exploration. 2nd ed. New York: John

Wiley and Sons. 453 p.

Xiochun, Ma. 1986. Fortran Program for the solution of Zoeppritz equations. Unpublished. CSM Geophysics Department Library.

Yu, G. 1985. Offset-amplitude variation and controlled-amplitude processing. Geophysics 50 (12): 2697-2708.

APPENDIX 1

Inexco Oil Co. Olson #1-12 swse sec 12-154N-85W

SAMPLE 1 (B593 6295-6296)

massive anhydrite

dry wt. air	32.912	wet wt. air	32.977
wet wt. water	16.657	length	.870
vol.	11.000	phi	.500%

Density

dry, air	2.939	bulk air	2.990
bulk water	3.000	matrix	3.010

POISSON'S RATIOS

dry	0.300	wet	0.338

Pc	Pp	Tp	Vp	Ts	Vs
		Dry			
1000	0	15.70	16740	29.02	9240
2000	0	15.55	17300	28.95	9320
3000	0	15.40	18000	28.77	9540
4000	0	15.39	18000	28.55	9820
5000	0	15.34	18300	28.52	9860
3000	2000	15.45	17800	28.80	9500
4000	2000	15.39	18000	28.63	9720
5000	2000	15.29	18500	28.47	9930
6000	2000	15.23	18800	28.43	9990
7000	2000	15.19	19000	28.34	10100

Pc	Pp	Tp	Vp	Ts	Vs
		Water Saturated			
1000	0	15.19	18979	29.32	8896
2000	0	15.12	19333	28.72	9602
3000	0	15.01	19918	28.71	9615
4000	0	14.97	20139	28.51	9877
5000	0	14.91	20480	28.37	10069
3000	2000	15.10	19437	29.34	8874
4000	2000	15.09	19489	28.75	9565
5000	2000	14.99	20027	28.59	9771
6000	2000	14.93	20365	28.45	9959
7000	2000	14.93	20365	28.39	10042

SAMPLE 2 (B593 6282-6283)

appears nonporous, subtidal carbonate

dry wt. air	25.855	wet wt. air	27.907
wet wt. water	16.657	length	.882
vol.	11.100	phi	18.500%

Density

dry, air	2.035	bulk air	2.320
bulk water	2.510	matrix	2.850

POISSON'S RATIOS

dry	0.257	wet	0.288

Pc	Pp	Tp	Vp	Ts	Vs
		Dry			
1000	0	15.91	16189	29.05	9327
2000	0	15.82	16517	28.84	9583
3000	0	15.75	16781	28.68	9787
4000	0	15.68	17053	28.65	9826
5000	0	15.58	17458	28.61	9879

Pc	Pp	Tp	Vp	Ts	Vs
3000	2000	15.82	16517	29.09	9280
4000	2000	15.74	16819	28.72	9735
5000	2000	15.67	17093	28.68	9786
6000	2000	15.62	17294	28.69	9774
7000	2000	15.62	17294	28.60	9892

Pc	Pp	Tp	Vp	Ts	Vs
		Water Saturated			
1000	0	15.87	16333	29.56	8760
2000	0	15.68	17053	29.32	9018
3000	0	15.65	17173	29.20	9153
4000	0	15.57	17500	28.88	9533
5000	0	15.52	17711	28.80	9633
3000	2000	16.15	17495	30.69	8784
4000	2000	16.08	17755	30.32	9139
5000	2000	15.99	18100	30.30	9159
6000	2000	15.95	18259	30.26	9199
7000	2000	15.95	18259	30.14	9323

SAMPLE 3 (B593 6285)

"porous" fine-grained carbonate, lt. oil stain, intertidal

dry wt. air	25.858	wet wt. air	27.427
wet wt. water	16.802	length	.827
vol.	10.500	phi	14.800%

Density

dry, air	2.429	bulk air	2.460
bulk water	2.610	matrix	2.890

POISSON'S RATIOS

dry	0.281	wet	0.319

Pc	Pp	Tp	Vp	Ts	Vs
		Dry			
1000	0	15.95	15047	29.02	8779
2000	0	15.72	15843	28.93	8881
3000	0	15.60	16292	28.91	8904
4000	0	15.58	16370	28.82	9009
5000	0	15.54	16527	28.64	9226
3000	2000	15.91	15180	29.18	8604
4000	2000	15.82	15487	29.01	8790
5000	2000	15.73	15807	28.99	8813
6000	2000	15.63	16178	28.77	9067
7000	2000	15.55	16487	28.73	9116
Pc	Pp	Tp	Vp	Ts	Vs
		Water Saturated			
1000	0	15.87	15315	30.22	7615
2000	0	15.77	15663	29.44	8333
3000	0	15.64	16139	29.49	8283
4000	0	15.55	16487	29.38	8394
5000	0	15.50	16687	29.29	8487
3000	2000	15.78	15627	30.15	7674
4000	2000	15.64	16140	29.69	8089
5000	2000	15.64	16140	29.54	8234
6000	2000	15.62	16216	29.40	8374
7000	2000	15.56	16449	29.31	8466

Monsanto #2 Ring, sec 32-162N-83W

SAMPLE 4 (B708 4410)

peritidal carbonate, vuggy porosity

dry wt. air	33.039	wet wt. air	35.584
wet wt. water	21.264	length	1.119
vol.	14.200	phi	17.800%

Density

dry, air	2.294	bulk air	2.330
bulk water	2.510	matrix	2.840

POISSON'S RATIO

dry	0.286	wet	0.304

Pc	Pp	Tp	Vp	Ts	Vs
		Dry			
1000	0	16.50	18177	30.37	10136
2000	0	16.44	18393	30.32	10191
3000	0	16.34	18763	30.21	10315
4000	0	16.31	18877	30.20	10327
5000	0	16.28	18992	30.16	10373
3000	2000	16.60	17830	30.40	10103
4000	2000	16.42	18465	30.27	10247
5000	2000	16.42	18465	30.20	10327
6000	2000	16.38	18613	30.19	10338
7000	2000	16.28	18992	30.18	10350
Pc	Pp	Tp	Vp	Ts	Vs
		Water Saturated			
1000	0	16.52	18107	31.21	9288
2000	0	16.44	18393	30.91	9574
3000	0	16.33	18800	30.72	9764
4000	0	16.38	18613	30.67	9816
5000	0	16.28	18992	30.55	9941
3000	2000	16.39	18576	31.41	9106
4000	2000	16.40	18539	30.78	9703
5000	2000	16.35	18725	30.68	9805
6000	2000	16.28	18992	30.49	10005
7000	2000	16.28	18992	30.40	10103

SAMPLE 5 (B708 4401)

peritidal carbonate, vuggy porosity

dry wt. air	31.346	wet wt. air	32.816
wet wt. water	19.767	length	1.019
vol.	12.900	phi	11.300%

Density

dry, air	2.390	bulk air	2.430
bulk water	2.550	matrix	2.740

POISSON'S RATIO

dry	0.287	wet	0.321

Dry

Pc	Pp	Tp	Vp	Ts	Vs
1000	0	16.20	17581	30.24	9362
2000	0	16.16	17728	29.86	9772
3000	0	16.08	18029	29.78	9863
4000	0	16.02	18262	29.66	10001
5000	0	15.97	18460	29.54	10145
3000	2000	16.17	17691	29.98	9639
4000	2000	16.10	17953	29.80	9840
5000	2000	16.04	18183	29.74	9909
6000	2000	15.99	18380	29.71	9943
7000	2000	15.96	18500	29.64	10026

Water Saturated

Pc	Pp	Tp	Vp	Ts	Vs
1000	0	16.09	17991	30.52	9082
2000	0	15.98	18420	30.27	9332
3000	0	15.93	18622	30.14	9467
4000	0	15.93	18622	30.08	9530
5000	0	15.87	18870	29.91	9716

Pc	Pp	Tp	Vp	Ts	Vs
3000	2000	15.99	18380	30.40	9200
4000	2000	15.97	18460	30.34	9260
5000	2000	15.89	18787	30.09	9520
6000	2000	15.85	18955	29.88	9749
7000	2000	15.82	19082	29.84	9794

SAMPLE 6 (B708 4366)

very fine grained peritidal carbonate mudstone

dry wt. air	33.031	wet wt. air	34.788
wet wt. water	21.880	length	1.061
vol.	2.800	phi	13.600%

Density

dry, air	2.419	bulk air	2.590
bulk water	2.730	matrix	3.000

POISSON'S RATIO

dry	0.235	wet	0.289

Pc	Pp	Tp	Vp	Ts	Vs
Dry					
1000	0	16.47	17337	29.84	10198
2000	0	16.40	17578	29.73	10329
3000	0	16.38	17648	29.61	10476
4000	0	16.33	17825	29.58	10513
5000	0	16.31	17898	29.56	10538
3000	2000	16.44	17439	29.84	10198
4000	2000	16.38	17648	29.70	10365
5000	2000	16.32	17862	29.56	10538
6000	2000	16.33	17825	29.56	10538
7000	2000	16.33	17825	29.56	10538

Pc	Pp	Tp	Vp	Ts	Vs
		Water Saturated			
1000	0	16.44	17439	30.50	9477
2000	0	16.37	17683	30.36	9621
3000	0	16.34	17790	30.25	9738
4000	0	16.29	17970	30.17	9824
5000	0	16.27	18044	30.17	9824
3000	2000	16.39	17613	30.31	9674
4000	2000	16.31	17898	30.27	9716
5000	2000	16.31	17898	30.19	9802
6000	2000	16.27	18044	30.19	9802
7000	2000	16.27	18044	30.20	9791

SAMPLE 7 (B708 4406)

peritidal carbonate, vuggy porosity

dry wt. air	30.504	wet wt. air	31.955
wet wt. water	19.145	length	1.003
vol.	12.700	phi	11.300%

Density

dry, air	2.362	bulk air	2.410
bulk water	2.520	matrix	2.840

POISSON'S RATIO

dry	0.285	wet	0.317

Pc	Pp	Tp	Vp	Ts	Vs
		Dry			
1000	0	16.39	16658	30.09	9375
2000	0	16.23	17207	30.05	9417
3000	0	16.21	17278	29.98	9492
4000	0	16.18	17386	29.94	9535
5000	0	16.18	17386	29.94	9535

Pc	Pp	Tp	Vp	Ts	Vs
3000	2000	16.30	16962	30.06	9406
4000	2000	16.28	17032	30.02	9449
5000	2000	16.22	17242	29.98	9492
6000	2000	16.21	17278	29.94	9535
7000	2000	16.18	17386	29.92	9557

Pc	Pp	Tp	Vp	Ts	Vs
		Water Saturated			
1000	0	16.26	17101	30.64	8831
2000	0	16.21	17278	30.46	9002
3000	0	16.16	17458	30.31	9149
4000	0	16.14	17531	30.32	9139
5000	0	16.12	17605	30.15	9312
3000	2000	16.15	17495	30.69	8784
4000	2000	16.08	17755	30.32	9139
5000	2000	15.99	18100	30.30	9159
6000	2000	15.95	18259	30.26	9199
7000	2000	15.95	18259	30.14	9323

APPENDIX 2

SAMPLE 1 Vp↑2 VS Pe↑1/3
+=BRINE SAT., SQU.=AIR SAT.

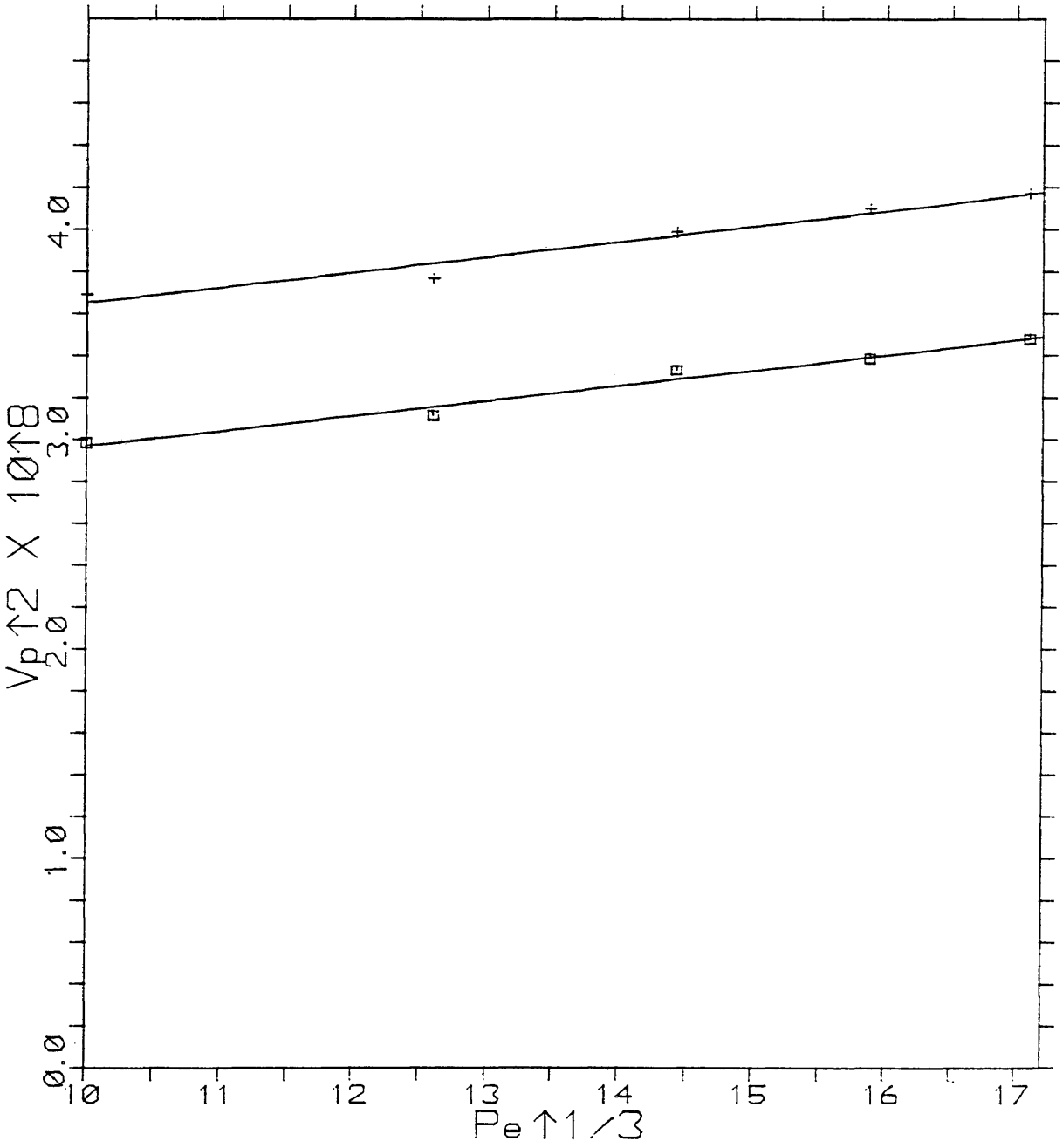

SAMPLE 1 Vs↑2 VS Pe↑1/3
+=BRINE SAT., SQU.=AIR SAT.

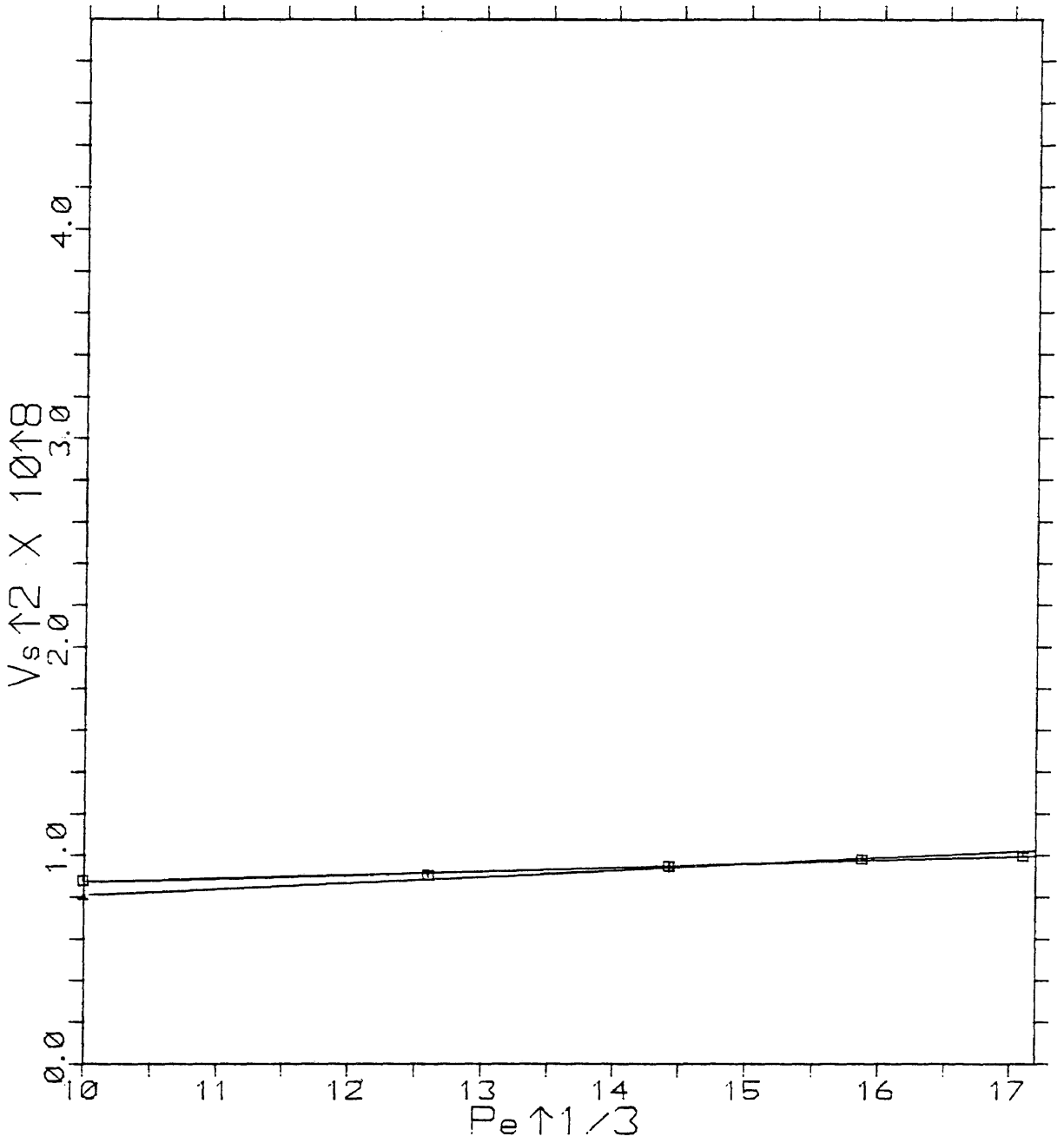

SAMPLE 3 Vp↑2 VS Pe↑1/3
+=BRINE SAT., SQU.=AIR SAT.

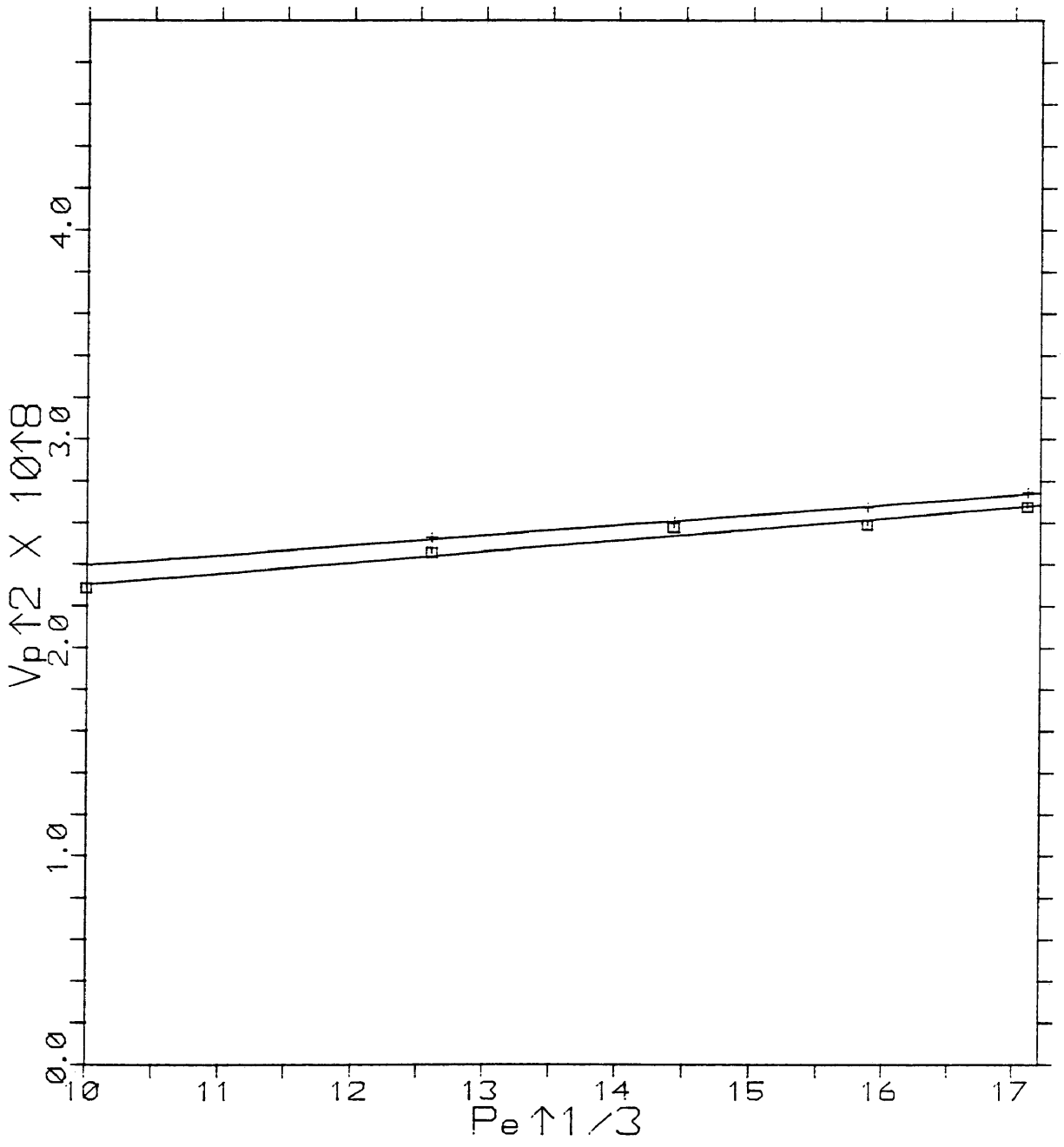

SAMPLE 3 Vs↑2 VS Pe↑1/3
+=BRINE SAT., SQU.=AIR SAT.

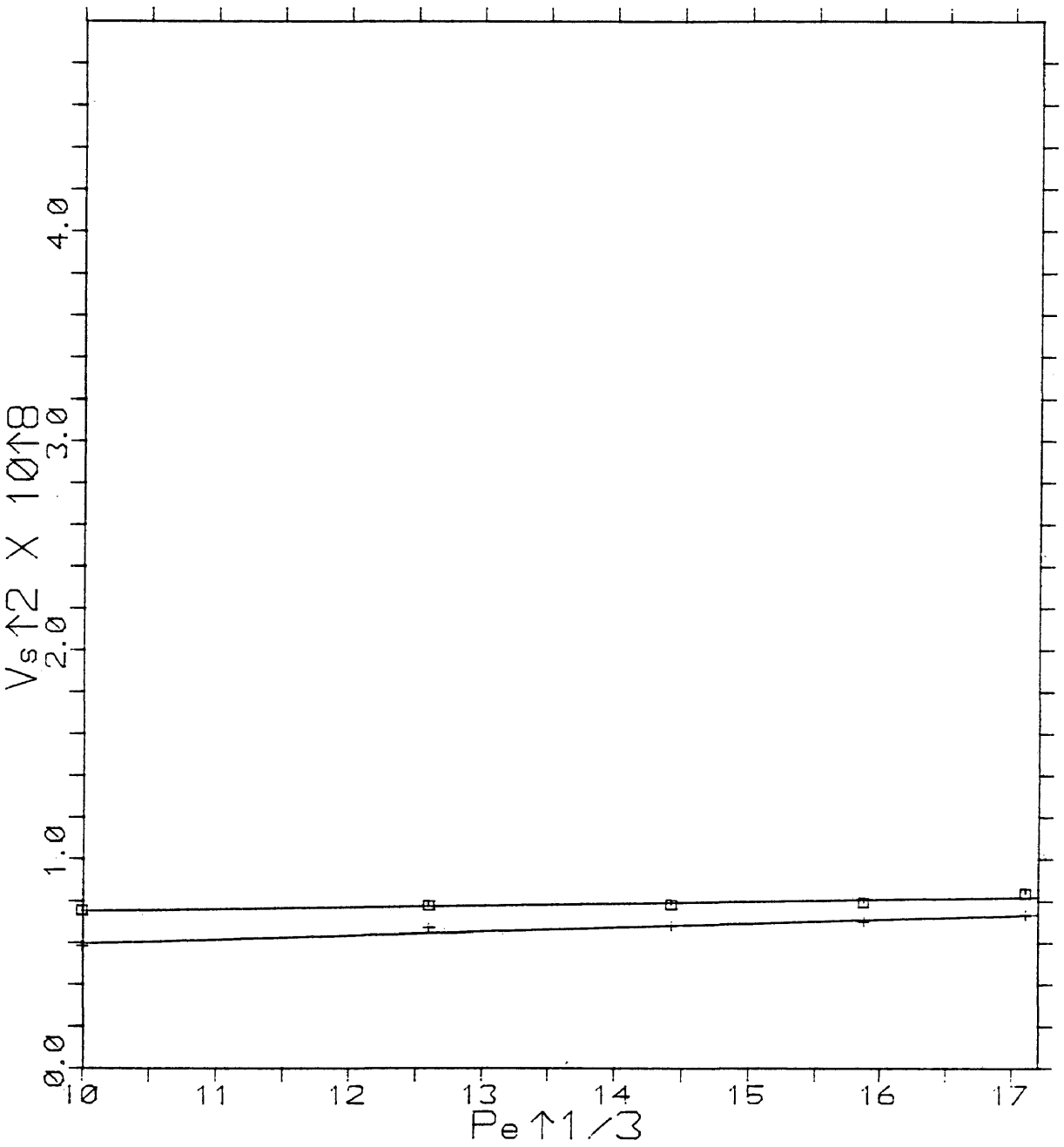

SAMPLE 4 Vp↑2 VS Pe↑1/3
+=BRINE SAT., SQU.=AIR SAT.

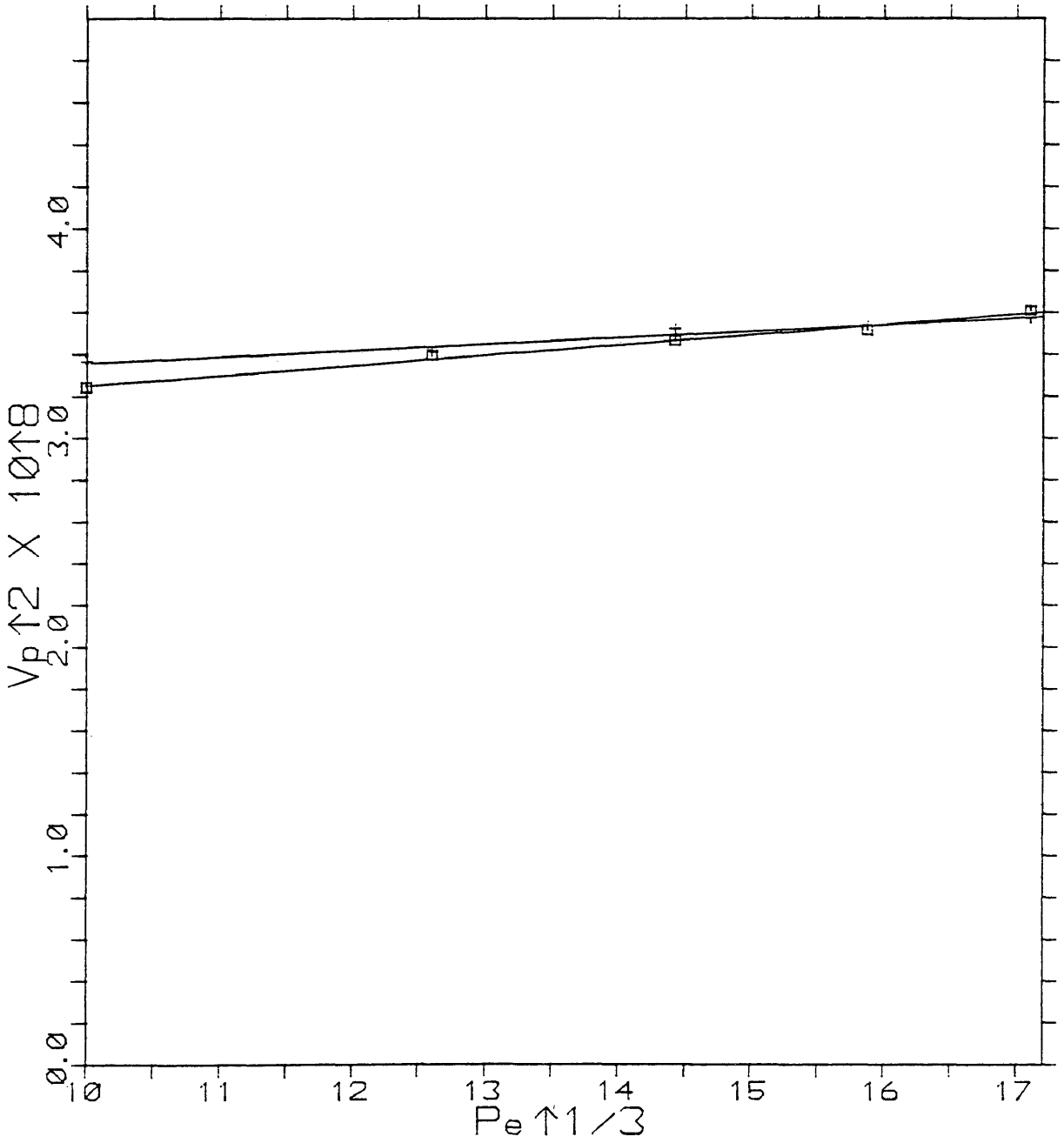

SAMPLE 4 Vs↑2 VS Pe↑1/3
+=BRINE SAT., SQU.=AIR SAT.

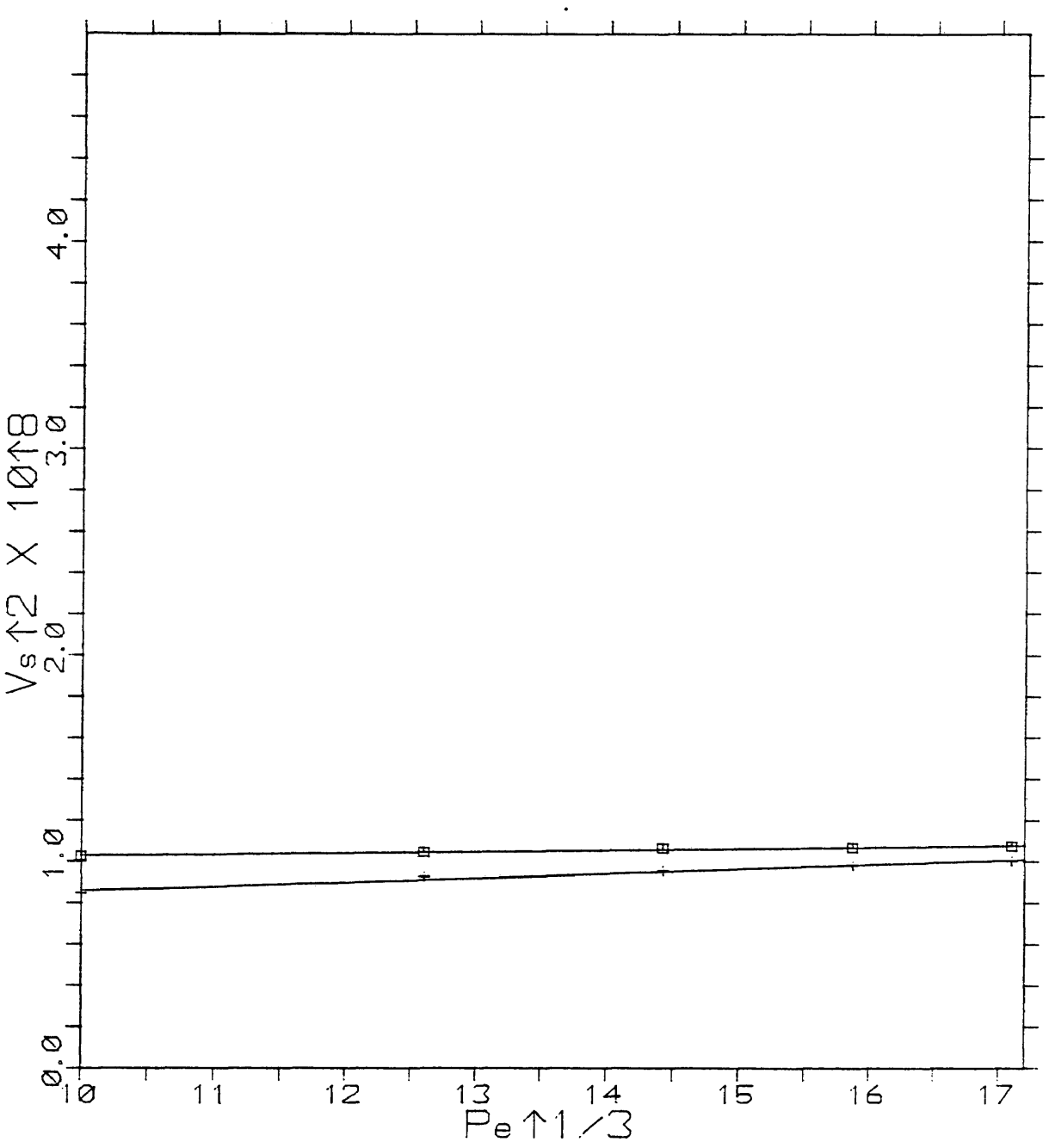

SAMPLE 5 Vp↑2 VS Pe↑1/3
+=BRINE SAT., SQU.=AIR SAT.

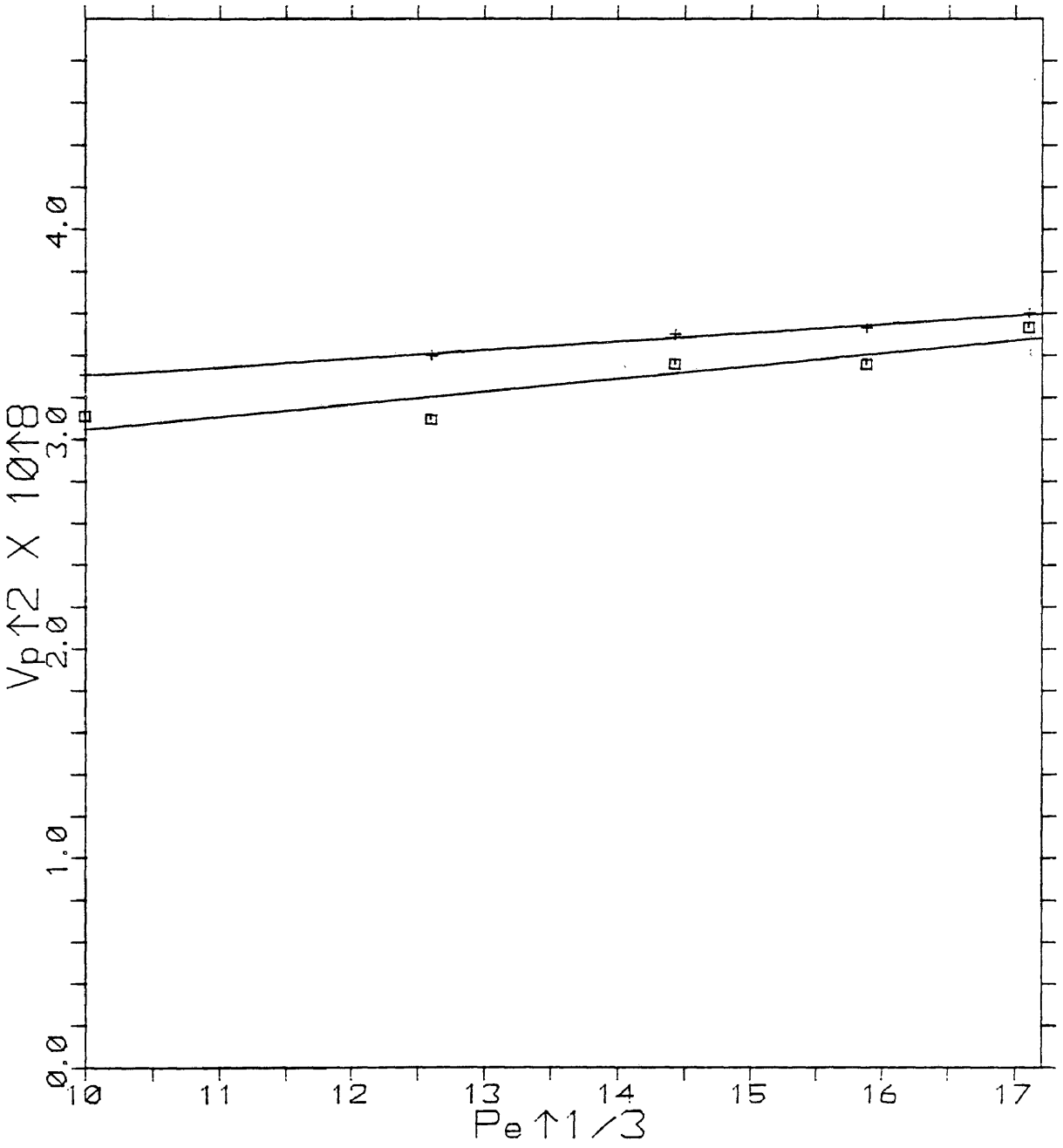

SAMPLE 5 Vs↑2 VS Pe↑1/3
+=BRINE SAT., SQU.=AIR SAT.

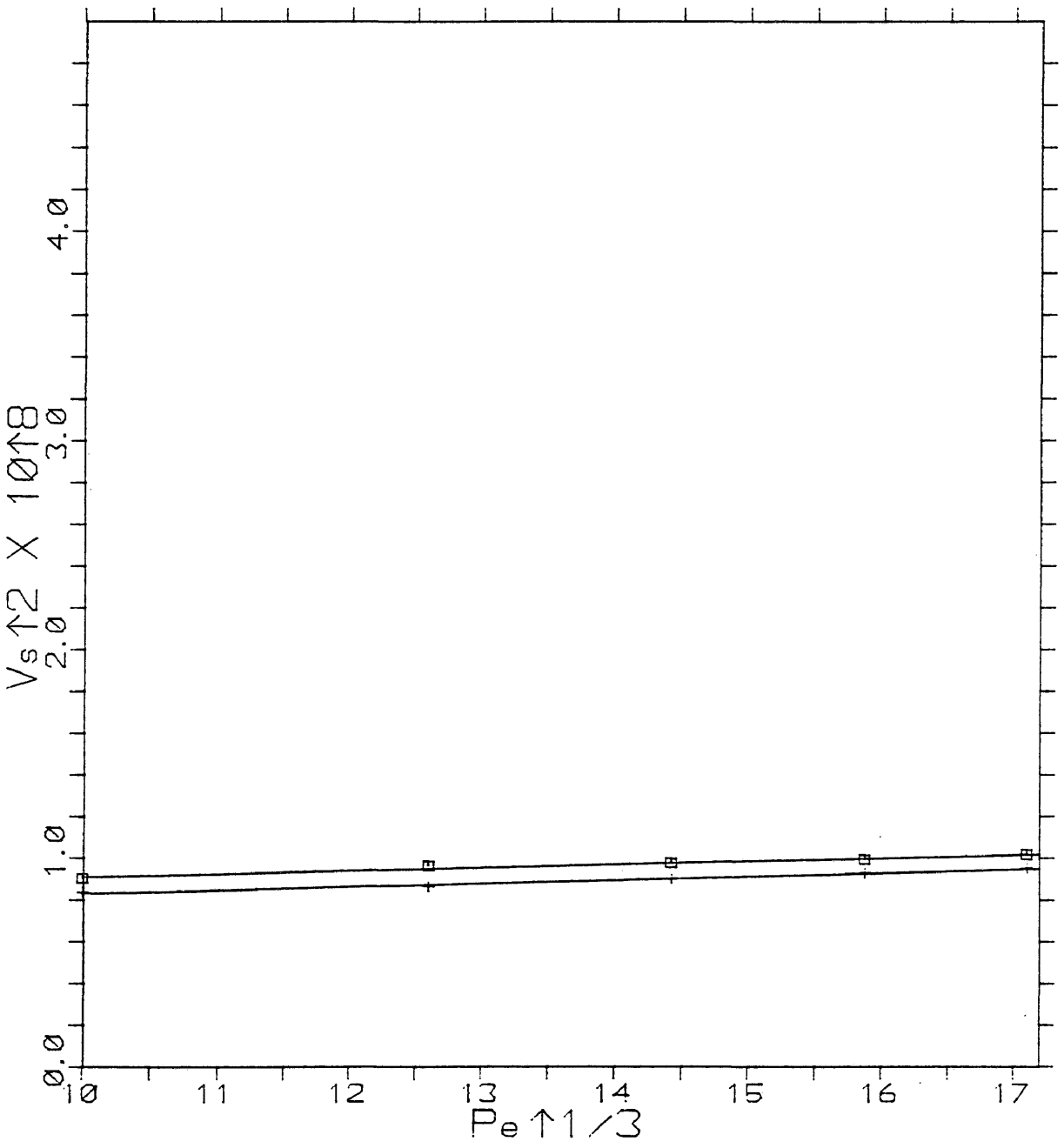

SAMPLE 6 Vp↑2 VS Pe↑1/3
+=BRINE SAT., SQU.=AIR SAT.

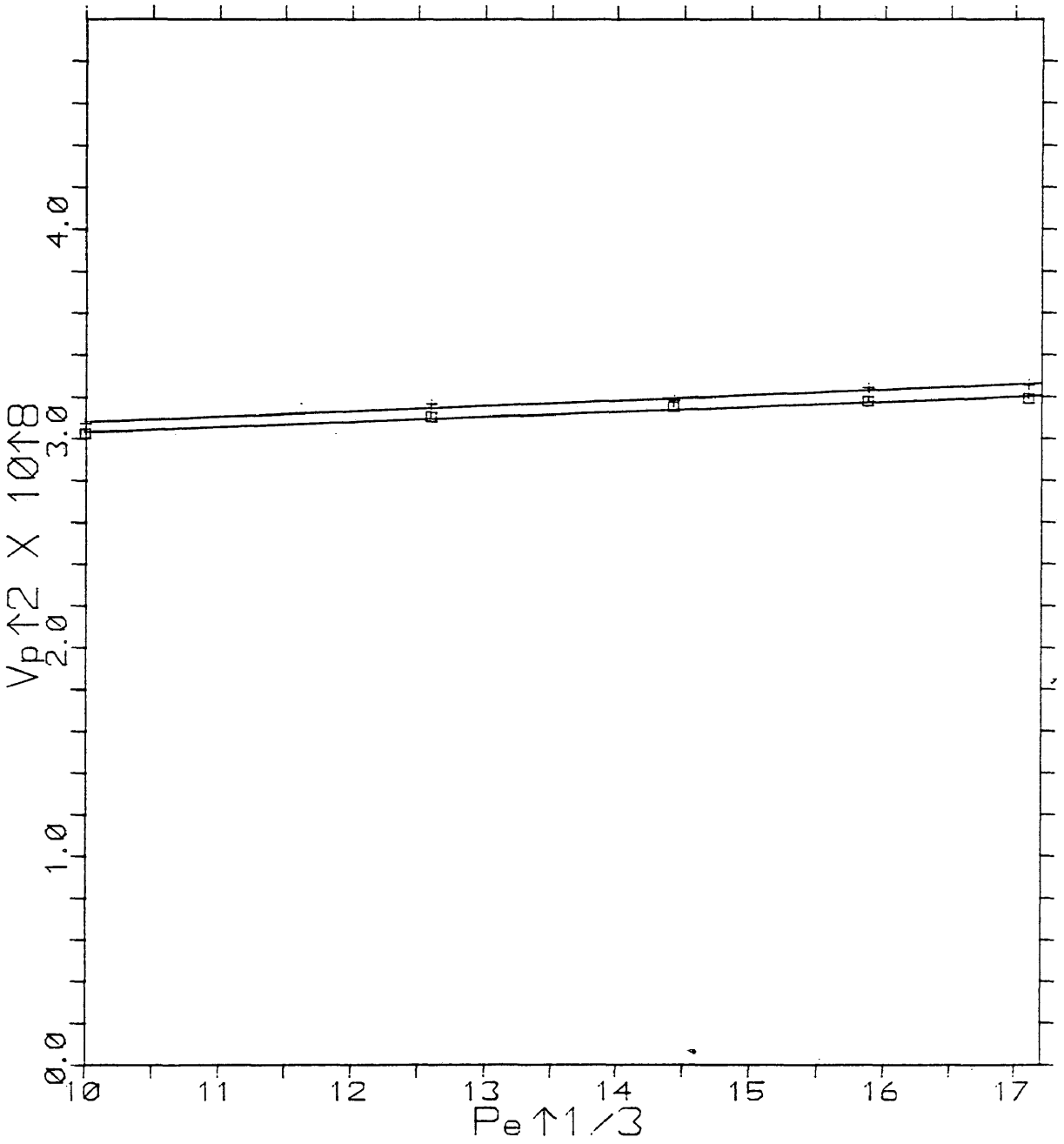

SAMPLE 6 Vs↑2 VS Pe↑1/3
+=BRINE SAT., SQU.=AIR SAT.

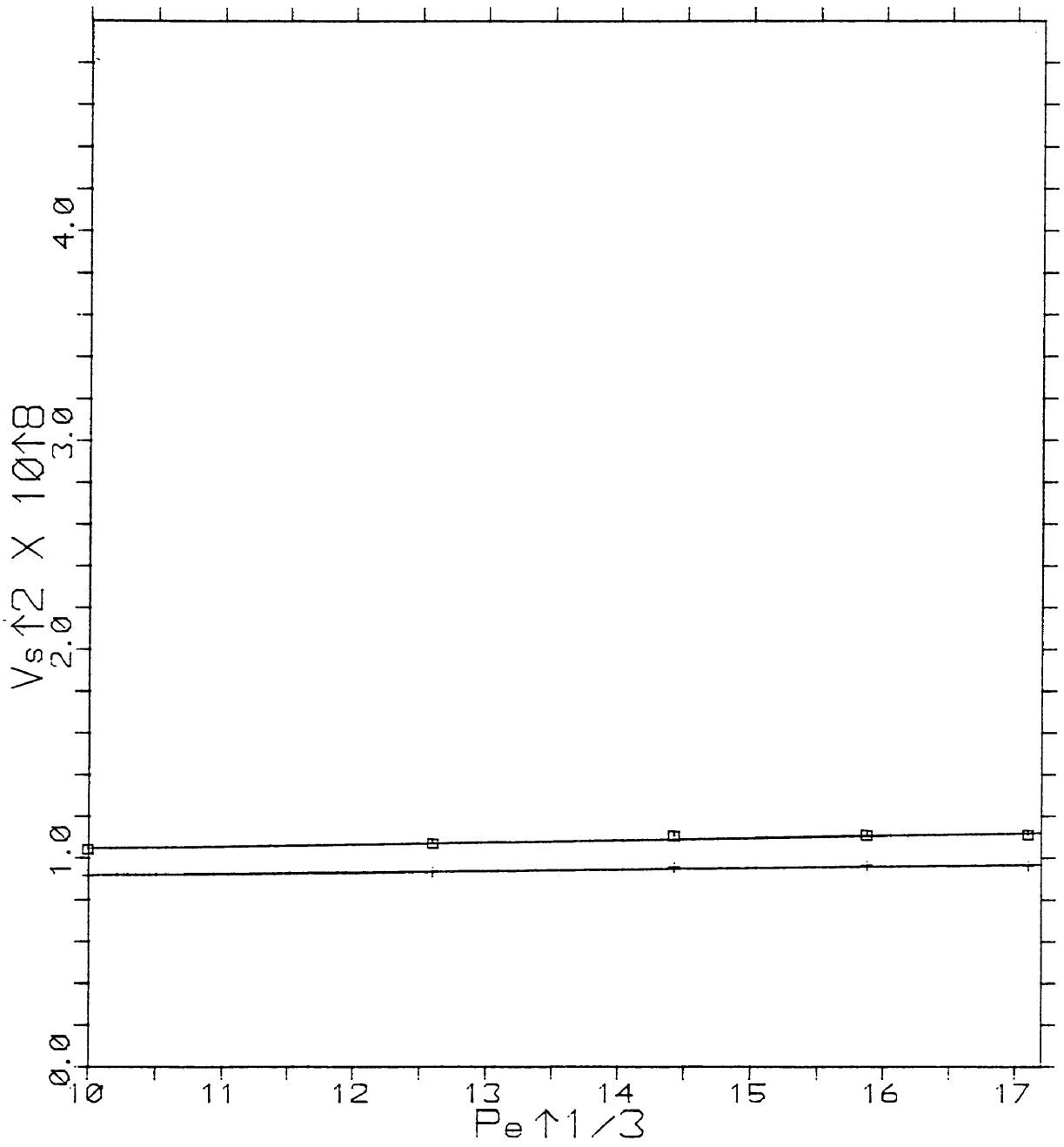

SAMPLE 7 Vp↑2 VS Pe↑1/3
+=BRINE SAT., SQU.=AIR SAT.

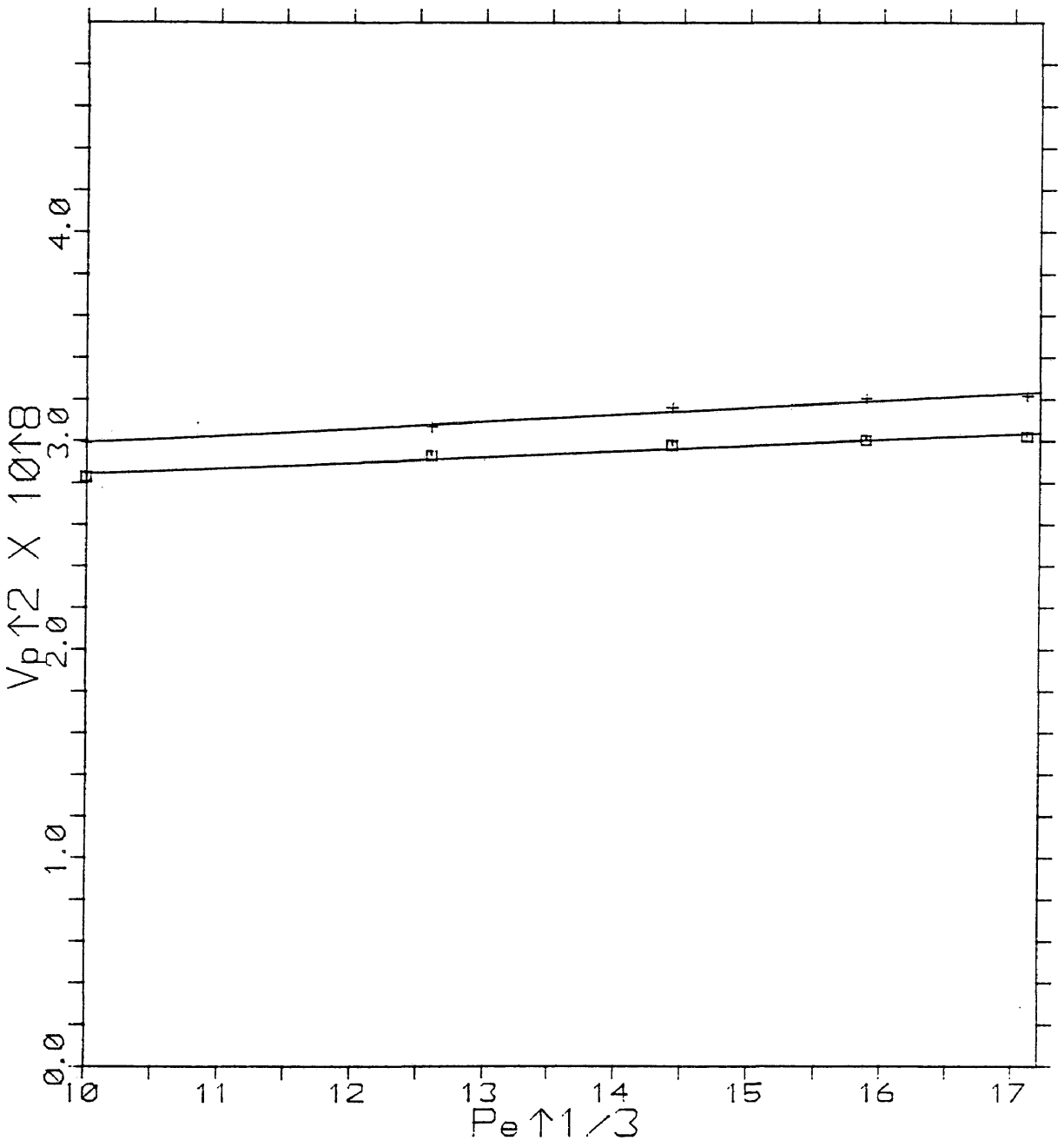

SAMPLE 7 Vs↑2 VS Pe↑1/3
+=BRINE SAT., SQU.=AIR SAT.

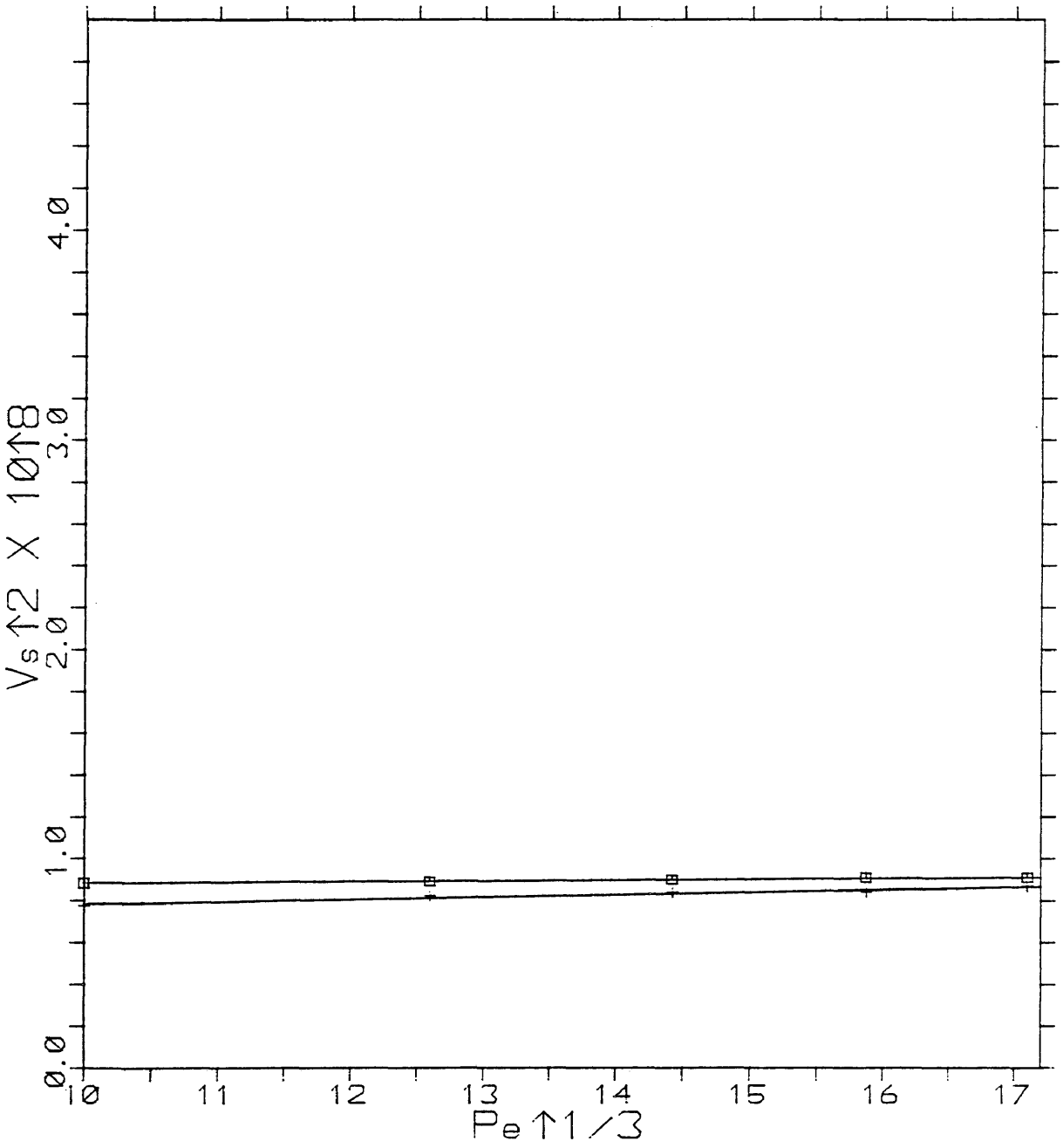

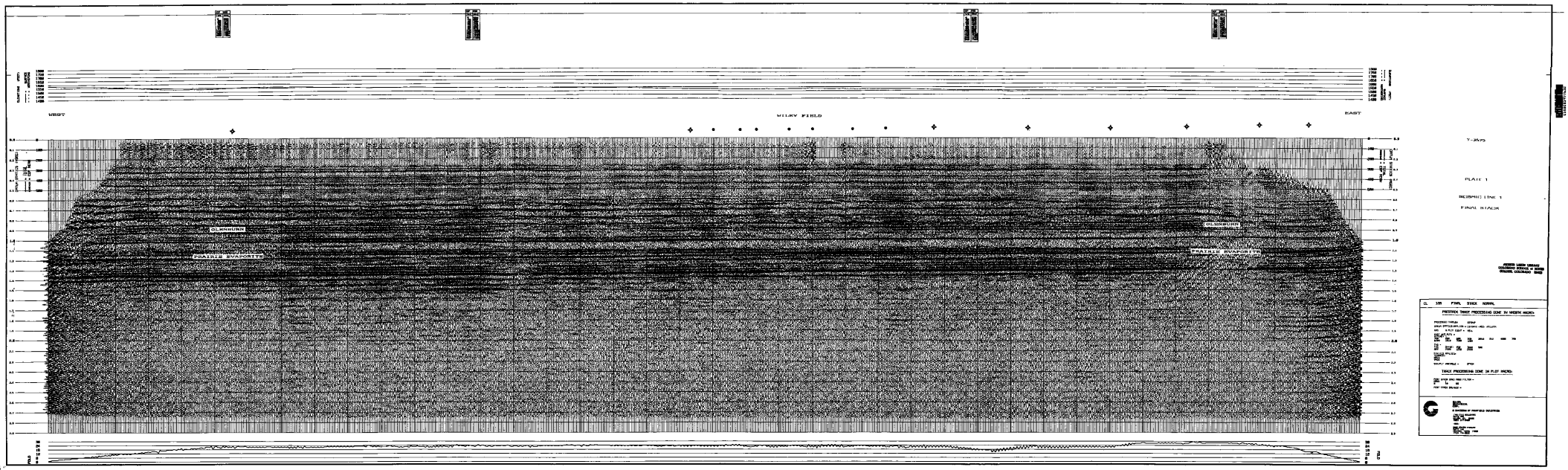

Y-3679

PLATE 1

SEISMIC LINE 1

FINAL RIALM

CL 105 FINAL STACK NORMAL

PRESTACK TRACE PROCESSING DONE IN MIDPOINT ORDER:

TRACE PROCESSING DONE IN PLOT ORDER:

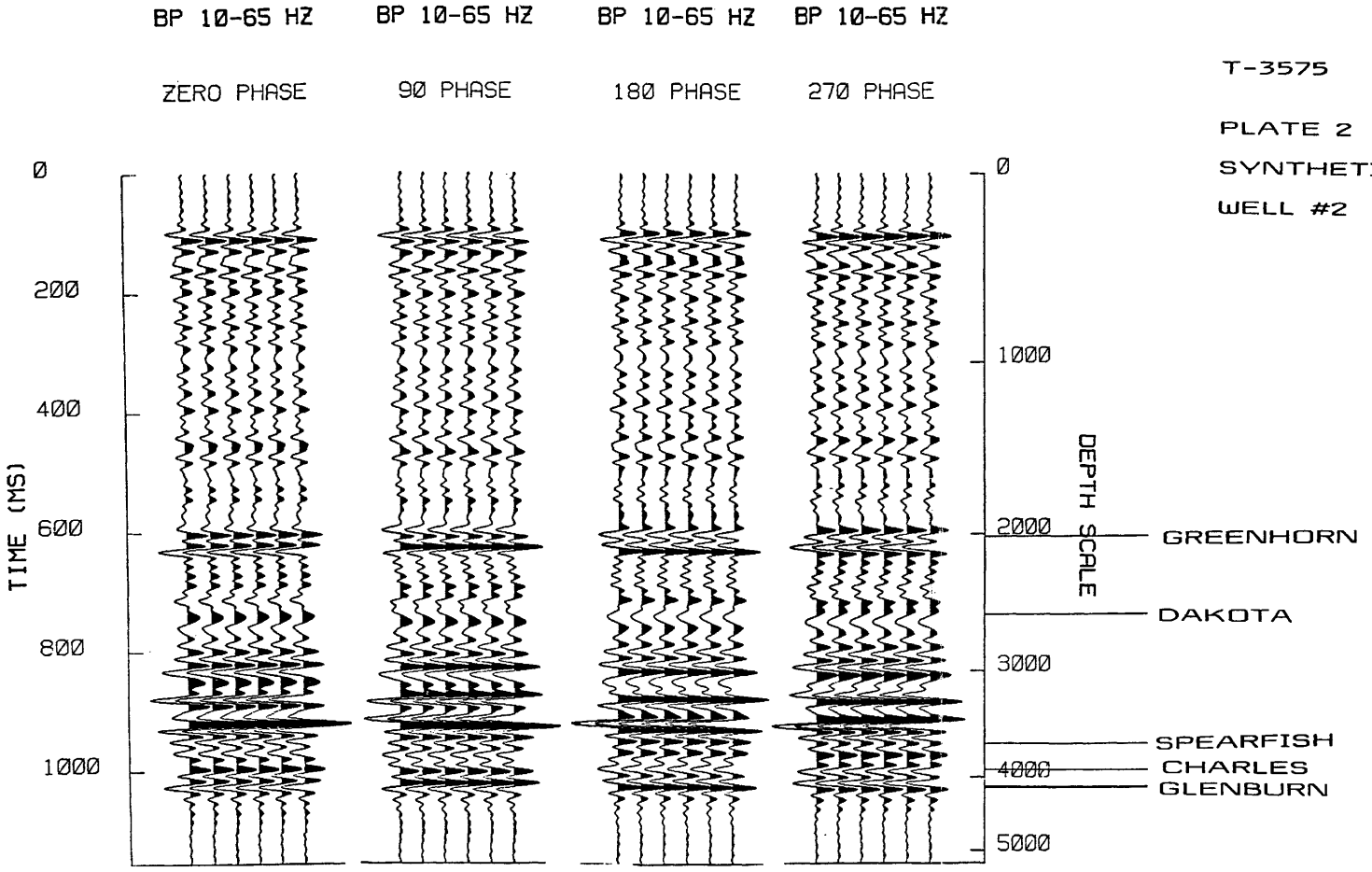

T-3575

PLATE 2

SYNTHETIC SEISMOGRAM

WELL #2